GULF GENERAL ATOMIC

Gulf-GA-A12818
UC-77

HTGR BASE PROGRAM
QUARTERLY PROGRESS REPORT
FOR THE PERIOD ENDING
NOVEMBER 30, 1973

Prepared under
Contract AT(04-3)-167
Project Agreement No. 17
for the
San Francisco Operations Office
U.S. Atomic Energy Commission

Date Published - December 28, 1973

GULF GENERAL ATOMIC COMPANY
P.O. BOX 81608, SAN DIEGO, CALIFORNIA 92138

Printed in the United States of America
Available from
National Technical Information Service
U.S. Department of Commerce
5285 Port Royal Road
Springfield, Virginia 22151
Price: Printed Copy $5.45; Microfiche $1.45

DISCLAIMER

GULF GENERAL ATOMIC

Gulf-GA-A12818
UC-77

HTGR BASE PROGRAM
QUARTERLY PROGRESS REPORT
FOR THE PERIOD ENDING
NOVEMBER 30, 1973

Prepared under
Contract AT(04-3)-167
Project Agreement No. 17
for the
San Francisco Operations Office
U.S. Atomic Energy Commission

Gulf General Atomic Project 317

Date Published - December 28, 1973

GULF GENERAL ATOMIC COMPANY
P.O. BOX 81608, SAN DIEGO, CALIFORNIA 92138

QUARTERLY REPORT SERIES

GA-4072-December, 1962, through February, 1963
GA-4350-March, 1963, through May, 1963
GA-4569-June, 1963, through August, 1963
GA-4937-September, 1963, through November, 1963
GA-5104-December, 1963, through February, 1964
GA-5366-March, 1964, through May, 1964
GA-5618-June, 1964, through August, 1964
GA-5866-September, 1964, through November, 1964
GA-6113-December, 1964, through February, 1965
GA-6418-March, 1965, through May, 1965
GA-6671-June, 1965, through August, 1965
GA-6869-September, 1965, through November, 1965
GA-7010-December, 1965, through February, 1966
GA-7181-March, 1966, through May, 1966
GA-7396-June, 1966, through August, 1966
GA-7553-September, 1966, through November, 1966
GA-7801-December, 1966, through February, 1967
GA-7981-March, 1967, through May, 1967
GA-8200-June, 1967, through August, 1967
GA-8356-September, 1967, through November, 1967
GA-8530-December, 1967, through February, 1968
GA-8662-March, 1968, through May, 1968
GA-8860-June, 1968, through August, 1968
GA-9090-September, 1968, through November, 1968
GA-9227-December, 1968, through February, 1969
GA-9372-March, 1969, through May, 1969
GA-9660-June, 1969, through August, 1969
GA-9815-September, 1969, through November, 1969
GA-9944-December, 1969, through February, 1970
GA-10088-March, 1970, through May, 1970
GA-10288-June, 1970, through August, 1970
GA-10399-September, 1970, through November, 1970
GA-10501-December, 1970, through February, 1971
GA-10661-March, 1971, through May, 1971
Gulf-GA-A10784-June, 1971, through August, 1971
Gulf-GA-A10930-September, 1971, through November, 1971
Gulf-GA-A10999-December, 1971, through February, 1972
Gulf-GA-A12150-March, 1972, through May, 1972
Gulf-GA-A12222-June, 1972, through August, 1972
Gulf-GA-A12422-September, 1972, through November, 1972
Gulf-GA-A12515-December, 1972, through February, 1973
Gulf-GA-A12575-December, 1972, through February, 1973
Gulf-GA-A12599-March, 1973, through May, 1973
Gulf-GA-A12725-June, 1973, through August, 1973

ABSTRACT

This publication continues the quarterly report series on the HTGR Base Program. The Program covers items of the base technology of the High-Temperature Gas-cooled Reactor (HTGR) system. The development of the HTGR system will, in part, meet the greater national objective of more effective and efficient utilization of our national resources. The work reported here includes studies of basic fission-product distribution mechanisms, recycle fuel studies (including designing and testing of recycle test elements) and exploration of head-end reprocessing methods (as part of a national recycle plan and of a recycle fuel plan), and physics and fuel management studies. Materials studies include irradiation and analysis of fuel particles in capsules to evaluate fuel systems, and basic studies of control materials and of carbon and graphite. Experimental procedures and results are discussed and, where appropriate, the data are presented in tables, graphs, and photographs. More detailed descriptions of experimental work are presented in topical reports, and these are listed at the end of the report for those concerned with the field.

INTRODUCTION

This report covers the work performed by Gulf General Atomic under U.S. Atomic Energy Commission Contract AT(04-3)-167, Project Agreement No. 17. This Project Agreement calls for support of basic technology associated with gas-cooled, nuclear power reactor systems. The program is based on the concept of the High-temperature Gas-cooled Reactor (HTGR) developed by Gulf General Atomic.

Large HTGR systems will be placed in operation starting in the late 1970's following the operation of the 330-MW(e) prototype in 1973. Characteristics of these advanced systems include:

1. A single-phase gas coolant allowing generation of high-temperature, high-pressure steam with consequent high-efficiency energy conversion and low thermal discharge.

2. A prestressed concrete reactor vessel (PCRV) offering advantages in field construction, primary system integrity, and stressed member inspectability.

3. Graphite core material assuring high-temperature structural strength, large temperature safety margins, and good neutron economy.

4. Thorium fuel cycle leading to U-233 fuel which allows good utilization of nuclear resources and minimum demands on separative work.

CONTENTS

ABSTRACT iii

INTRODUCTION v

TASK IV. FISSION PRODUCT MECHANISMS 1

Vapor Pressure Studies 1
FIPER Code Work 1
FIPER Code Development 1
FIPER Code Applications 16
Fission Product Plateout and Liftoff Studies 22
Reaction of Steam with Graphite 23
Reference 24

TASK V. RECYCLE FUEL STUDIES 26

HTGR Fuel Recycle Plant Study 26
System Design Description for Cold Pilot Plant 26
Design Criteria for Commercial Reprocessing Plant 26
Conceptual Flowsheets and Material Balances for Refabrication 26
Liaison with National Laboratories and AEC 26
Head-End Reprocessing 28
Summary 28
Crushing 29
Solids Handling 33
Primary Fluidized-Bed Burner 34
Secondary Fluidized-Bed Burner 38
Leaching 54

TASK VIII. PHYSICS AND FUEL MANAGEMENT 67

ENDF/B Participation 67
Analysis of HTGR and HTLTR Critical Experiments 68
Re-analysis of Control Rod Experiments Performed at the HTGR Critical Facility 68
Analysis of HTLTR Critical Experiments 79
HTLTR Reactivation 79
Topical Report Summarizing GGA Analysis of the HTGR and HTLTR Critical Experiments 80
Analysis of Reactor Noise and Pulsed-Neutron Experiments in Large HTGRs 80
Test Element Program 81
Fuel Test Element FTE-3 81
References 93

TASK IX. FUEL MATERIALS DEVELOPMENT 94

Fuel Irradiations 94
Capsule P13N 94
Capsule P13P 95
Capsules P13R and P13S 97
Capsule P13T 100
GGA-ORNL Cooperative Irradiation Capsules 100

TASK XI. GRAPHITE RESEARCH 119

Introduction 119
Capsule Irradiations 119
Capsule OG-1 119
Capsule OG-2 120
HT-20 through -23 120
Graphite Properties and Irradiation 120
Project Plan 121

FIGURES

4-1. Comparison of FIPER S assumptions and actual solution 3

4-2. Fission product release from failed TRISO particles 13

4-3. Calculated release of long-lived nuclide from a BISO coated fuel particle assuming coating control and steady power 18

4-4. Calculated release of long-lived nuclide from a BISO coated particle assuming coating control and an initial power interval followed by release 19

4-5. Calculated release of long-lived metallic nuclide from a BISO coated particle assuming kernel control and an initial power interval followed by release 21

4-6. Effect of helium pressure on the rate of reaction with steam with H-327 graphite 25

5-1. Physical arrangement of tertiary crusher 30

5-2. Details of tertiary crusher 31

5-3. Recycle auger system 35

5-4. Extended feed auger system 36

5-5. 10-cm primary burner auger performance 37

5-6. 10-cm secondary burner layout 39

5-7. Cross section of resistance-heated secondary burner 40

5-8. Cross section of induction-heated secondary burner 41

5-9. Typical induction heating system 44

5-10. Size distribution for particle crushing system 48

5-11. Lower section of 10-cm secondary burner showing high-temperature bed removal system and burner alignment mechanisms 51

5-12. High-temperature bed removal system for 10-cm secondary fluid bed burner 52

5-13. Size distribution of feed and product, run F4RHB-M24 53

5-14. ORNL sol gel dissolution, runs 58, 59, 62, and 67 through 71 55

5-15. Feed size distribution, runs 58, 59, 62, 67, 68, and 69 through 71 58

8-1. Design of fission product release spine samples in FTE-3 84

8-2. Design of diffusion spine samples 90

9-1. Kernel migration coefficient versus 1/T for UO_2 TRISO particles from fuel rods 2D-16, 2A-10, 4D-9, and 5A-19 irradiated in capsule P13N 96

9-2. Schematic layout showing temperature-fluence conditions for capsules P13R and P13S 99

TABLES

5-1. Parts list for "Centerol" crusher 32

5-2. Summary of BISO-ThO_2 burn-back tests 49

5-3. Leacher operating data, 13-cm-diameter leacher 57

5-4. Weight factor and specific gravity calibrations for vessels . 59

5-5. Sample analysis results, 13-cm-diameter leacher 61

5-6. Thorium material balance results, 13-cm-diameter leacher 62

5-7. Estimated value of c 63

5-8. Comparison between storage tanks using calibration relations from Table 5-4, 13-cm-diameter leacher, Thorex tank 64

5-9. Comparison between storage tanks using calibration relations from Table 5-4, 13-cm-diameter leacher, mother liquor tank .. 65

8-1. Radial dimensions of core and reflector with large control rods 70

8-2. Measured core reactivity 70

8-3. Energy group structures 72

8-4. Effect of annealing on fission gas release for fuel rods irradiated in FTE-3 82

8-5. Description of fuel particles used in niobium-canned fission product release samples irradiated in FTE-3 85

8-6. Thermal analysis of niobium-canned fission product release samples irradiated in FTE-3 86

8-7. Distribution of Cs-137, Ce-144, and Zr-95 in fission product release samples irradiated in FTE-3 87

8-8. Cesium sorption ratios derived from data for FTE-3 diffusion samples 92

9-1. Description of fuel rods being tested in capsule P13R 101

9-2. Description of fuel rods being tested in capsule P13S 103

9-3. Fuel rod variables being tested in capsules P13R and P13S ... 105

9-4. TRISO coated fissile particle variables being tested in irradiation experiments P13R and P13S 106

9-5. Fertile particle variables being tested in irradiation experiments P13R and P13S 107

9-6. Description of coated particles being tested in capsule P13R 109

9-7. Description of coated particles being tested in capsule P13S 111

9-8. Description of coated particle samples being tested in capsule P13Q 113

9-9. Description of fuel rods being tested in capsule P13Q 115

TASK IV
FISSION PRODUCT MECHANISMS

VAPOR PRESSURE STUDIES

Work is under way to obtain sorption (equilibrium vapor pressure) data for cesium on fuel rod matrix material. This work is being done using the mass spectrometric technique in which a Knudsen cell is mounted in a mass spectrometer.

The study will provide information for use in assigning values to $\emptyset$, the sorption ratio (or partition coefficient), which is an important input parameter for FIPER calculations. The sorption ratio is defined as the ratio of the fission product metal concentration between the fuel block graphite and the fuel rod matrix, measured at the graphite-matrix interface (gap).

$$\emptyset = \frac{\text{concentration of metal in fuel matrix}}{\text{concentration of metal in graphite}}$$

One source of values of $\emptyset$ is data on the sorption behavior of metals on graphite and fuel rod matrix materials.

FIPER CODE WORK

FIPER Code Development

The FIPER code is used for calculating the release of metallic fission products into the primary coolant circuit of HTGR systems. Two forms of the FIPER code, FIPER Q and FIPER S, are utilized. FIPER Q, the basic rigorous version, uses an accurate but rather costly finite difference

solution. FIPER S uses a very rapid and approximate closed form solution. FIPER S is a design tool, intended for use in core survey and parametric study applications where FIPER Q would be too costly.

The original version of FIPER S contained a number of approximations that, in certain circumstances, could lead to a substantial overestimate of fission product release. The most important of these were:

1. An insulated (zero mass flux) boundary condition was at the coolant hole.

2. Conservation of mass was neglected. The inventory of fission products was not reduced by release, and it was possible to release more than was actually produced.

The possibility of improving the approximations used in the original FIPER S led to a reevaluation of the assumptions and the model. It was determined that a reasonably rapid exact analytical solution was possible with an improved model that uses very few restrictive assumptions.

A new model was developed based on (1) a new differential equation that includes thermal diffusion and radioactive decay, and (2) an exact solution of the equation using a realistic convection boundary condition at the coolant hole. A computer program to solve the differential equation was written and checked out. Details of the work are described in the previous Quarterly Progress Report (Gulf-GA-A12725).

It was decided to develop an interim version of FIPER S for immediate use in design calculations and to serve as a basis for checking out the advanced version. The ground rules for the interim model were (1) that it be capable of reading the latest power tapes, (2) that it be capable of a more refined local analysis (as opposed to block average calculations), and (3) that it incorporate an empirical means of correcting for some of the more significant discrepancies between FIPER Q and FIPER S.

Work on the interim FIPER S code, which was carried out in the previous quarter, is now complete. The interim code will serve three useful purposes. First, it will permit us to do calculations while a new code is being developed. Second, the driver program will serve as an ideal test-bed for the new model. Third, the release values calculated by the interim code can be used to check out various aspects of the new model. A summary of the improvements and changes leading to the interim code is given below.

Boundary Condition Correction

The original FIPER S model assumed that the coolant hole boundary was insulated, whereas in actuality a concentration gradient is required to support the mass flux (Fig. 4-1).

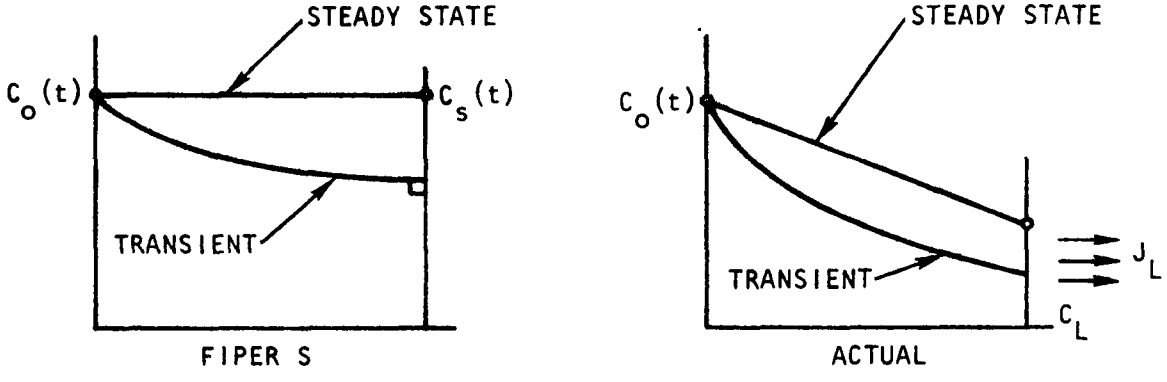

Fig. 4-1. Comparison of FIPER S assumptions and actual solution

An approximate, empirical correction was made in order to make FIPER S correspond more closely to the actual solution.

The correction was accomplished by first reducing the problem to simpler terms, namely, an equivalent steady-state isothermal problem with a known input concentration history, $C_o(t)$. Having defined the equivalent isothermal problem (by a method to be described on the following pages), an

exact calculation of release by a closed-form analytical expression is possible. This new release is the corrected release. The FIPER S portion of the calculation, which by itself is erroneous, serves mainly as an integrator to determine the effect of varying conditions of temperature, temperature gradients, coolant flow, etc., in defining the equivalent isothermal problem. While not strictly accurate, this procedure probably reduces errors to within a factor of two.

The first step in the correction is to approximate the input concentration history, $C_o(t)$. Since the FIPER S diffusion calculations operate primarily in the steady-state regime (see Fig. 4-1), it is reasonable to assume that

$$C_o(t) = C_s(t) \quad . \tag{4-1}$$

Next, this function is evaluated at two time points, a mid-time and the end-time. Having done this, a simplified power function is fitted to the concentration history. The resulting approximation is

$$C_o(t) \approx C_{end}\left(\frac{t}{t_{end}}\right)^Z \quad , \tag{4-2}$$

where

$$Z = \frac{\log\left(\frac{C_{mid}}{C_{end}}\right)}{\log\left(\frac{t_{mid}}{t_{end}}\right)} \quad . \tag{4-3}$$

Knowing the concentration history, the vapor pressure versus concentration relationships are then used to determine the mass flux. In the Freundlich regime,

$$P = e^{m(T)}\left(\frac{C_L}{\rho}\right)^{n(T)} \qquad \left[C_L > C_{tran}\right] \quad , \tag{4-4}$$

and in the Henrian regime

$$P = e^{m(t)} \frac{C_{tran}^{n(T)-1} C_L}{\rho^n} \quad \left[C_L \leq C_{tran}\right] \quad . \tag{4-5}$$

Having determined the vapor pressure, the mass flux is given by

$$J_L(t) = \frac{K(t)\ (1.013\ \text{exp}\ 12)\ P(t)}{RT} \quad . \tag{4-6}$$

Combining the above equations, it can be shown that

$$J_L(t) = \varepsilon_F(T)\ C_L(t)^{n(T)} \qquad \left[C_L > C_{tran}\right] \tag{4-7}$$

and

$$J_L(t) = \varepsilon_H(T)\ C_L(t) \qquad \left[C_L \leq C_{tran}\right] \quad , \tag{4-8}$$

where ε_F and ε_H are functions of temperature defined through Eqs. 4-4, 4-5, and 4-6. Assuming that the temperature is constant, Eqs. 4-7 and 4-8 can be integrated in closed form to obtain the average mass flux. Substituting the concentration history (Eq. 4-2) into Eqs. 4-7 and 4-8 and integrating, the average mass flux for the isothermal problem can be shown to be

$$\overline{J}_S = \frac{\varepsilon_H(T)\ C_{end}\ f_H^{Z+1}}{Z+1} + \frac{\varepsilon_F(T)\ C_{end}^{n(T)} \left(1 - f_H^{Zn+1}\right)}{Zn+1} \quad , \tag{4-9}$$

where

$$f_H = \frac{t_{tran}}{t_{end}} \tag{4-10}$$

is the fraction of time spent in the Henrian regime.

The basis for defining the equivalent isothermal model has now been obtained. First, the mean mass flux $\bar{J}_S$ is calculated from the FIPER S release. Having this numerical value, Eq. 4-9 is then solved iteratively for the temperature T. Thus, the temperature of an equivalent isothermal problem that would give the same (incorrect) release as FIPER S did for the varying temperature case is defined.

The next step is to correct the isothermal model for the boundary condition error. This is done by solving a mass balance equation. In the Freundlich regime this equation is

$$\frac{D\left[C_o(t) - C_L(t)\right]}{L} = \varepsilon_F \, C_L(t)^n \quad , \tag{4-11}$$

where D is the diffusion coefficient and L is the length of the graphite diffusion region. The left-hand side of Eq. 4-11 is simply the steady-state mass flux that diffuses through the graphite, with the indicated concentration gradient as a driving force. The right-hand side is the mass flux due to vaporization on the coolant boundary (see Eq. 4-7). Continuity requires that these fluxes be equal.

Equation 4-11 can be solved iteratively for the corrected concentration C_L. This is done at two points in time, after substituting the explicit time dependency of C_o from Eq. 4-2. These two solutions for C_L then form the basis for a function fit similar to that of Eq. 4-2. Thus, the following equation is derived:

$$C_L(t)_F = C_L(t_{end})_F \left(\frac{t}{t_{end}}\right)^X \quad , \tag{4-12}$$

where

$$X = \frac{\log\left[\frac{C_L(t_{mid})}{C_L(t_{end})}\right]}{\log\left(\frac{t_{mid}}{t_{end}}\right)} \quad , \tag{4-13}$$

and where the subscript F designates the Freundlich regime. Equation 4-12 is the corrected concentration history that would result if the Freundlich behavior existed throughout life.

In a similar manner, employing Eq. 4-8, the continuity condition in the Henrian regime is

$$\frac{D\left[C_o(t) - C_L(t)\right]}{L} = \varepsilon_H C_L(t) \quad . \tag{4-14}$$

This equation can be solved exactly for C_L, with the result that

$$C_L(t)_H = \frac{C_{end}}{\left(\frac{L\,\varepsilon_H}{D} + 1\right)} \left(\frac{t}{t_{end}}\right)^Z$$

$$= C_L(t_{end})_H \left(\frac{t}{t_{end}}\right)^Z \quad . \tag{4-15}$$

Having thus obtained two corrected concentration histories, these can be integrated, as in the previous uncorrected case, to obtain a corrected average mass flux. This results in

$$\bar{J}_C = \frac{\varepsilon_H C_L(t_{end})_H f_H^{Z+1}}{Z+1}$$

$$+ \frac{\varepsilon_F C_L(t_{end})_F (1 - f_H^{Xn+1})}{Xn+1} \quad . \tag{4-16}$$

The similarity between Eqs. 4-16 and 4-9 is immediately obvious. The two differences are that the end concentrations (C_L) are corrected and that the time dependency in the Freundlich regime is changed. The corrected release in curies is then

$$R_C = R_S \left(\frac{\bar{J}_C}{\bar{J}_S}\right) \quad . \tag{4-17}$$

Conservation of Mass Correction

Even after the above boundary condition correction is applied, it is still possible for the FIPER S release to be more than is produced. The reason for this is that the released mass is never subtracted from the inventory of mass available for release. This can be corrected by the procedure described below.

It is assumed that the block release is proportional to a driving force, representing the amount of fission product (released from particles) that is still available for release from the block. In the FIPER S model, where release is not substracted,

$$R_C = k\, T_p \quad , \tag{4-18}$$

where T_p is the total released from particles. In actuality, the driving force is less due to the fact that some of T_p is released. Thus,

$$R_C^* = k(T_p - R_C^*) \quad , \tag{4-19}$$

where R_C^* is the release corrected for the mass balance. Solving Eq. 4-18 for k and substituting into Eq. 4-19 gives

$$R_C^* = \frac{R_C}{T_p}(T_p - R_C^*) \quad . \tag{4-20}$$

Solving this for R_C^* gives

$$R_C^* = R_C \left(\frac{1}{1 + \frac{R_C}{T_p}} \right) \quad . \tag{4-21}$$

It is seen that, after applying the above correction, it is never possible for R_C^* to exceed T_p.

Concentration Ratio ($\emptyset$) Calculation

In the original FIPER S code the concentration ratio at the fuel rod-graphite interface was input as a constant, $\emptyset$. In actuality, this ratio depends on the vapor pressure versus sorptivity relationships in the gap. These, in turn, depend on the temperature and the temperature gradient in the gap. Since these latter quantities are functions of both spatial position and time in the reactor, and since the sorptivity equations are well known, it was clear that this concentration ratio should be calculated in the code as a function of spatial point and time. The equations used to do this are described below.

First, the fuel rod surface concentration C_F, which is calculated directly from the particle release model, is assumed to be given as a function of time. This surface concentration is in equilibrium with a vapor pressure P in the gap. The equations describing this equilibrium are

$$P = e^{m_1(T_1)} \quad (C_F)^{n_1(T_1)} \qquad \left[C_F > C_{tran_1}\right] \tag{4-22}$$

or

$$P = e^{m_1(T)} \; C_{tran_1}{}^{n_1(T_1)-1} \; C_F \left[C_F \leq C_{tran_1}\right] \quad , \tag{4-23}$$

where the subscript 1 refers to the inside of the gap. The above equations are the Freundlich and the Henrian absorption isotherms, respectively, for the fuel rod matrix material. Note that the above equations differ from the earlier equations (4-4 and 4-5) by a density factor ρ. This is because the present calculation is most conveniently carried out in concentration units of μ moles/gram. The density factor is not presently required, but will be introduced later.

Having obtained the vapor pressure in the gap, it is noted that this pressure must be constant throughout the gap. In particular, it is the

same on the graphite moderator surface. Equations similar to Eqs. 4-22 and 4-23 also apply to the graphite surface, except that now the temperature is T_2 and the adsorption functions are n_2 and m_2. Solving these equations for the graphite concentration, C_G,

$$C_G = \left[\frac{P}{e^{m_2(T_2)}}\right]^{1/n_2(T_2)} \qquad \left[C_G > C_{tran_2}\right] \tag{4-24}$$

or

$$C_G = \left[\frac{P}{e^{m_2(T_2)}}\right]\left(\frac{1}{C_{tran}}\right)^{n_2(T_2)-1} \qquad \left[C_G \leq C_{tran_2}\right] . \tag{4-25}$$

Since C_G is not known prior to the evaluation above, it is necessary to first solve for the transition vapor pressure:

$$P_{tran} = e^{m_2(T_2)}\, C_{tran}^{n_2(T_2)} . \tag{4-26}$$

Having the transition pressure, the implication

$$(P < P_{tran}) \Longrightarrow (C < C_{tran}) \tag{4-27}$$

is used to choose between Eqs. 4-24 and 4-25.

The concentrations C_F and C_G, as previously mentioned, have been computed in units of μ moles/gram. The ratio of concentrations expressed in μ moles/cm^3 is therefore

$$\phi = \frac{C_F\, \rho_F}{C_G\, \rho_G} . \tag{4-28}$$

Particle Release Model

In the original FIPER S code, there were two optional particle release models. One was a straight line "failure" function, wherein fractional release was a linear function of time, uniform throughout the reactor. The second model was based on particle failures by an empirical kernel migration equation. An improved particle release model was devised with the following modes of release:

1. 100% release from failed TRISO particles.
2. 100% release from failed BISO particles.
3. Diffusion release from intact BISO particles.

In order to calculate release separately for the two particle types, it was necessary to separately account for the birth rate and to determine the relative volumetric contribution of the two particle types. The means for doing this are fairly complicated, and too lengthy to describe in full detail in this report. A summary of the method, however, is given below.

Given the incremental number of fissions as a function of power level and time increment,

$$\Delta f = P\ \Delta t\ \frac{(3.3 \times 10^{10})\ (16^{6})}{(6.023 \times 10^{23})} \quad . \tag{4-29}$$

This total number of fissions can be partitioned among the two particle types (TRISO and BISO) according to

$$\Delta f_T = \Delta f * \text{FACTOR} \tag{4-30}$$

and

$$\Delta f_B = \Delta f * (1 - \text{FACTOR}) \quad , \tag{4-31}$$

where

$$\text{FACTOR} = \frac{\Delta \text{FIMA}_T}{\Delta \text{FIMA}_T + \Delta \text{FIMA}_B \cdot R_{T/U}} \quad . \tag{4-32}$$

In the above equations the subscripts T and B stand for TRISO and BISO, respectively. The ΔFIMAs are the incremental number of fissions per initial metal atom for the two particle types. The $R_{T/U}$ is the thorium-uranium ratio, a factor required to convert the "initial metal atoms" to a common denominator, thus accounting for the relative volumetric contribution of the two particle types. The FACTOR calculated by Eq. 4-32 is a function of spatial position and time.

Having thus determined the fission density distribution between the particles, the incremental birth of fission products is given by

$$\Delta B_T = \Delta f_T \cdot \text{YIELD}_T \tag{4-33}$$

$$\Delta B_B = \Delta f_B \cdot \text{YIELD}_B \quad . \tag{4-34}$$

The total production in any particle type is then

$$B_T = \Sigma \Delta B_T \tag{4-35}$$

$$B_B = \Sigma \Delta B_B \tag{4-36}$$

and the total production for all particles is

$$B_{TOT} = B_T + B_B \quad . \tag{4-37}$$

The TRISO particles are assumed to fail, releasing 100% of their fission product inventories, according to an arbitrary function of fast neutron dose (Fig. 4-2).

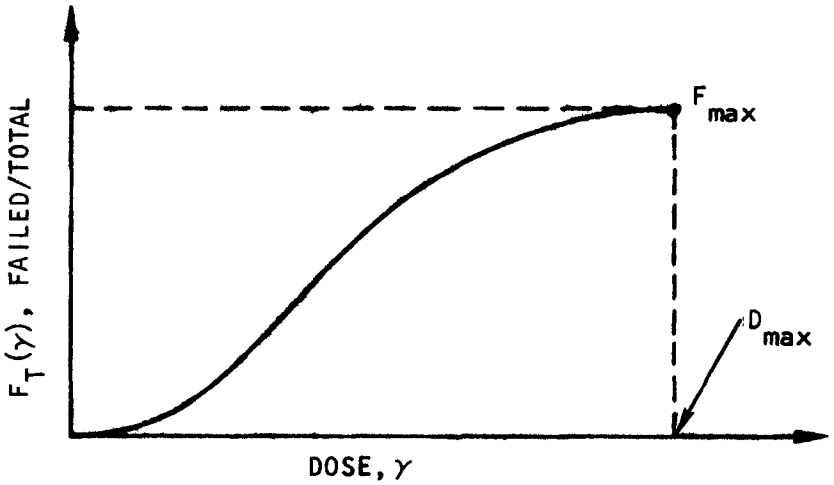

Fig. 4-2. Fission product release from failed TRISO particles

The release from failed TRISO particles is then

$$R_T = F_T(\gamma)\ B_T \quad . \tag{4-38}$$

Failure of BISO particles is calculated by a procedure that is identical to the above method, except that a different failure function is input. The release from failed BISO particles is

$$R_{B_F} = F_B(\gamma)\ B_B \quad . \tag{4-39}$$

Release by diffusion is calculated by a numerical application of Duhamel's superposition principle. The differential equation of diffusion in one-dimensional slab geometry is

$$\frac{\partial C}{\partial t} = D\frac{\partial^2 C}{\partial x^2} \quad \left[C = C(x,t)\right] \quad . \tag{4-40}$$

By a transformation of independent variables,

$$\rho(t) = \int_0^t \frac{D}{L^2}\, d\tau \qquad (4\text{-}41)$$

and

$$\xi = \frac{x - x_o}{L} \quad . \qquad (4\text{-}42)$$

Equation 4-40 can be written in nondimensional form

$$\frac{\partial C}{\partial \rho} = \frac{\partial^2 C}{\partial \xi^2} \quad . \qquad (4\text{-}43)$$

Equation 4-43 implies that, for a given set of boundary conditions and initial conditions, the solution C is a function of only ρ and ξ. Furthermore, the solution at a given spatial point is a function of ρ alone. This theory was investigated by using FIPER Q to analyze an actual BISO particle. Although it is not precisely a slab geometry, the coating is thin enough for slab geometry to be a reasonable approximation. It was found, indeed, that for a given set of boundary conditions

$$\frac{R}{B}(t) = \mathcal{T}(\rho) \quad . \qquad (4\text{-}44)$$

FIPER Q was then used to generate the release function $\mathcal{T}$ for the case of a single impulse of fission products born inside the particle (see Figs. 4-4 and 4-5 and accompanying text in section on FIPER Code Applications).

The release

$$R(t) = \Delta B\, \mathcal{T}[\rho(t)] \qquad (4\text{-}45)$$

was determined numerically from the FIPER Q output. For a succession of birth pulses, ΔB_i, the principle of superposition gives the total release

$$R(t) = \sum_{i=1}^{n} \mathcal{F}[\rho(t) - \rho(t_i)]\ \Delta B_i \quad . \tag{4-46}$$

Alternately, Eq. 4-46 can be expressed in integral form as

$$R(t) = \int_{0}^{\rho(t)} \mathcal{F}(\rho - \rho')\ \frac{dB}{d\rho'}\ d\rho' \quad . \tag{4-47}$$

This integral is evaluated in FIPER S using the trapezoidal rule. At each time point the entire past history must be examined and the release contribution of all the birth pulses up to the present time must be summed. The total fractional release by diffusion from intact BISO particles is then

$$F_D(t) = \frac{R(t)}{B_B(t)} \quad . \tag{4-48}$$

It is noted that this fraction is independent of the actual number of intact BISO particles. It can be calculated on the assumption that all the particles remain intact, and then the actual failure fraction can be considered later. Thus, the total fraction of intact BISO particles at any time is

$$F_{INTACT} = 1 - F_B(\gamma) \tag{4-49}$$

and the total release from BISO particles, including failure and diffusion from intact particles, is

$$R_{B_{TOTAL}} = B_B \left\{F_B(\gamma) + [1 - F_B(\gamma)]\ F_D(t)\right\} \quad . \tag{4-50}$$

Combining Eqs. 4-50 and 4-38, the total release from all particles is

$$R_{TOT} = F_T B_T + B_B \left[F_B + (1 - F_B)F_D\right] \quad . \tag{4-51}$$

The total effective release fraction is then

$$F_{TOT} = \frac{R_{TOT}}{B_{TOT}} \quad . \tag{4-52}$$

This completes the particle release calculation.

FIPER Code Applications

The spherical coordinate option of the FIPER Q code was used to calculate the release of long-lived fission product metal nuclides (such as Cs-137 and Sr-90) from intact BISO coated fuel particles. The purpose of this work was to serve as a basis for calculating diffusive release from BISO fuel particles in HTGR core calculations and to obtain calculated release versus time curves for comparison with observed curves.

The assumptions used in the calculations are:

1. Release is controlled either by diffusion in the fuel kernel or in the pyrolytic carbon coating.

2. Diffusion obeys Fick's law.

3. A unity partition coefficient (sorption ratio) is assumed between the different material regions of the coated particle.

4. A zero metallic fission product concentration is assumed at the other pyrolytic carbon surface.

5. Release is assumed to be independent of fast fluence or burnup.

Results of the calculations are in the form of curves showing accumulated fractional release as a function of the dimensionless quantity Dt/ℓ^2, where D is the diffusion coefficient (cm^2/sec) of the metallic nuclide in the pyrolytic carbon coating (or in the fuel kernel), t is the release time (sec), and ℓ is the thickness (cm) of the outer (dense) pyrolytic carbon coating (or ℓ is the radius of the kernel). Calculations were made for three different cases.

In the first case, it was assumed that release is controlled by diffusion in the pyrolytic carbon coating, and that steady-state production of the metallic nuclide (steady power) occurs. In this calculation, the diffusion coefficient for the fuel kernel was taken to be orders of magnitude larger than the diffusion coefficient for the pyrolytic carbon. The result of the calculation is the curve shown in Fig. 4-3. In this case, the dimensionless quantity is $D_c t/\ell_c^2$, where D_c is the diffusion coefficient for the metallic nuclide in the outer (dense) pyrolytic carbon coating, t is the release (or irradiation) time, and ℓ is the coating thickness. The curve in Fig. 4-3 can be used to obtain a value for the in-pile release of a long-lived metallic nuclide (e.g., Cs-137) from a BISO coated particle. Knowing values of D_c, t, and ℓ_c, a value for $D_c t/\ell_c^2$ is calculated; from this value and the curve in Fig. 4-3, a value for the accumulated fractional release can be derived.

In the second case, it was assumed that release is controlled by diffusion in the pyrolytic carbon coating in which the metallic nuclide is produced with no release in an initial time (power) period, and release with no production (no power) occurs in a following time period. The calculated curve is shown in Fig. 4-4. This case applies, for example, to laboratory (out-of-pile) release of Cs-137 in anneal tests using BISO coated particles irradiated under conditions where no cesium release occurs. In this case, t is the release time, and D_c and ℓ_c are the same as for the first case.

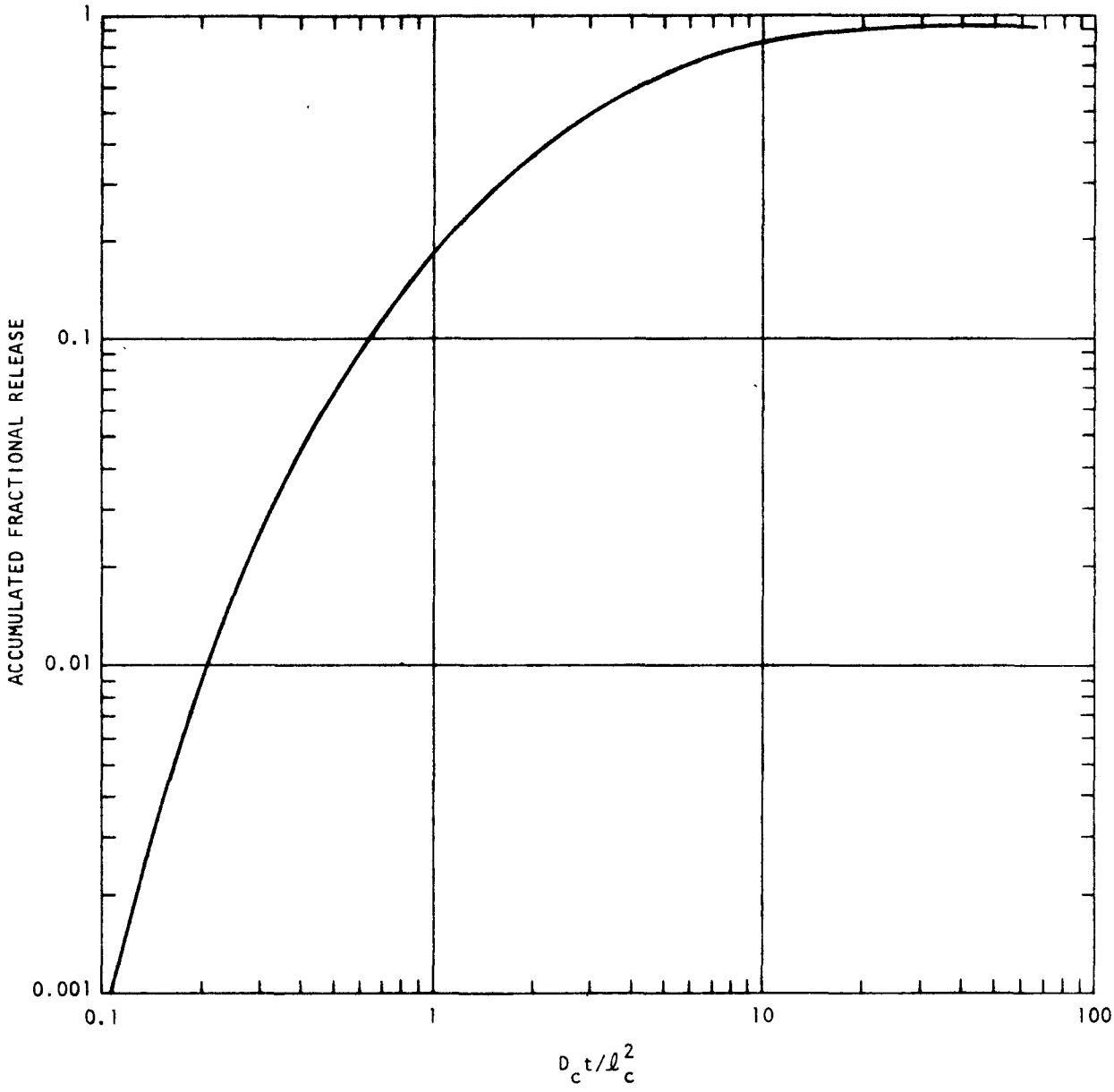

Fig. 4-3. Calculated release of long-lived nuclide from a BISO coated fuel particle assuming coating control and steady power

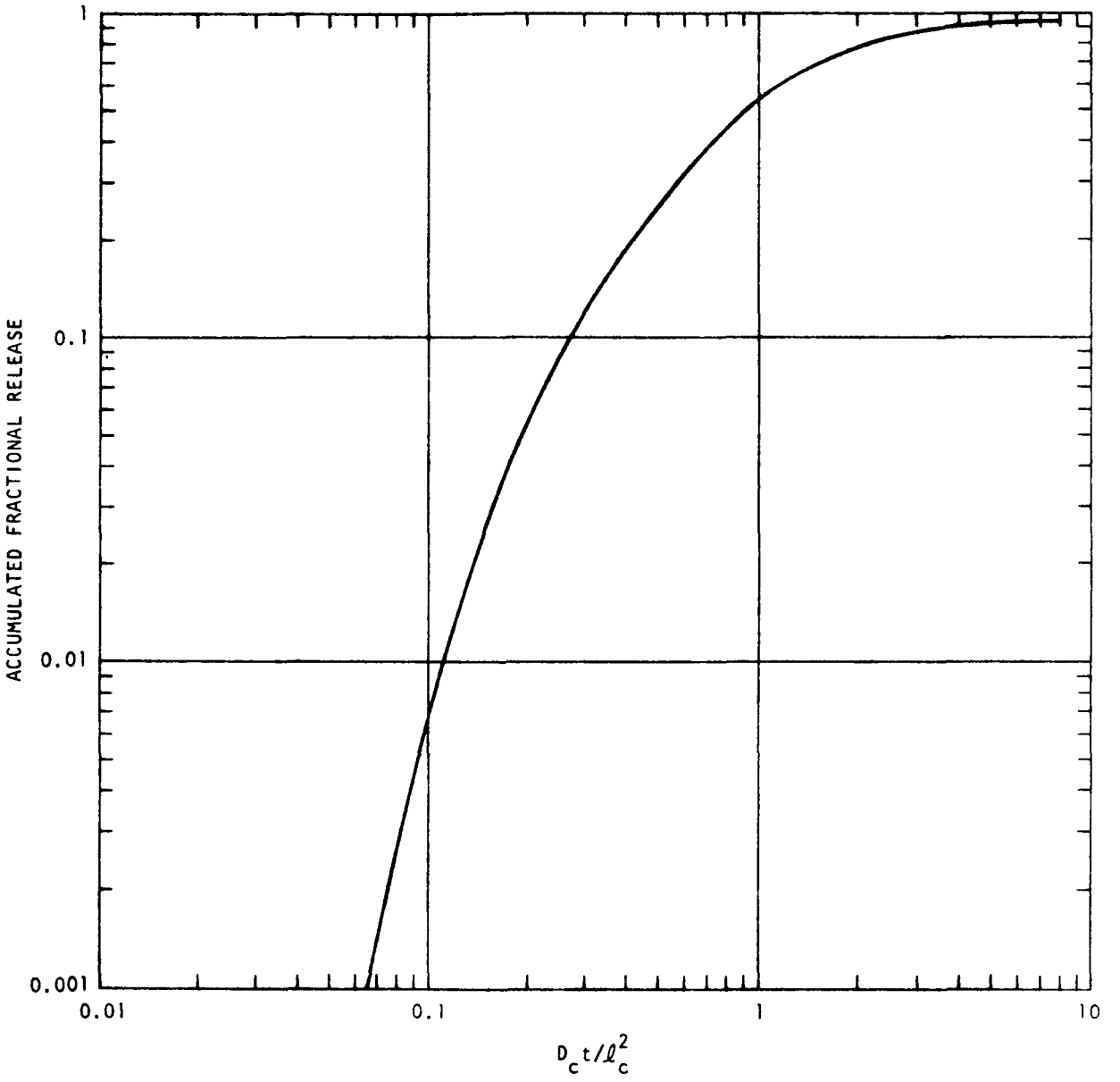

Fig. 4-4. Calculated release of long-lived nuclide from a BISO coated particle assuming coating control and an initial power interval followed by release

In the third case, it was assumed that release is controlled by diffusion in the fuel kernel, the metallic nuclide is produced with no release in an initial time (power) period, and that release with no production (no power) occurs in a following time period. The diffusion coefficient for the pyrolytic carbon coating is taken to be orders of magnitude larger than the diffusion coefficient for the fuel kernel. The calculated curve is shown in Fig. 4-5. In this case the dimensionless quantity is $D_k t/r^2$, where D_k is the diffusion coefficient for the metallic nuclide in the fuel kernel, t is the release time, and r is the radius of the fuel kernel. This case applies, for example, to laboratory (out-of-pile) release of Sr-90 in anneal tests using BISO oxide kernel coated particles irradiated under conditions where no release of Sr-90 occurs.

Included in Fig. 4-5 is a curve resulting from an analytical (hand-calculated) solution. This solution, which serves as a check on the FIPER Q solution, was obtained using Eq. 6.22 in Ref. 4-1. This equation assumes Fick's law diffusion in a sphere of uniform initial and zero surface concentration. The difference between the analytical solution and FIPER Q code solution is explained principally by different source distributions in the kernel and by recoil from the kernel. The FIPER code considers a recoil fraction which is immediately released because of the assumed high diffusion coefficient in the pyrolytic carbon coating. The analytical solution does not consider the recoil fraction. An approximate FIPER Q solution can be obtained by adding a recoil fraction to the analytical solution. This is not a precisely correct procedure since in the analytical solution, depletion of the kernel surface concentration was not considered. Depletion was considered in the FIPER Q solution.

It is of interest to use the curve in Fig. 4-3 to estimate the release of Cs-137 from a hypothetical BISO particle in a reactor for 1200 days at constant power and a constant temperature of 1100°C. On the basis of data from out-of-pile cesium release experiments under way at Gulf General Atomic, $D = 2 \times 10^{-13}$ cm^2/sec at 1100°C. The reference pyrolytic carbon coating thickness is 75 μm. Using these values, one calculates $D_c t/\ell_c^2 = 0.37$, and

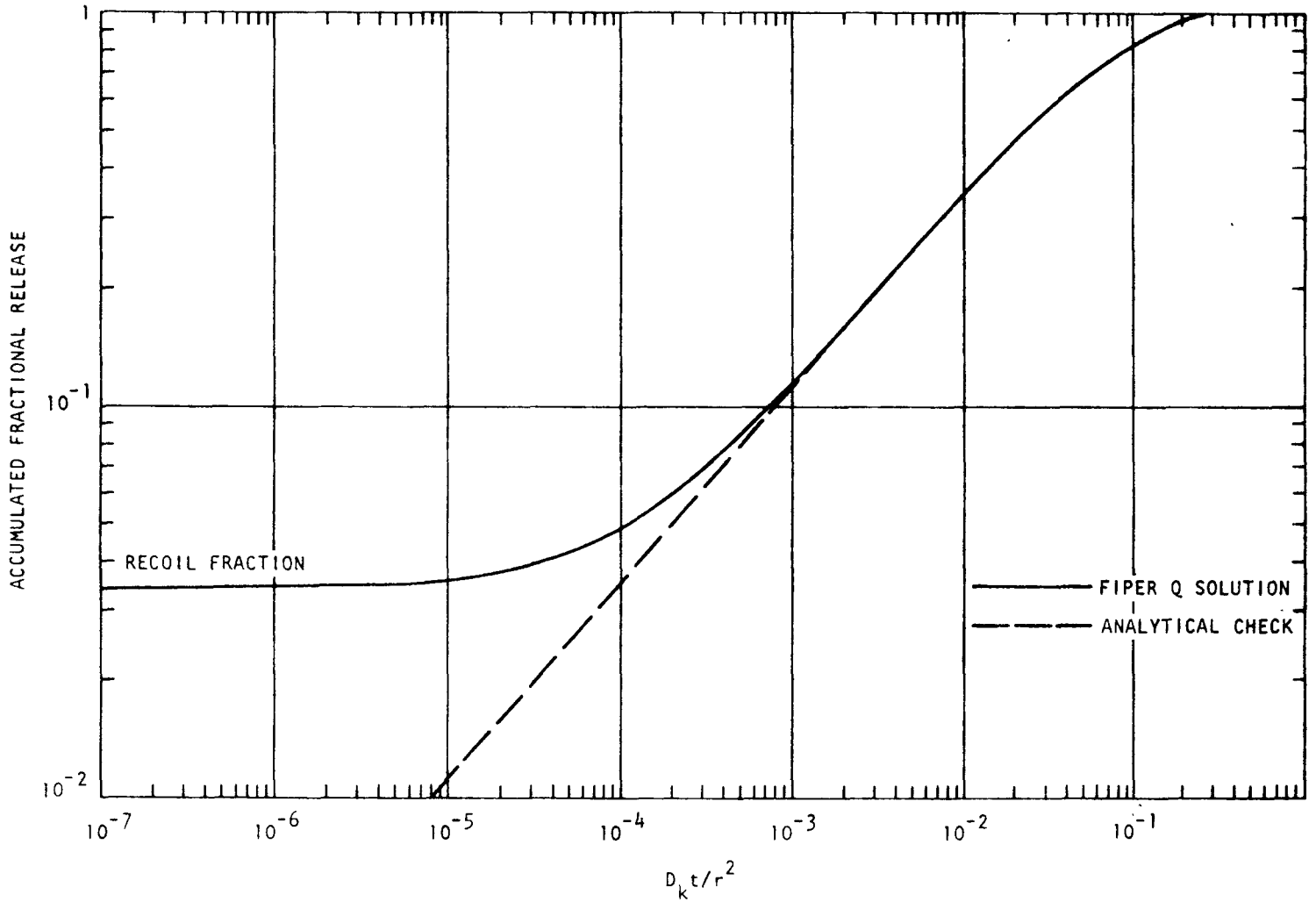

Fig. 4-5. Calculated release of long-lived metallic nuclide from a BISO coated particle assuming kernel control and an initial power interval followed by release

referring to Fig. 4-3, the corresponding fractional release is 0.04. Thus, even at the relatively high fuel temperature of 1100°C, the estimated release of Cs-137 is relatively small.

Figures 4-4 and 4-5 are presently used to model cesium and strontium releases from BISO fuel particles in HTGR core release calculations. Multiple time intervals are treated by a numerical application of Duhamel's superposition principle. This treatment and its application in the FIPER S code are discussed in the previous section on FIPER Code Development (Eqs. 4-40 through 4-50 and accompanying text).

FISSION PRODUCT PLATEOUT AND LIFTOFF STUDIES

A deposition loop, assembled at Gulf General Atomic, is being used to study the plateout characteristics of cesium, strontium, and iodine under conditions similar to HTGR conditions. Helium at 350 psia circulates in the loop with Reynolds numbers of around 15,000 and temperatures varying from 150° to 320°C. The type of steel used for the loop tubing is representative of steel used in the steam generators of HTGRs. Surface temperatures in the loop vary from 200° to 400°C. The source of fission products in the loop is obtained by heating graphite crucibles within the loop that are loaded with the fission products sorbed on graphite matrix material.

The objectives of the loop work are to obtain plateout distribution data and liftoff data by subjecting sections of the loop to conditions of high shear ratios. The plateout data are used to test and refine the PAD code. The liftoff data are used for safety analyses associated with HTGR depressurization accidents.

Experimental work on deposition loop No. 5 was essentially completed during the quarter. Strontium tagged with Sr-85 (a gamma emitter) was the depositing species. The electrically heated source heater was maintained at 800° to 1000°C for 5 days until failure. Very modest quantities of

Sr-35 were released, resulting in counting difficulties. Upon disassembly, it was discovered that about 20 to 30% of the five graphite crucibles containing the source material had disintegrated, and that the loop surfaces were quite dusty.

The most obvious explanation is that the helium used in the loop was contaminated with oxygen and/or water. Considering the high graphite temperatures (∿1000°C) and high strontium loadings (a catalyst for graphite oxidation), graphite corrosion rates would be expected to be high. Preliminary analysis of four spent cylinders indicate a constant water level of 25 ppm and an oxygen level of 40 ppm in half of the cylinders.

Blowdown tests are under way, and the plateout distribution will be determined. The extensive graphite corrosion and subsequent dust generation, as well as poor counting statistics, will make interpretation of this experiment extremely difficult.

REACTION OF STEAM WITH GRAPHITE

The quantitative effect of helium pressure on the reaction rate of H-327 graphite with steam is being investigated over a temperature range of 800° to 1000°C and a helium pressure range of 15 to 750 psia. Data on the helium pressure effect are needed for comparison with theoretical predicitons utilized in analyses of steam in-leakage situations. A description of the apparatus was given in an earlier Quarterly Progress Report (Gulf-GA-A12515).

It was reported previously (Quarterly Progress Report Gulf-GA-A12725) that precise measurements were being hampered by air ingress, high graphite oxidation rates, and carbon transport reactions. Most of these problems have been eliminated by changes in the apparatus. In addition, more accurate temperature control has been provided for, and the temperature of the graphite sample is now monitored by a thermocouple placed directly within the graphite sample.

The reaction rate of H-327 graphite at 900°C and 0.03 atm steam was measured as a function of helium pressure from 60 to 610 psia. The data are plotted on a log-log plot in Fig. 4-6. The negative slope of the line drawn through the data points gives a value for n, the power relationship between reaction rate and helium pressure. From the slope, n = 0.55; this value is in close agreement with the theoretically predicted value of n = 0.5 for this temperature regime. The measured oxidation rates are higher than expected from previous rate studies on H-327 graphite. The cause of these higher rates is being sought.

Additional studies have been carried out in an effort to establish experimental conditions that will yield the most representative data. Results in Fig. 4-6 were measured with nearly a constant helium flow past the sample of 45 cm^3/min. When the total flow through the chamber was maintained at a constant flow rate (i.e., decreasing flow past the sample with increasing pressure), rapid decreases of reaction rate were recorded with increasing pressure, with the slope (n) of the log-log plot of reaction rate versus temperature approaching 1.0. This may result from depletion of steam in the vicinity of the sample, as well as hydrogen buildup, causing inhibition of the reaction. This effect is receiving additional study in current experiments.

REFERENCE

4-1. Crank, J., The Mathematics of Diffusion, Clarendon Press, 1957, p. 87.

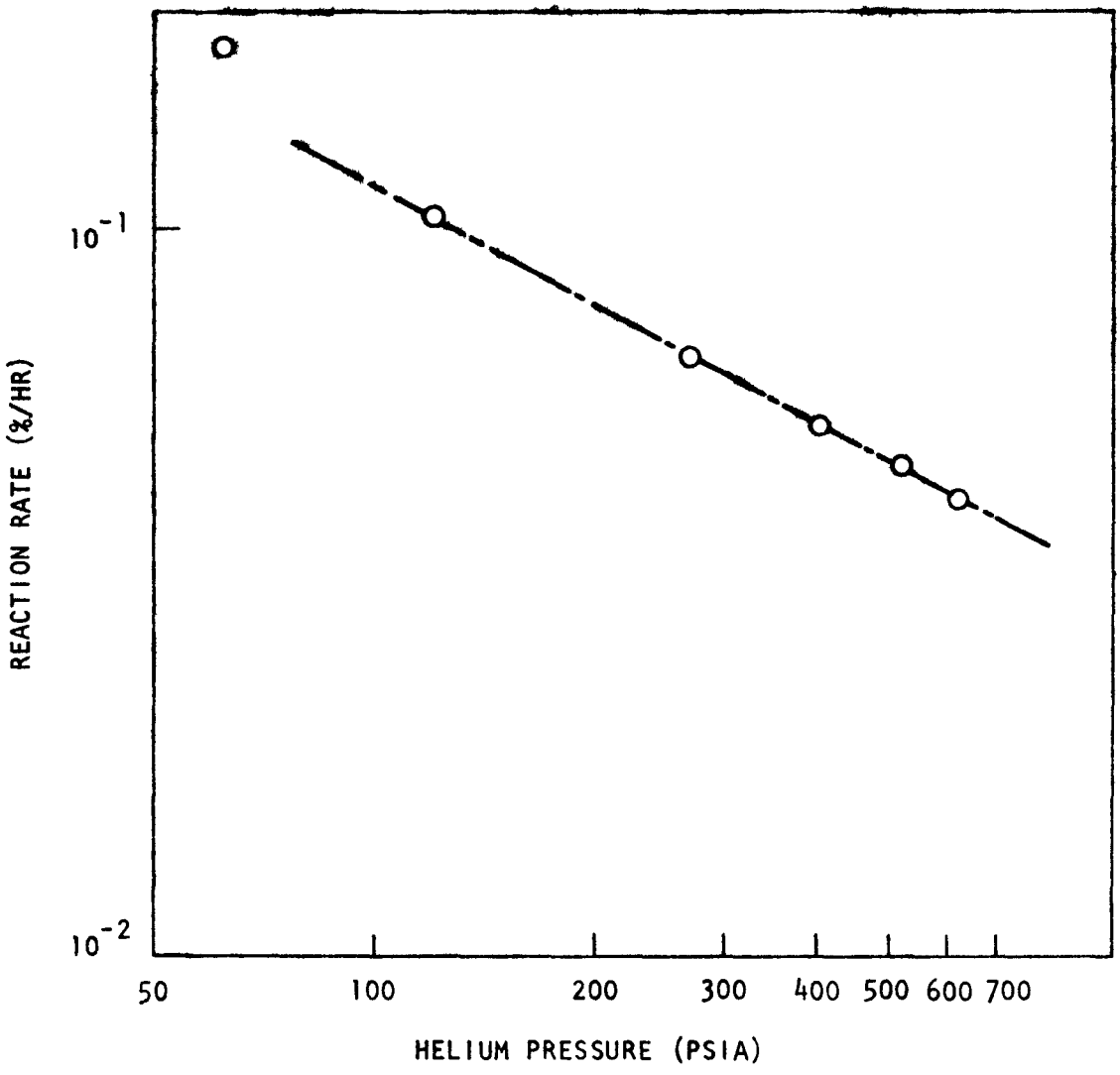

Fig. 4-6. Effect of helium pressure on the rate of reaction of steam with H-327 graphite

TASK V
RECYCLE FUEL STUDIES

HTGR FUEL RECYCLE PLANT STUDY

System Design Description for Cold Pilot Plant

The System Design Description (SDD) for the cold pilot plant will follow RDT Standard F 1-2T, "Preparation of System Design Descriptions." A detailed definition of the contents of the SDD is being reviewed and preparation of Issue A is under way.

Design Criteria for Commercial Reprocessing Plant

Preparation of the Design Criteria for the commercial reprocessing plant has progressed steadily during the quarter. It is anticipated that a first draft will be ready for initial review in mid-November.

Conceptual Flowsheets and Material Balances for Refabrication

Collection of information for preparing a SOLEX refabrication process flowsheet has begun. A preliminary draft of the solution feed preparation and extraction portions of the flowsheet has been completed. Principal material balances, process conditions, and equipment volumes and types are being indicated for 20,000 refabricated fuel elements per year.

Liaison with National Laboratories and AEC

Plans for the hot demonstration facility for HTGR fuel reprocessing have been reviewed with personnel at the Idaho Chemical Processing Plant

(ICPP). ICPP has provided GGA with a list of development needs for design of the HTGR fuel reprocessing plant and their required timing.

The following topics were discussed with ORNL representatives:

1. Whole-block burning development.

2. Comparative layouts of a commercial reprocessing plant using both whole-block burning and fluidized bed burning techniques.

3. Processes for use in the TURF demonstration.

4. Potential capability of reprocessed, recycled U-235 fuels for contact fabrication without shielding.

Work was done on the preparation of a draft standard entitled, "Design for the Decommissioning of Nuclear Fuel Reprocessing Plants," at a meeting of ANSI subcommittee N46.5.10.

HEAD-END REPROCESSING

Summary

Whole-block crushing tests are continuing. Characterization of crusher product and crusher modifications continue to show promise. Testing of a tertiary stage roll crusher has been initiated, and a large double-roll tertiary stage crusher has been ordered for comparative studies.

Installation of the pneumatic transport systems for crusher system product, primary burner product, and secondary burner product has been started. The installation of the air-classifier apparatus for particle separation is included in the installation of the pneumatic transport systems.

Modification of the primary and secondary burners continued. The 10-cm primary burner was not operated due to problems associated with delivery and operation of the new control system. The secondary burner was used to test batch burning of primary burner type feed, to burn back whole particles, and to burn particles which had the SiC shell cracked off of the kernel. New double-roll particle crushers were used to evaluate the effect of gap size on the product size distribution and the effect of different sized feed to the secondary burner.

ThO_2 sol-gel particles were processed in the leaching system to establish operating characteristics with this type of material. It was established that essentially 100% thorium recovery could be obtained in less than 2 hours on sol-gel ThO_2 that had been crushed in a double-roll crusher. Uncrushed ThO_2 sol-gel required 16 hours for complete dissolution.

Crushing

Primary Crusher

Two standard control-rod fuel elements were reduced in the primary crusher. These fuel elements were crushed in the vertical-captured position with a fixed discharge setting. The resulting crushed product is presently being analyzed to determine cumulative size and shape distributions [the terms size and shape were defined in the previous Quarterly Progress Report (Gulf-GA-A12725)].

Secondary Crusher

Some minor modifications were made to the crushing cavity of the secondary crusher to obtain a slightly higher size-reduction ratio than has been previously used. The modification involved placing a shim on the stationary jaw plate, which reduced the discharge opening.

Tertiary Crusher

The tertiary crusher has been received and a few preliminary tests have been performed. The machine consists of a single roll mounted on a rotating eccentric shaft. The roll is situated between two stationary crushing plates, the shapes of which asymptotically conform to the curvature of the roll. Figure 5-1 relates the physical arrangements of the various machine elements; details are shown in Fig. 5-2. The major components called-out in Figs. 5-1 and 5-2 are identified in Table 5-1.

A double-roll (18-in. diameter x 14 in. wide) crusher has been ordered. This machine, when operational, will be used to determine if a net comparative advantage exists over the single-roll crusher described above. The comparative advantages to be determined will be based on (1) minimizing fuel particle breakage, and (2) suitability of the crusher(s) for a remote facility.

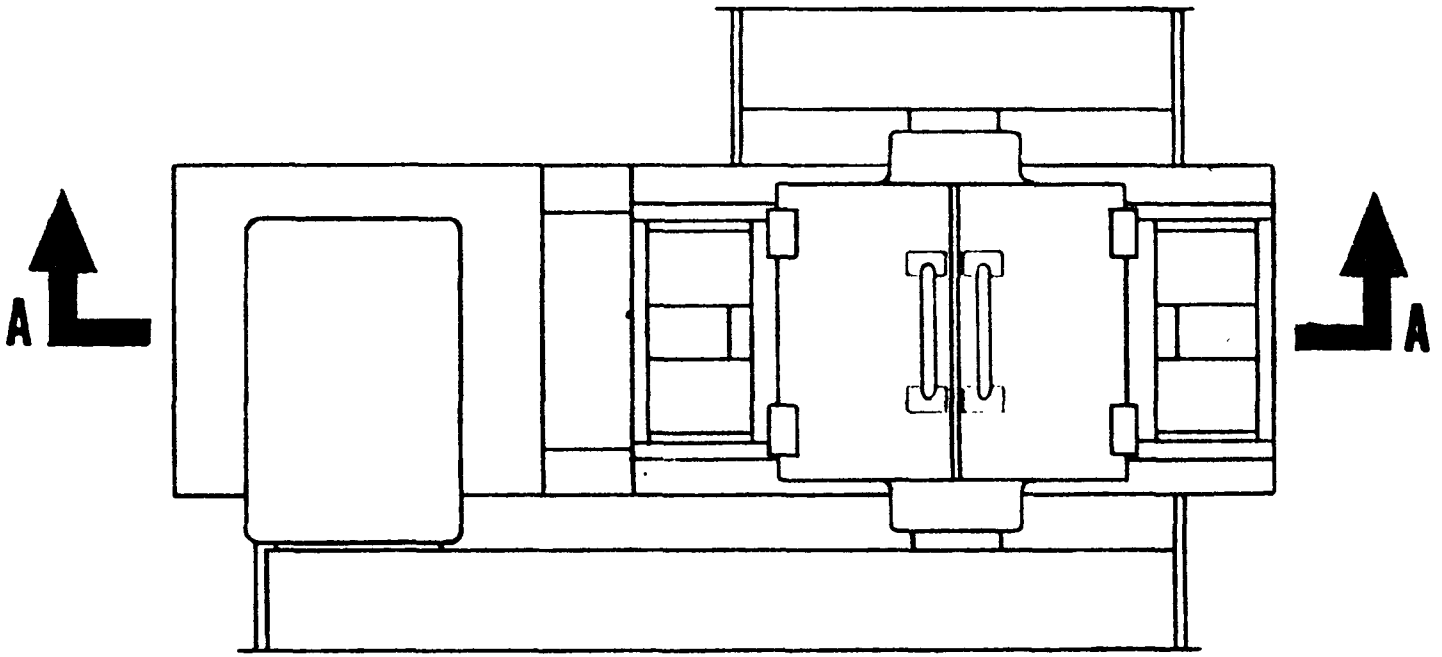

Fig. 5-1. Physical arrangement of tertiary crusher, top view

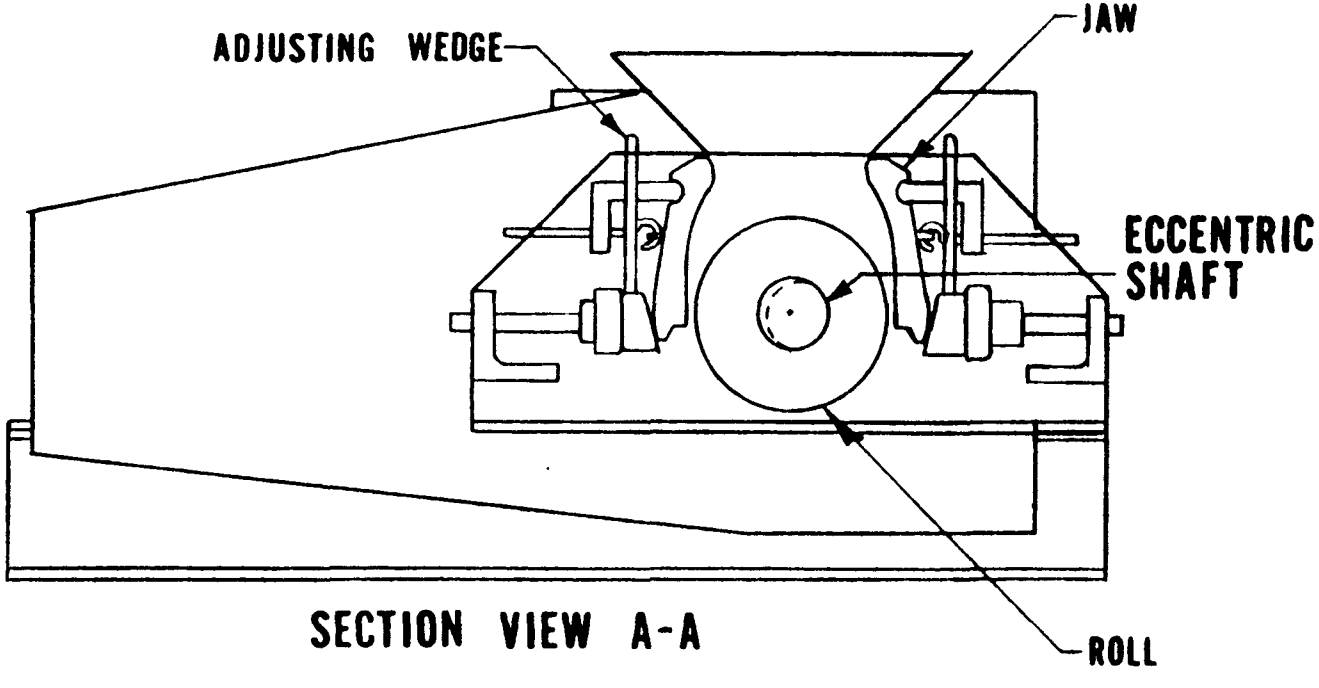

Fig. 5-2. Details of tertiary crusher

TABLE 5-1
PARTS LIST FOR "CENTEROL" CRUSHER

No.[a]	Description	No.	Description
1	Base, crusher	29	3/4 Lockwasher
2	Frame	30	3/4-10 UNC locknut NE
3	5/8-11 UNC x 2 LG HHCS	31	Wedge, adjusting
4	5/8 lockwasher	32	Screw, adjusting
5	5/8-11 UNC locknut NE	33	Washer, Spher
6	Shaft, eccentric	34	5/8-11 UNC SPA FLG nut
7	Roll	35	Jaw
8	BRG, SJ 9568 S	36	Eyebolt
9	BRG, IR 9568	37	Spring, compression
10	Seal P/N 27379	38	5/16 washer
11	Retainer, roll seal	39	5/16-18 UNC locknut NE
12	3/8-16 UNC x 1-in. LG SHCS NYLK	40	Motor, FR 184T
13	Cheekplate	41	3/8-16 UNC x 1-3/4 LG HHCS
14	1/2-13 UNC x 2 LG FHCS	42	3/8 lockwasher
15	1/2 lockwasher	43	3/8-16 UNC locknut NE
16	1/2-13 UNC hex locknut NE	44	Guard, flywheel
17	Seal P/N 24991 type FI	45	3/8-16 UNC x 1-in. LG HHCS
18	Retainer, frameseal	46	Guard, drive
19	BRG, FLG P/N FB 22439H	47	Sheave
20	BRG, FLG P/N FEB 22439H	48	V-Belt (matched set)
21	1/4 DIAM. x 1-3/4 LG SPR PIN	49	Hopper, feed
22	5/8-11 UNC x 1-3/4 LG SHCS NYLK	50	5/16-18 UNC x 3/4 HHCS NYLK
23	1/8 grease fitting 1610BL	51	Cover, flywheel guard
24	S/A sheave	52	1/4-20 UNC x 3/4 LG HHB
25	Key, flat 5/8 x 7/16 x 2-1/2	53	1/4 lockwasher
26	Guide, spring	54	1/4-20 UNC hex nut
27	3/4-10 UNC x 7 LG SQHB	55	Cover, drive guard
28	Spring, compression		

[a] Numbers correspond to those in Figs. 5-1 and 5-2.

Solids Handling

Pneumatic Transport Systems

The positive displacement blowers for each of the three subsystems described in the previous Quarterly Progress Report (Gulf-GA-A12725) have been received. Installation of these units is expected prior to receipt of the remainder of the system.

Pneumatic Feeder for Primary Burner

The pneumatic feeder previously described (Gulf-GA-A12725) has been constructed. Experiments indicated that the following changes from the original conceptual description should be made:

1. The funnel-flow, 60° offset hopper was discarded and a mass flow type hopper was substituted.

2. The blow-through feeder was abandoned in favor of a venturi or flow-nozzle type pickup.

The first change was introduced to decrease particle segregation and thereby improve the consistency of flow to the drop-through feeder. The second change was suggested by the fact that flow required to generate a sufficient pickup velocity for the largest particle (3/16 in.) was much greater than the inert gas flow allowed for pneumatic feeding to the 8-in. primary burner. (The concept remains viable for the prototype burner, however.) Evaluation of the above changes is continuing.

Air Classification and Particle Crushing

The air classifier and two particle crushers previously reported as on order have been received. Installation of these pieces of equipment is proceeding so as to experimentally evaluate the previously outlined flow

diagram (Fig. 5-9 of previous Quarterly Progress Report Gulf-GA-A12725) for particle classification and crushing.

Primary Fluidized-Bed Burner

The 10-cm primary fluidized-bed burner was not operated during the past quarter because of construction of an improved auger feed system and problems with the new control system.

The new bottom feeder is shown in Fig. 5-3. The new top feeder, which can either feed the burner directly or add fresh feed to the bottom hopper along with the elutriated material collected in the cyclone, is shown in Fig. 5-4. The new auger systems were installed to provide a more reliable feed system and also to lower particle breakage. Figure 5-5 shows the output and particle breakage of these new augers. The performance of this system appears satisfactory. An analysis of the auger feed system, former problems, and the basis of the new system can be found in the previous Quarterly Progress Report (Gulf-GA-A12725). Figure 5-13 of that report shows the present 10-cm burner configuration.

Delivery of the new control system was delayed; however, the burner should be operational early in the next quarter.

Batch Primary Burning

The batch operating concept takes into consideration requirements for accountability and separation of fuel types. By using in-vessel filters to contain fines, the equipment associated with the primary burning operation (defined as burning the crushed fuel elements down to particles) would be greatly simplified by eliminating the equipment presently used to handle fines. Conceptually the run would operate until the bed of particles was built to an arbitrary size, the flow rate would be lowered to allow burning the fines, and the batch would then be dumped. This would eliminate the need for a bed size control loop.

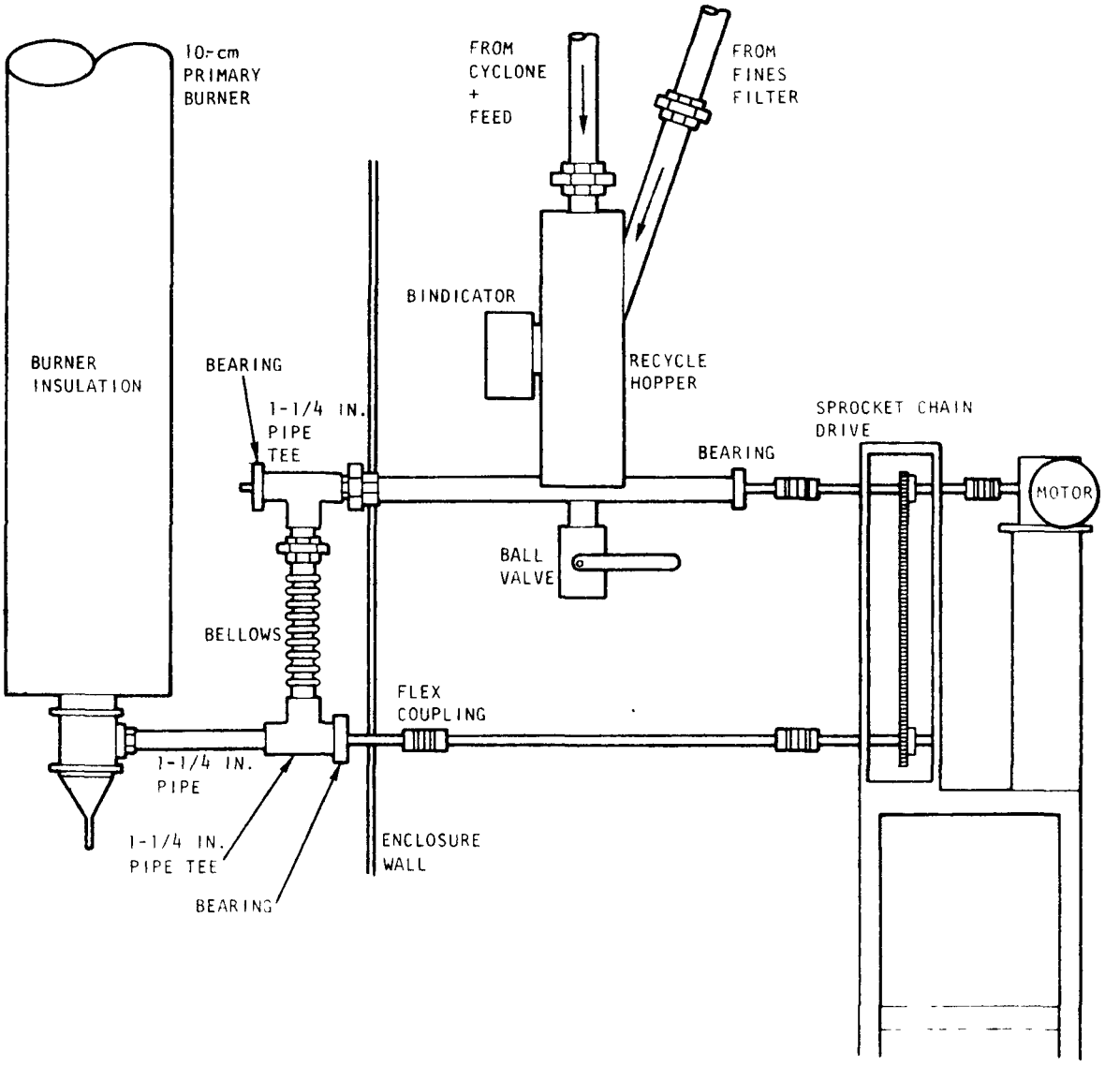

Fig. 5-3. Recycle auger system

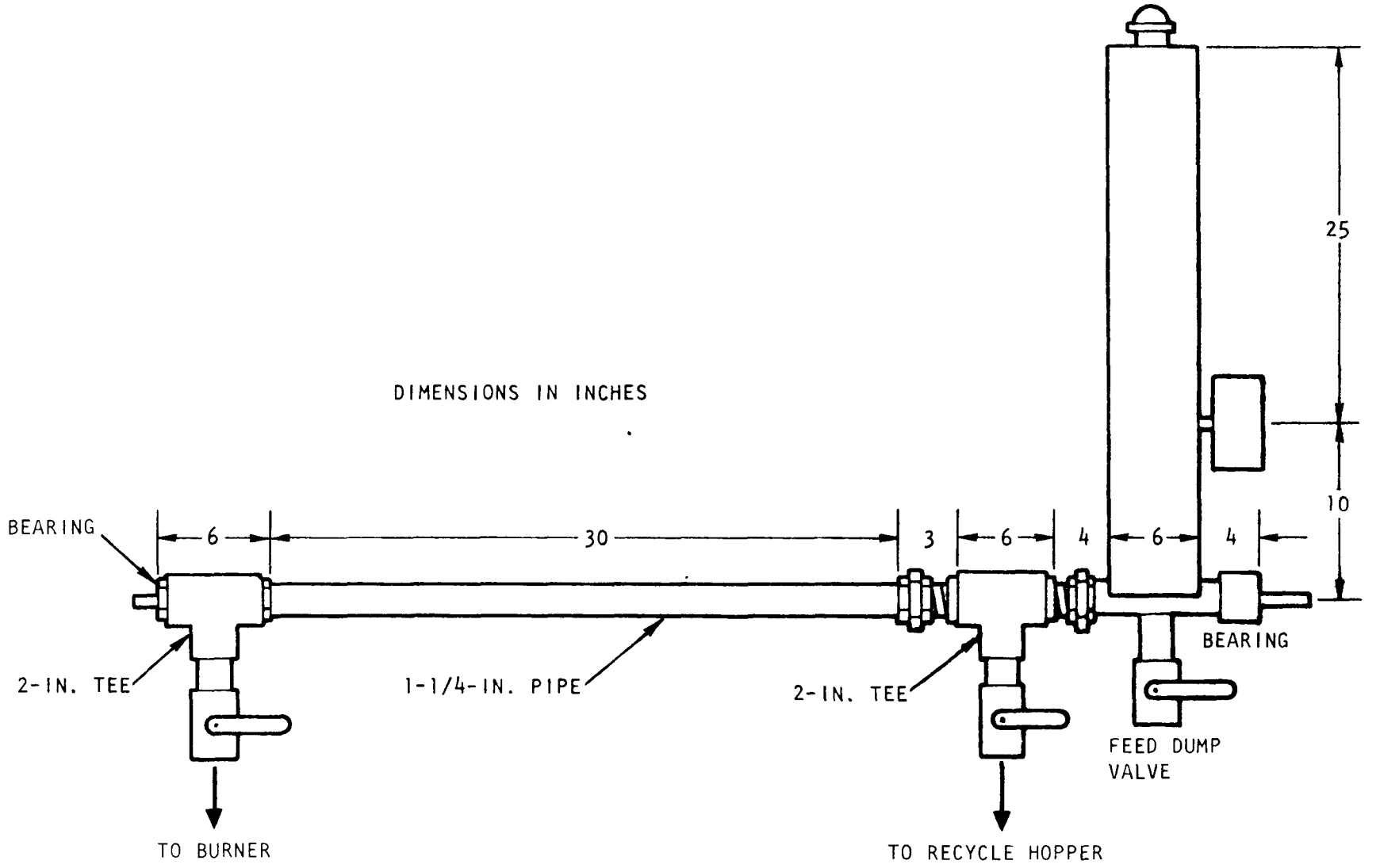

Fig. 5-4. Extended feed auger system, 7/8-in. by 50-in. core auger

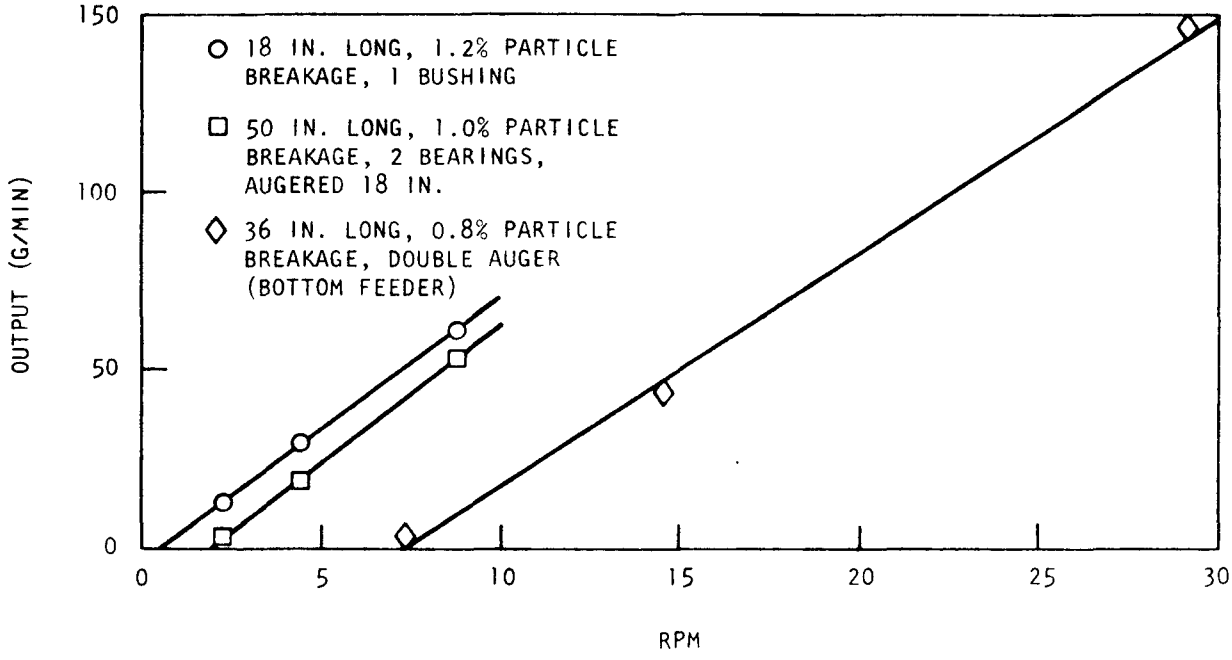

Fig. 5-5. 10-cm primary burner auger performance (installed), 7/8-in. core auger in a 1-1/4-in.-diameter barrel

The initial test of this concept was made using a "whole bed" startup technique - feeding 5 kg of fresh feed to a hot burner tube (950°C). Two run attempts were made in the 10-cm "secondary burner" tube (Fig. 5-6) using the pneumatic feeder and a distributor plate (Fig. 5-9, Gulf-GA-A12515). In both attempts the bed segregated during startup, with the static bed burning at the bottom of the burner. Hot spots formed, which resulted in the formation of agglomerates and failure of burner components. It was concluded that "whole-bed" startup was not possible with the present burner configuration. Further tests will be made of the batch burner concept using an alternative startup technique. These tests will be used to establish the concept and to evaluate the batch size (i.e., how much feed can be burned before the fines buildup causes operational problems).

Secondary Fluidized-Bed Burner

Heating and Cooling Evaluation

Reprocessing HTGR fuel entails a secondary burning operation in which crushed fuel particles are burned to remove excess carbon (from coatings and residual matrix) and to oxidize the ThC_2 and UC_2 kernels. The method chosen to effect this combustion is a batch fluidized-bed burner. Operating procedures include introducing a cold batch of crushed fuel particles, heating them to their ignition temperature (approximately 700°C for appreciable combustive heat generation), burning them in a stream of O_2, and removing the ash at the end of combustion. This cycle is immediately followed by another in order to utilize the heat stored in the burner walls for quicker startup, thus increasing the overall capacity of the burner.

To maximize throughput, the burner must be capable of heating the bed quickly during startup and cooling the bed sufficiently during combustion. Two candidate processes for achieving these requirements have been evaluated: (1) resistance heating with jacketed air cooling of the upper portion of the burner (see Fig. 5-7), and (2) induction heating with a full-length air cooling jacket (see Fig. 5-8).

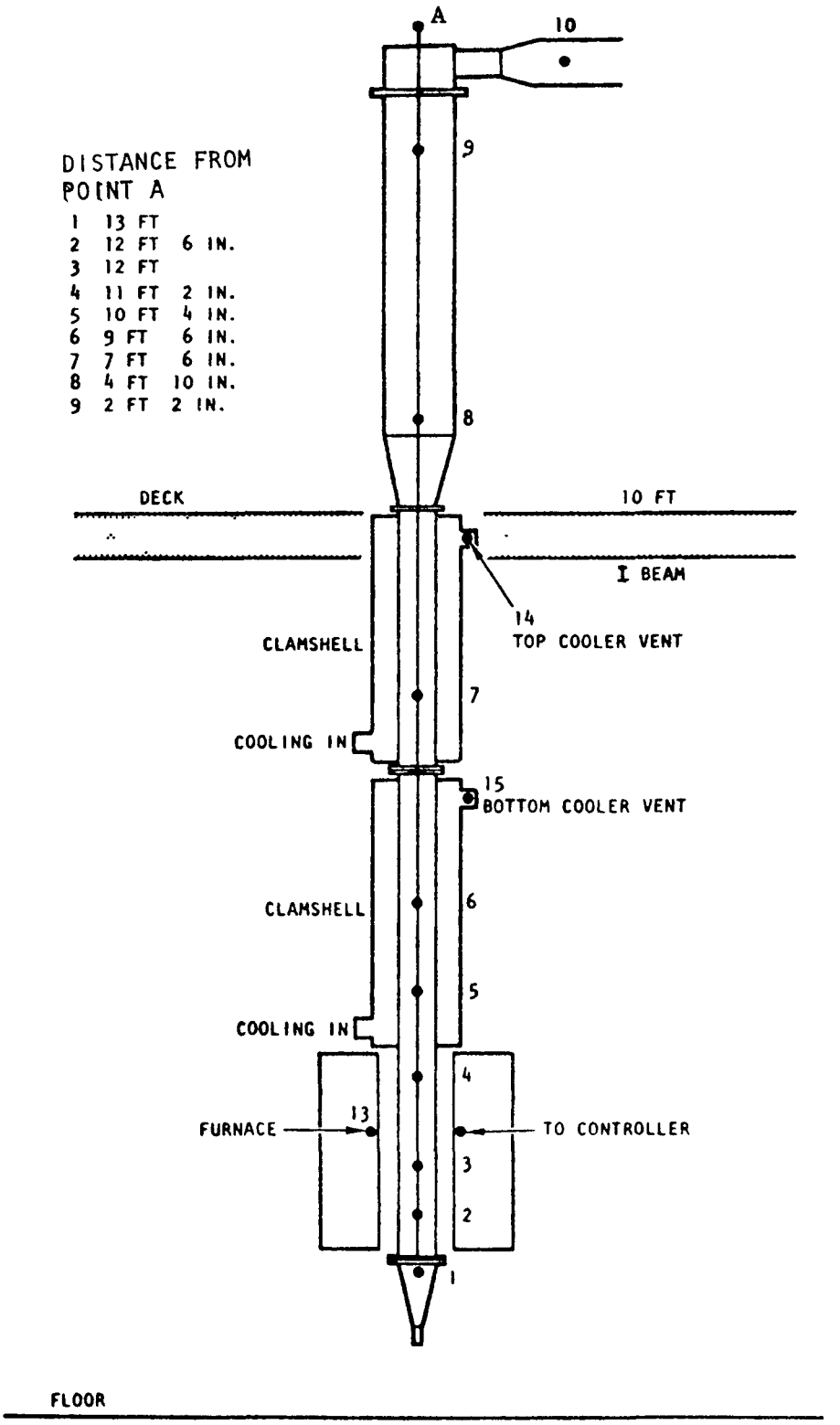

Fig. 5-6. 10-cm secondary burner layout

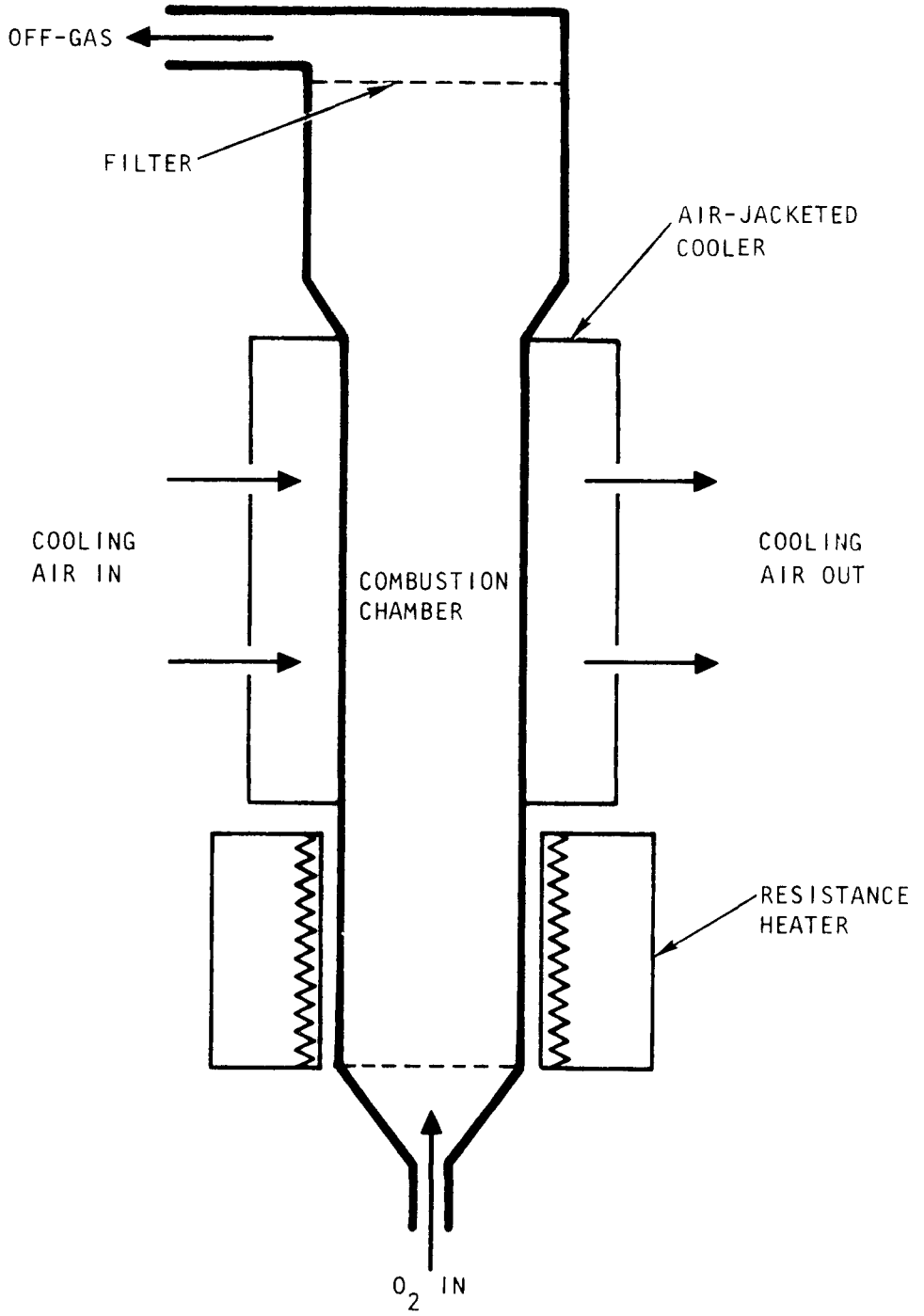

Fig. 5-7. Cross section of resistance-heated secondary burner

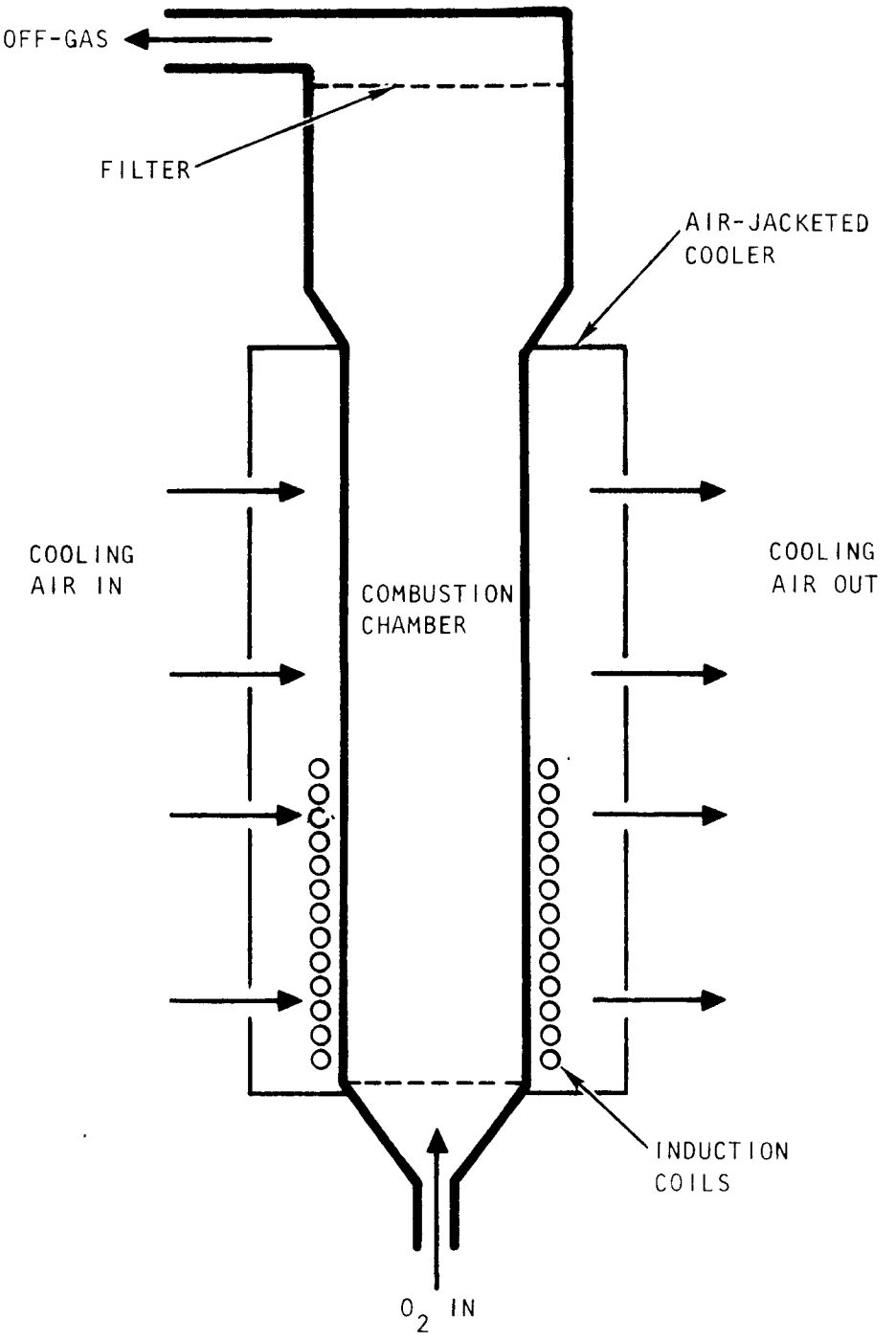

Fig. 5-8. Cross section of induction-heated secondary burner

Resistance Heating. A resistance heater transfers heat from the heating element (Kanthal resistor wire - an Al-Cr-Co-Fe alloy - embedded in a refractory cement) to the reactor tube via radiation and natural convection. Tests on a 10-cm-diameter (4 in.) burner with a 6 kW, 50-cm high furnace indicate that heating from 300°C (temperature after bed is added to burner) to 700°C (approximate bed ignition temperature) takes 25 minutes.

Heatup time has been extrapolated to apply to a 25-cm secondary burner according to the assumptions listed below:

1. Area for heat transfer is proportional to D (burner diameter).

2. System heat capacity (ΣmC_p) is proportional to D^2.

3. Furnace heating capacity (Q) is proportional to heat transfer area.

4. Bed heating rate is proportional to $Q/\Sigma mC_p$.

From these assumptions, it can be seen that heatup time t is directly proportional to burner diameter D. Therefore, the anticipated heatup time of a 25-cm secondary burner from 300° to 700°C is 63 minutes.

Normal operation of the secondary burner requires thermal cycling (300° to 1000°C) which, in the case of resistance heaters, imposes severe thermal and mechanical stresses. The thermal stresses lead to fracturing of the ceramic material in which the resistance (Kanthal) heater is buried. Once the ceramic protective material is fractured, the resistance wire is subjected to rapid oxidation. Mechanical stresses arise when the wire is required to hold adjacent pieces of ceramic together, resulting in wire breakage and subsequent loss of power. Cracking of the elements is expected to be a major maintenance problem causing significant cell downtime.

Capital cost of a resistance heater for a 25-cm secondary burner would be approximately $10,000. The cost of replacing elements in the cell is not known. At least several days of downtime would be necessary any time an element failed.

Induction Heating. An induction heating system, as illustrated in Figs. 5-8 and 5-9, uses an alternating magnetic field to induce currents in the burner wall. This flow of induced current generates resistive heat in the tube itself.

For efficient electrical supply, the capacitors shown in Fig. 5-9 must be located within a few feet of the work load. This means shielding oil-fitted capacitors from hot cell radiation.

For the nonmagnetic high-temperature burner tube metals under consideration, a 10 kHz induction current supply would yield a suitable depth of heat penetration, assuming approximately 0.25-in.-thick tube walls.

The effect of using a welded Hastelloy X burner tube with an induction heater has been investigated. It was concluded that there are no significant differences in tube life when heated by either induction or resistance heaters. It was also determined that Hastelloy X is a suitable metal for use as a burner tube.

Induction heaters are often used when rapid heating to high temperature is required. Heating rates are limited by the thermal conductivity of the tube wall. To determine the tube wall gradients that will be encountered, the following model is assumed:

1. The burner tube is 4-in., No. 40 Hastelloy X pipe; C_p = 0.15 cal/g-°C; k = 0.2 W-cm/cm^2-°C; heated zone weight = 15 kg (100-cm length); heated zone surface area = 3600 cm^2; wall thickness = 0.64 cm.

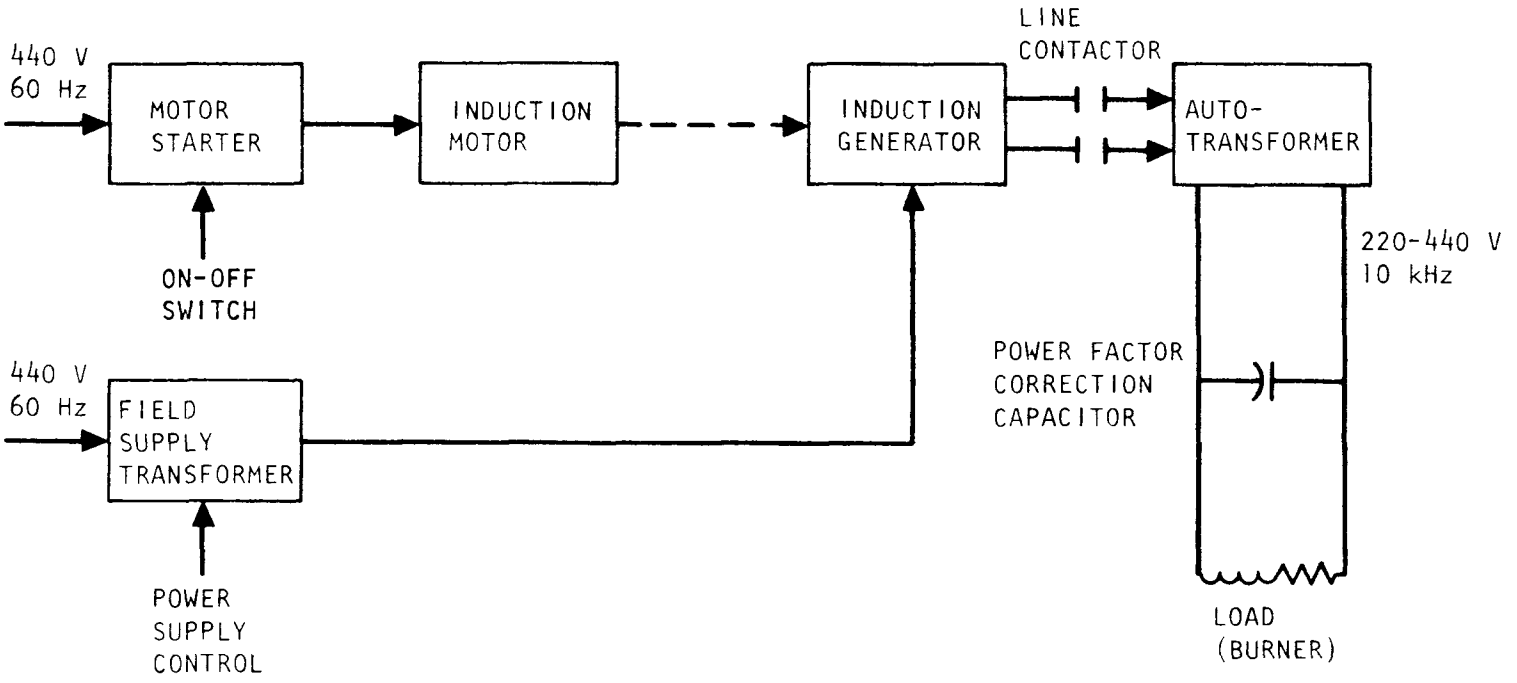

Fig. 5-9. Typical induction heating system

2. The bed has a mass of 10 kg and C_p = 0.024 cal/g-°C.

3. All heat enters the tube wall at the outside surface.

4. Required heating rate is 100°C/minute, or startup in about 5 minutes.

Using the heat conduction equation

$$Q = kA\Delta T/L,$$

where Q = heating rate, W
k = thermal conductivity, W-cm/cm^2°C
ΔT = tube wall temperature gradient, °C
L = tube thickness, cm
A = tube surface area, cm^2

then ΔT = 16°C, which is very small.

Performing a similar calculation on a 25-cm secondary burner indicates that heating from 300° to 700°C in 10 minutes yields a 10°C tube wall temperature gradient. This heating rate would require 25 kW of induced power.

The capital cost of an induction heater for a 10-in. burner would be approximately $15,000. Maintenance problems would be minimal.

Cooling. As seen in Fig. 5-7, the bottom of the present burner is located at the same level as the bottom of the resistance furnace, which keeps the bed in the hot zone so that it can be heated during startup. The maximum bed sizes used to date are such that the fluidized bed is entirely contained in the heated zone. This means that during the burning stage, air-jacketed cooling can only be effected on burned walls that are not in contact with the bed. Thus, the wall is much cooler than where the bed is

contained, yielding less heat flow per unit surface area. Less heat removal capability means a lower maximum burn rate and longer cycle times.

Average burn rates to date in the 10-cm secondary burner are about 40 g carbon/minute. Higher burn rates are not permitted due to high temperature alarms (>1000°C centerline bed temperature), indicating that the burn rate is limited by heat removal capability.

It is anticipated that air jacketing the entire length of the 10-cm secondary burner, which is possible with an induction heating system (see Fig. 5-8), would increase the average burn rate to approximately 70 g carbon/minute. This is a significant improvement in heat removal capability and would substantially decrease burning time.

Conclusions and Future Work. Based on the arguments presented, an induction heating system has been ordered for testing on the 10-cm secondary fluid-bed burner. It will be fully air jacketed to provide maximum burner cooling capability.

A Hastelloy X welded seam burner tube (10-cm-i.d., 0.63-cm wall thickness) has been ordered to replace the stainless steel tube (0.25-cm wall thickness) presently used. This new tube will be a suitable susceptor for the induction heating coil.

Particle Crushing System

A system to crush TRISO fuel particles has been fabricated in line with the 10-cm secondary fluid-bed burner. This system serves to supply crushed material for burner runs.

The system consists of two parallel crushers, one with a 430 μ (0.017 in.) gap and the other with a 300 μ (0.015 in.) gap. The rolls are 2.5 cm (1.0 in.) wide and 7.5 cm (3.0 in.) in diameter. Crushed material can either be sampled or fed directly into the 10-cm secondary burner feed hopper.

TRISO fertile particles have been crushed through each crusher (see Fig. 5-10 for size distribution) and through both in series. The resulting product is interesting in that over 75% of the ThC_2 kernels remained whole. The previously used 300 μ (0.012 in.) gap particle crusher did not produce whole kernels. This larger particle size product is less dusty and flows more easily than the previous product.

Burner Alignment

As reported in the previous Quarterly Report (Gulf-GA-A12725), burner alignment mechanisms have been installed on the bottom flange of the 10-cm secondary burner (see Fig. 5-11). During the course of four different burner runs (in which the burner expanded 3 cm vertically between cold and hot operation), these mechanisms worked very smoothly with no binding. They succeeded in limiting the burner tube to vertical movement only, thus eliminating any "kinking' of the tube or oscillatory displacement previously associated with an unbraced tube containing a slugging fluid bed.

Whole Particle Burning

Two combustion tests were run using whole (uncrushed) BISO-ThO_2 fuel particles. Acceptable product was produced during both tests, although the first test product required screening to remove fine carbon dust (see Table 5-2).

During the first test, the bed removal* was incomplete. The initial 80% of the bed was emptied in less than 2 minutes, but the remainder mounded onto the distributor plate and would not fluidize. This can be accounted for by either of the two following mechanisms:

1. The bed was not expanded enough to leave through the open valve port.

*Using the high-temperature bed removal system described in previous Quarterly Progress Report Gulf-GA-A12725.

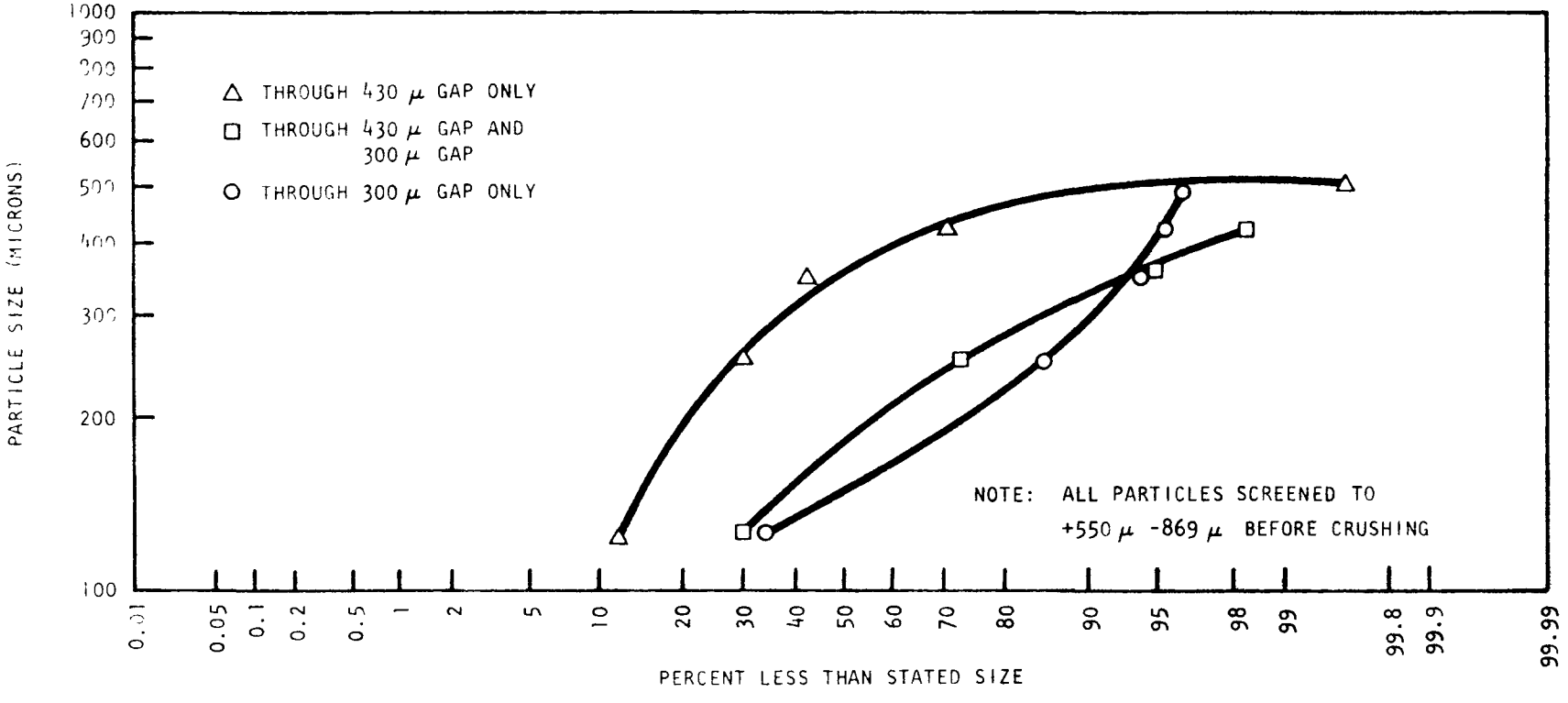

Fig. 5-10. Size distribution for particle crushing system

TABLE 5-2
SUMMARY OF BISO-ThO_2 BURN-BACK TESTS[a]

	Test I	Test II
Feed weight, g	8,127	10,443
Carbon in feed (approximate, via sample), %	38	36
Product weight, g	4,852	6,320
Product removed through valve port, %	82	98
Total combustion time, min	125	180

[a] Burned-back particle density $\simeq$ 10 g/cm^3
Burned-back particle size $\simeq$ 100 μm

2. The bed was static (piled in mounds between holes in the distributor plate) and thus had no gas passing through to fluidize it.

The second test was more successful. Greater than 98% cleanout was accomplished in 1 minute. This product contained no carbon (by visual examination). Subsequent inspection of the distributor plate revealed a mound of approximately 100 g of kernels and fine carbon. This was a substantial reduction in the quantity of "heel." Changes in removal procedures included higher temperature and greater gas flow through the distributor plate. This cause-effect relationship could support either of the previously proposed mechanisms.

A 5-kg batch of fissile-size TRISO coated depleted UC_2 particles was burned back to the SiC coating. These are for use in leaching and air classification studies as "dummy" fissile particles. This run proceeded smoothly and acceptable product was obtained.

Crushed Particle Burning

One run (F4RHB-M24) has been made to test the particle crushing system and the high-temperature bed removal system (see Figs. 5-11 and 5-12) with TRISO fertile particles. Due to an inadequate electric motor for particle crushing, only about 5 kg were crushed and burned. Size distributions of burner feed and product are shown in Fig. 5-13.

The particle crusher used was the 430-μ gap double-roll crusher. The power supply was a 1/8-hp, 29-rpm electric motor producing ~100 in.-lb torque. Both the gearbox and the motor overheated before the motor failed, indicating overload. Subsequent tests with a 1/2-hp motor yielding 500 in.-lb torque have been successful with no motor failure.

The combustion went smoothly with complete burnout (<0.1% carbon in product). Fines were burned at the close of the run by lowering the total

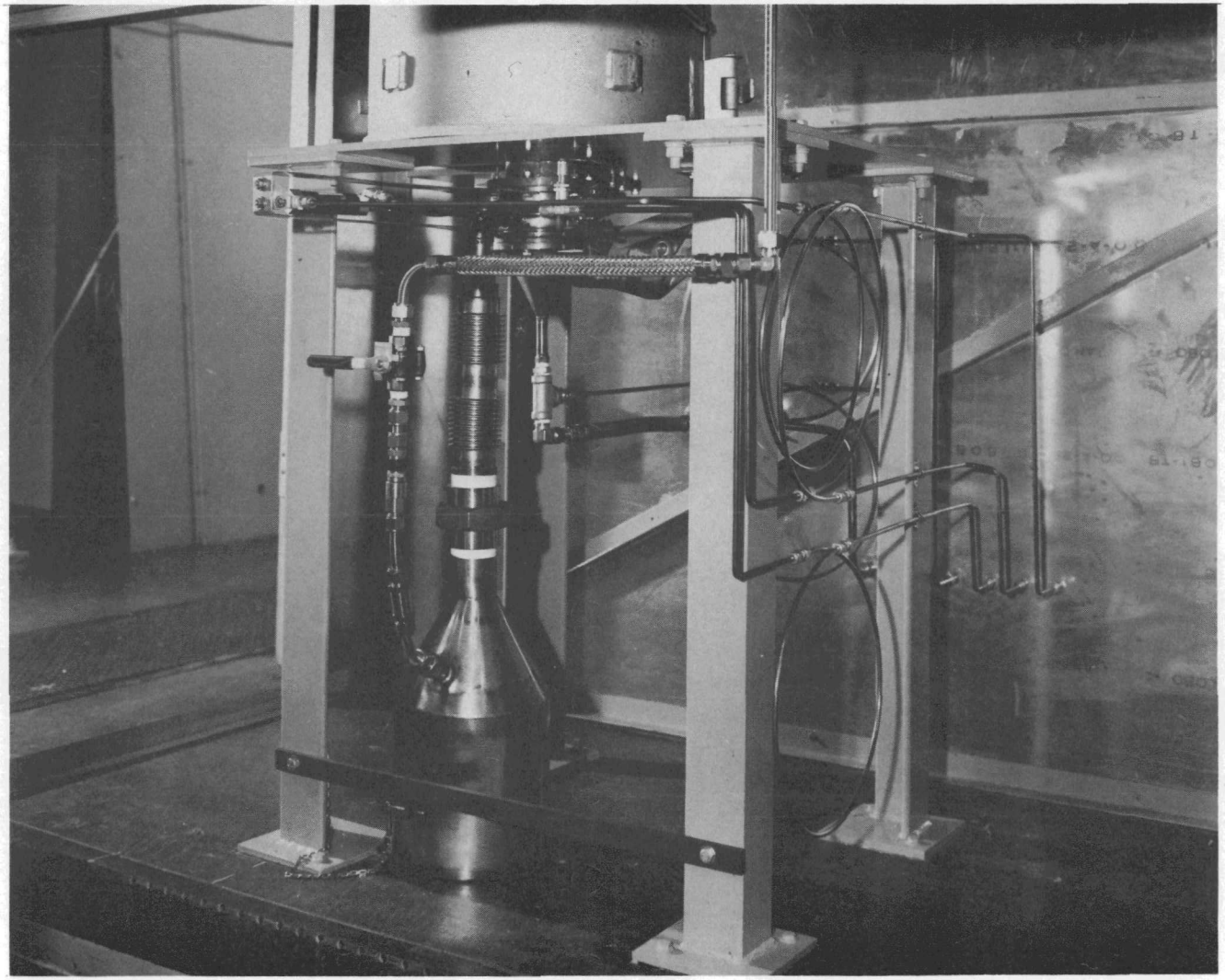

73HT770

Fig. 5-11. Lower section of 10-cm secondary burner showing high-temperature bed removal system and burner alignment mechanisms

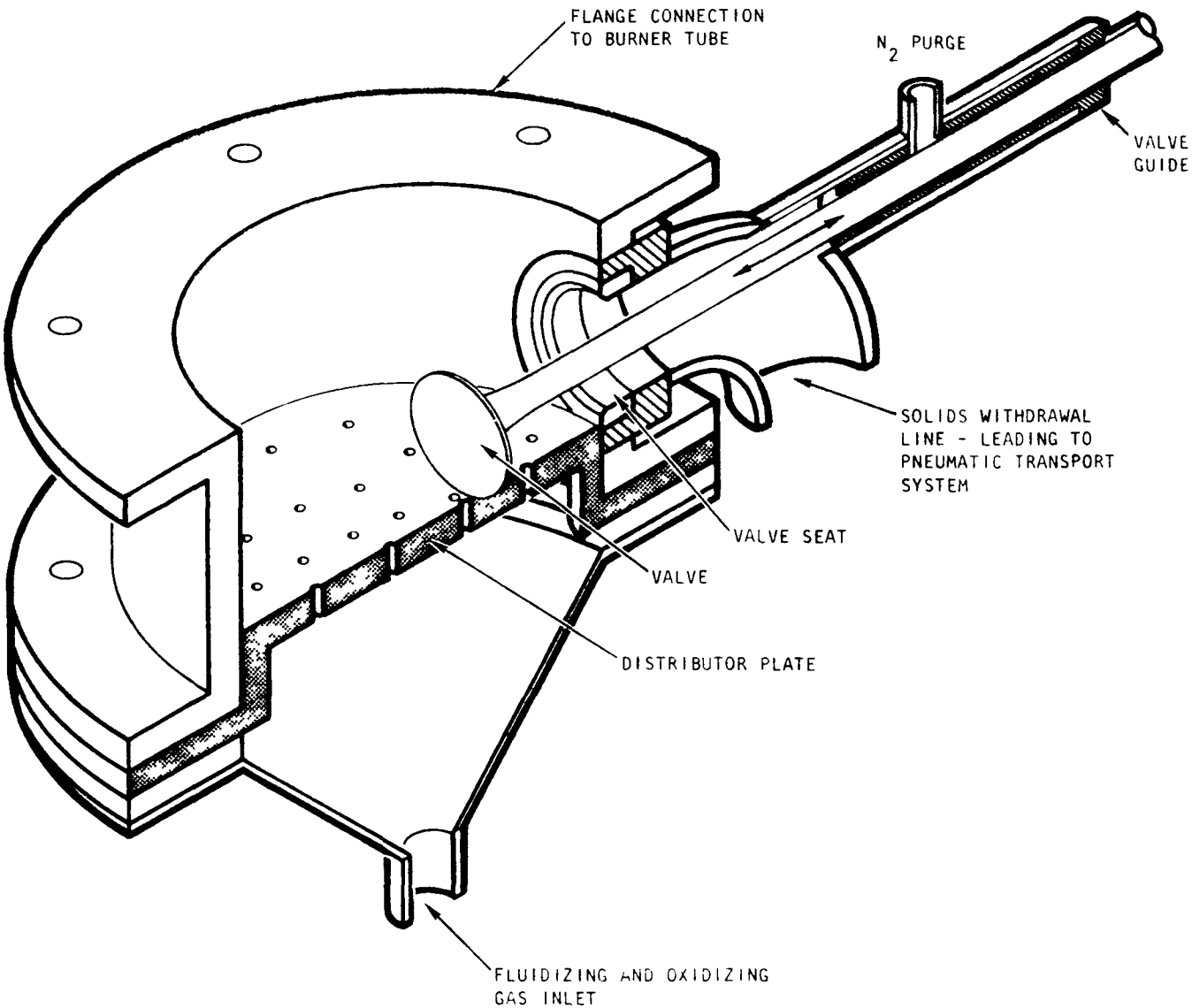

Fig. 5-12. High-temperature bed removal system for 10-cm secondary fluid bed burner

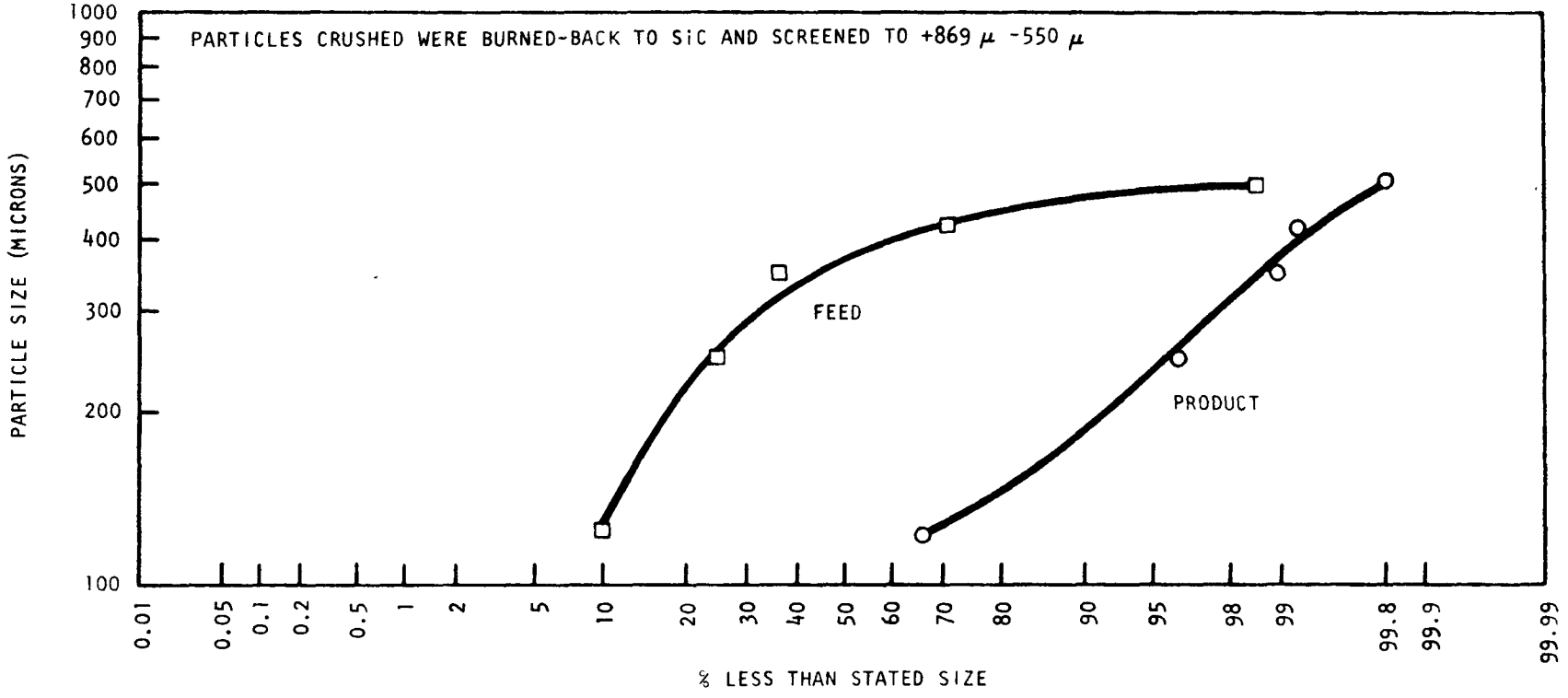

Fig. 5-13. Size distribution of feed and product, run F4RHB-M24

gas flow rate to let them settle from the filter chamber to the heated zone.

When combustion was complete, as indicated by the off-gas analysis, the bed was fluidized with 50 liters/minute of N_2. The product valve was then opened to empty the burner. After 1 minute, ~80% of the bed had been removed (according to the ΔP cell readout). Following 2 minutes of dumping, ~98% of the material was removed from the burner (determined by shutting down and dismantling the burner).

It is assumed that a commercial reprocessing plant would be operated on a batch basis of perhaps five or more secondary burner runs per batch. In this case, a short (2 to 5 minutes) bed removal between runs would be convenient, with a more complete cleanout (30 to 40 minutes) between batches. Data on short and long cleanouts will be taken on all future runs.

The thorium in the product was largely in the form of granulated "chunks" in the size range 30 to 150 μ. This is very different from the fluffy 5 to 10 μ agglomerate in the product of previous burning runs. The cause is almost certainly the different-gap particle crushers with the resulting different burner feed material.

Leaching

Experimental Leaching Runs

ThO_2 sol-gel particles were processed in the pilot plant leaching system (leaching runs 58, 59, 62, and 67 through 71) to establish operating characteristics with this type of material. It was established that essentially 100% thorium recovery could be obtained in less than 2 hours on sol-gel ThO_2 that had been crushed in a double-roll crusher. The uncrushed ThO_2 sol-gel required 16 hours for complete dissolution. The quantity of sparge air used for agitation of the leacher contents was also found to affect the dissolution rate. Results are depicted graphically in Fig. 5-14.

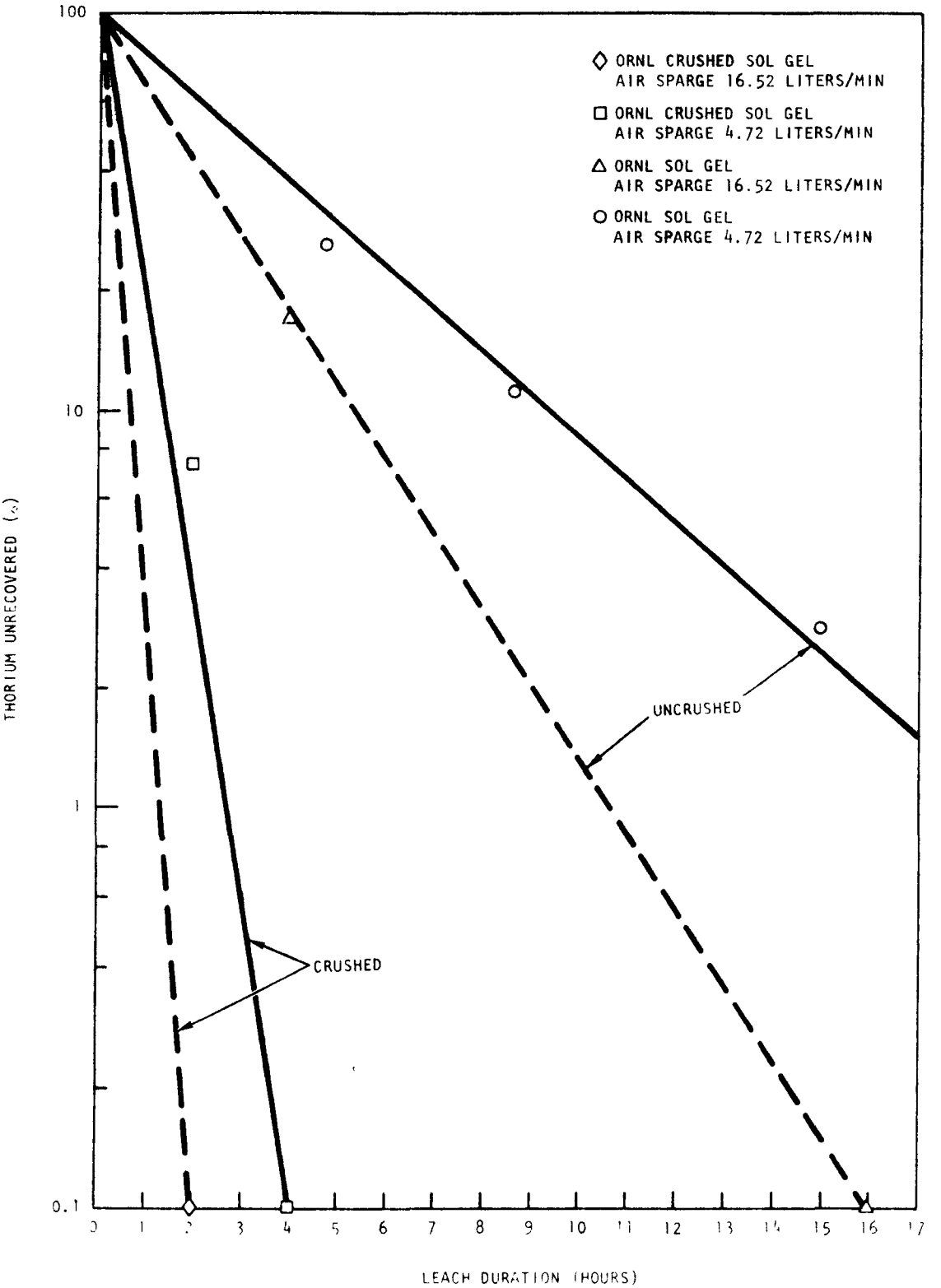

Fig. 5-14. ORNL sol gel dissolution, runs 58, 59, 62, and 67 through 71

This and other results are discussed in more detail under "Conclusions and Recommendations."

Summary of Leach Runs

Eight test runs were conducted with the 13-cm-diameter leacher. All of the tests were made on a batch basis using ThO_2 sol-gel material. The ThO_2 was initially in the form of BISO coated particles and was obtained from ORNL. The BISO coats were removed by fluidized-bed combustion prior to testing in the leaching system. All tests were conducted with about 3.8 liters of Thorex [13M HMO_3/0.05M HF/0.1M $Al(NO_3)_3$] per kg of ThO_2 feed. Operating data are shown in Table 5-3.

Runs 58, 59, 62, 67, and 68 were made using uncrushed feed, and runs 69 through 71 were made using double-roll crushed feed. Size distribution data are given in Fig. 5-15.

The steam-jet ejector system was not used for transfer of liquids because of an inadequate steam system (see earlier Quarterly Progress Report, Gulf-GA-A12599). All liquid transfers were accomplished with a peristaltic pump.

The liquid-solid separation of the leacher product was accomplished with a batch basket centrifuge. Centrifuge data for all runs are as follows:

1. 30-cm-diameter perforate basket.
2. Polypropylene filter bag (5 to 6 micron openings).
3. 1100 gravities purging force at basket sheet (2500 rpm).
4. After washing filter cake, spin dry for about 5 minutes.

The quantity and specific gravity of liquids in all storage tanks and the leacher were continuously and automatically monitored and recorded. Tank calibration relationships are included in Table 5-4. Analyses of samples

TABLE 5-3
LEACHER OPERATING DATA, 13-CM-DIAMETER LEACHER

	Leach Run Number							
	58	59	62	67	68	69	70	71
Burner ash charged, kg	2.00	2.00	2.00	2.00	2.00	2.00	2.00	2.00
Thorex charged, liters	7.68	7.63	7.60	7.60	7.93	7.61	7.68	7.57
Air sparge rate, liters/min	4.72	4.72	4.72	16.52	16.52	4.72	4.72	16.52
Leaching time at boiling point, hr	4.75	8.67	15.00	4.00	16.00	4.00	2.00	2.00
Insolubles after leach (dry wt), g	4.62	216.00	12.00	291.00	0	0	114.00	0
Mother liquor,[(a)] liters	8.74	9.19	8.44	8.34	9.16	7.52	8.46	8.211

[(a)] Includes some wash water.

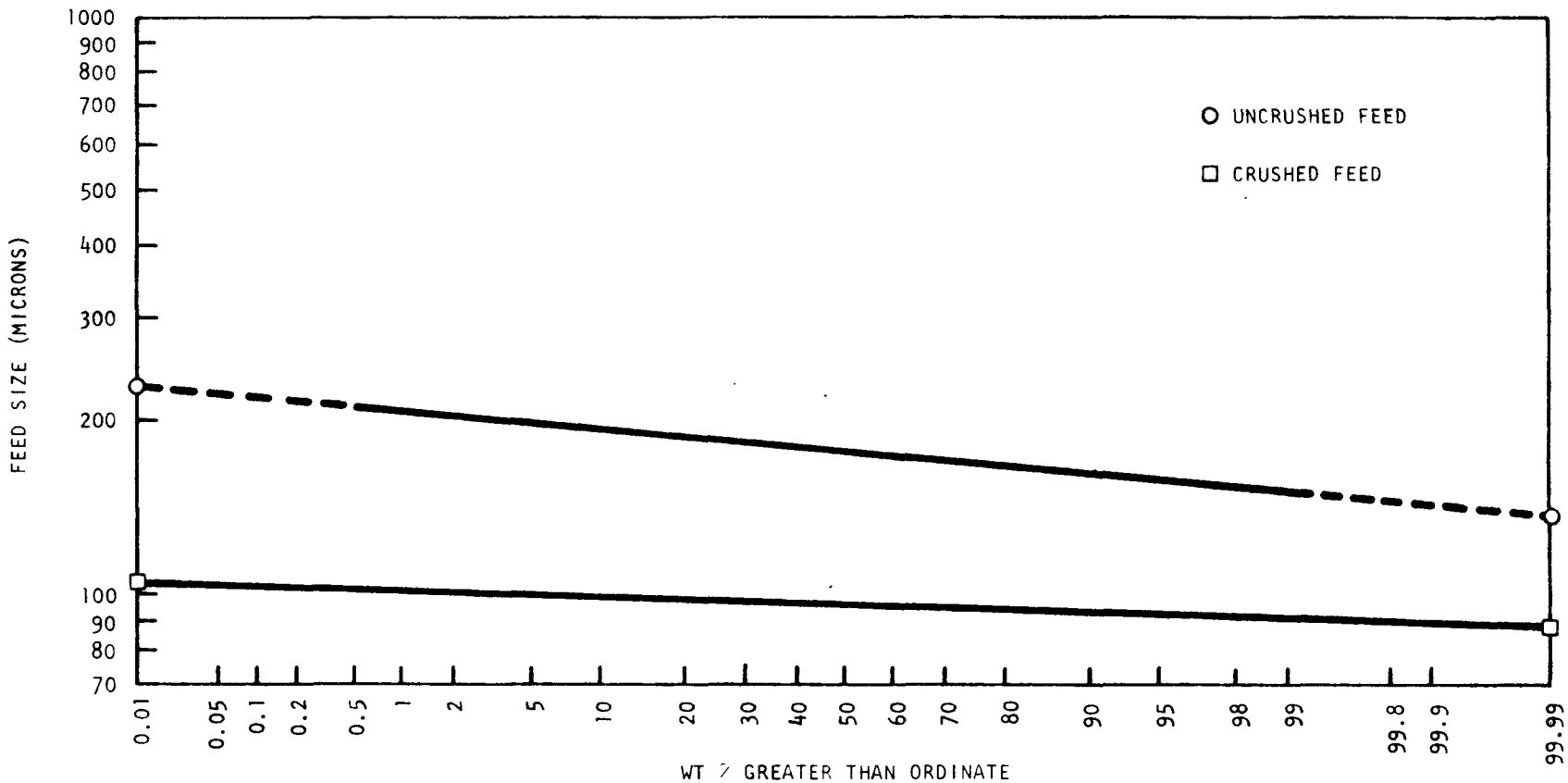

Fig. 5-15. Feed size distribution, runs 58, 59, 62, 67, 68, and 69 through 71

TABLE 5-4
WEIGHT FACTOR AND SPECIFIC GRAVITY
CALIBRATIONS FOR VESSELS[a]

Vessel	Weight Factor (kg)	Specific Gravity
Thorex	0.56084X - 0.25303	$\frac{0.2x}{10.406}$
20-cm leacher	0.48822X + 3.20925	$\frac{0.2x}{5.22}$
13-cm leacher	0.29282X + 1.80287	$\frac{0.2x}{5.174}$
Mother liquor tank	0.73555X + 0.55201	$\frac{0.2x}{10.15}$

[a]These calibrations were obtained with water using "least-squares" regression techniques, where

X is % reading on wt factor leg
x is % reading on specific gravity leg

} See Fig. 5-15, Quarterly Progress Report Gulf-GA-A12599

submitted to the Analytical Chemistry Department are given in Table 5-5. These data were utilized in material balance calculations (see Table 5-6).

Conclusions and Recommendations

The rate of dissolution for sol-gel ThO_2 is depicted graphically in Fig. 5-14. As expected, the rate of dissolution is substantially increased by reducing the average particle size of the solids fed to the leacher. An increase in the amount of sparge air used for agitation of the leacher contents was also found to increase the dissolution rate. The results of Fig. 5-14 can be represented mathematically:

Let Y = wt % thorium unrecovered
c = constant (function of sparge rate and average particle size)
θ = time in hours
e = irrational number, = 2.71828 ...., base of natural logarithms

The linear relationship depicted in Fig. 5-14 indicates:

$$Y = 100e^{c\theta}$$

where the value of c is estimated to be as shown in Table 5-7.

This mathematical relationship adequately describes the experimental results. Calculated results for different sparge rates and/or particle sizes (within the range investigated) can be made based on linear interpolation of the values of c given in Table 5-7.

The recorder readings between the Thorex tank and the 13-cm leacher show as much as 1.48 kg difference (see Table 5-8). From previous tests, the Thorex tank has been found to be accurate, indicating the error to be in the leacher calibration. Therefore, the leacher should be recalibrated. A comparison was also made between the mother liquor tank readings and the actual measured quantities (see Table 5-9). The mother liquor tank readings averaged 1.127 kg more than the amounts measured with a graduated cylinder. The specific gravity readings were low, indicating the need for recalibration. Run 62 was made using the measuring tank as the only receiving vessel. Calibrations were found in error (see Table 5-9).

TABLE 5-5
SAMPLE ANALYSIS RESULTS,[a] 13-CM-DIAMETER LEACHER

	Leach Run Number							
	58	59	62	67	68	69	70	71
Burner ash, wt % Th (i.e., ThO_2)	87.87	87.87	87.87	87.87	87.87	87.87	87.87	87.87
Insolubles, wt % Th (i.e., ThO_2)	87.87	87.87	87.87	87.87	87.87	87.87	87.87	87.87
Mother liquor,[b] g Th/liter	148.1	171.0[c]	202.3	175.6	192.6	238.7	192.6	214.0

[a] Mother liquor analysis is based on gravimetric determination by oxalate precipitation. Solids analysis is based on 100% ThO_2 composition.

[b] Includes some wash water.

[c] Because of an error in analytical results, this number was calculated based on a relationship between thorium content and the measured specific gravity of the solution.

TABLE 5-6
THORIUM MATERIAL BALANCE RESULTS, 13-CM-DIAMETER LEACHER

	Leach Run Number							
	58	59	62	67	68	69	70	71
Thorium input, g								
Burner ash[a]	1757.0	1757.0	1757.0	1757.0	1757.0	1757.0	1757.0	1757.0
Thorium output, g								
Mother liquor[b]	1294.0	1572.0	1706.0	1465.0	1763.0	1794.0	1628.0	1757.0
Insolubles	406.0	190.0	11.0	276.0	0	0	100.0	0
Total output	1700.0	1762.0	1717.0	1741.0	1763.0	1794.0	1728.0	1757.0
Material balance closure,[c] wt %	96.75	100.02	97.70	99.10	100.0	102.11	98.35	100.0
Thorium recovery,[d] wt %	73.65	89.0	97.10	83.0	100.0	102.11	92.66	100.0

[a] Based on solids which have a composition of 100% ThO_2.

[b] Includes some wash water.

[c] Output/input.

[d] Based on outlet quantities.

TABLE 5-7

ESTIMATED VALUE OF c

Particle Size	Estimated Value of c	
	Sparge Rate: 4.7 liters/min	Sparge Rate: 16.5 liters/min
Uncrushed (see Fig. 5-15)	-0.24	-0.44
Crushed (see Fig. 5-15)	-1.74	-3.52

TABLE 5-8
COMPARISON BETWEEN STORAGE TANKS USING CALIBRATION RELATIONS FROM TABLE 5-4
13-CM-DIAMETER LEACHER, THOREX TANK

	Leach Run Number							
	58	59	62	67	68	69	70	71
Thorex tank								
Thorex transferred to leacher, kg	10.81	11.63	10.79	10.50	10.94	10.50	10.60	10.50
Specific gravity	1.38	1.38	1.38	1.39	1.39	1.39	1.39	1.39
Leacher								
Thorex transferred from storage tank, kg	10.32	10.15	10.50	10.00	10.32	8.98	10.24	9.80
Specific gravity	1.40	1.42	1.39	1.43	1.39	1.40	1.40	1.40
Percent variation in leacher readings from Thorex tank								
Quantity	-0.49	-1.48	-0.29	-0.50	-0.55	-1.52	-0.36	-0.70
Specific gravity	+0.02	+0.04	+0.01	+0.04	0	+0.01	+0.01	+0.01

TABLE 5-9
COMPARISON BETWEEN STORAGE TANKS USING CALIBRATION RELATIONS FROM TABLE 5-4
13-CM-DIAMETER LEACHER, MOTHER LIQUOR TANK

	Leach Run Number							
	58	59	62	67	68	69	70	71
Mother liquor tank								
Leachate transferred to mother liquor tank, kg	14.23	14.82	13.07[a]	13.72	15.19	14.53	13.94	13.79
Specific gravity	1.503	1.510	1.600	1.490	1.498	1.462	1.509	1.488
Measured quantities								
Using 2-liter graduate and weighting, kg	13.12	13.90	13.23	12.84	14.05	11.92	13.13	12.91
Specific gravity using hydrometer	1.502	1.512	1.568	1.539	1.535	1.586	1.553	1.572
Percent variation in measured quantities from mother liquor tank readings								
Quantity	+1.10	+0.92	-0.160	+0.880	+1.140	+2.610	+0.810	+0.88
Specific gravity	+0.001	-0.020	+0.032	-0.050	-0.037	-0.124	-0.044	-0.084

[a]Measuring tank.

It was found that mother liquor tank ΔP readings were affected by thorium nitrate crystals building up in the dip legs. Some type of automatic rinsing system may be needed to cure this problem.

Insolubles were clinging to the walls and to the ball valve of the leacher after it was emptied. A distilled water rinse was found to remove these clinging particles. To provide accurate material balance information, a rinse system will be installed which will clean the leacher during the emptying operation.

TASK VIII

PHYSICS AND FUEL MANAGEMENT

REACTOR PHYSICS: ENDF/B PARTICIPATION

A literature survey was made and a short report was written on the energy release per fission in reactors by various isotopes. The following energy ratios per fission are recommended: U-233/U-235 = 0.988, Pu-239/U-235 = 1.031, and Pu-241/U-235 = 1.039 for thermal reactors and Th-232/U-238 = 0.954 for fast reactors. The energy release from U-238 fission can be assumed to be equal to that from U-235 fission, namely 192.5 MeV; similarly, the energy release from Pu-240 is essentially equal to that from Pu-239.

All of the ENDF/B Version III cross-section data sets needed for CSEWG thermal reactor benchmark calculations with current Gulf General Atomic methods were prepared except for a revised water scattering kernel. A new water scattering kernal based on the late 1969 revision of the ENDF/B scattering law data is being prepared with the Gulf General Atomic version of the FLANGE code.

A draft of a report documenting the GANDY3 unresolved resonance cross-section calculation code was completed.

Re-analysis of Control Rod Experiments Performed at the HTGR Critical Facility

Introduction/Summary

In 1968, an analysis (Ref. 8-1) of the control rod experiments performed as part of the HTGR critical program (Refs. 8-2, 8-3) revealed a substantial discrepancy between the calculated control rod worths and those inferred from the experiments. More precisely, the use of standard design techniques appeared to overestimate the worth of a single rod by ∿5% and the worth of a rod pair by ∿10%. Since this discrepancy must be factored into the design of the HTGR control system, there is a clear economic incentive to remove it, or at least understand it.

With this motivation, a study was performed to determine if the use of current design methods for cross-section generation (MICROX) and a more detailed treatment of the geometry (BUGTRI rather than GAZE) would reduce the observed disagreement. After a rather elaborate series of calculations, results essentially identical to those noted above were obtained.

The single-rod results are as accurate as can be expected with the quoted experimental uncertainties. However, the rod-pair results are not. The most likely source of error in this calculation appears to reside in the treatment of rod shadowing, and this can be eliminated by the use of TRIPLET, a triangular mesh transport theory code. It is recommended that this calculation be performed when TRIPLET becomes operational on the UNIVAC-1108. Apart from this, the most promising areas for any future effort appear to be (1) the re-evaluation of impurity levels in the central region, and (2) a review of the experimental corrections applied to the measured excess reactivity.

There was also some question about the validity of the high energy boron data used in this study. Accordingly, the single control rod

experiment was re-analyzed using ENDF/B Version III boron data instead of the standard Gulf General Atomic boron data. A small improvement in the comparison between calculation and experiment was obtained. The effect of using the ENDF/B Version III data does not appear to be large enough to explain the rod-pair worth discrepancy.

Description of the Experimental Facility

The details of the experimental configurations are given in Refs. 8-1 through 8-3. Only a general description of the facility and the experimental technique is presented in this section.

There are three configurations of interest in this study. Each is a three-region core with an approximately cylindrical shape contained within a rectangular aluminum honeycomb. The central or lattice region is composed of C, Th, and U-235; the middle or driver region contains C and U-235 in the ratio of 2500:1; and the outer or reflector region is composed of C and Al. Material densities are given in Ref. 8-1.

The base or unrodded core is designated as Core A. The second assembly, Core B, was constructed by removing the central element of Core A, replacing it with a control rod element, and building out the driver and reflector regions until the assembly became critical. (The control rod element consisted of an annular B_4C rod enclosed within a graphite sleeve with the same external dimensions as a fuel element.) Core E was constructed in a manner similar to Core B with two off-center rods replacing the central rod. Table 8-1 contains the equivalent radius of each region in each assembly.

In order to facilitate a "clean" analysis of the experiments, the measured excess reactivity was corrected to account for the reactivity associated with control system voids and the external honeycomb. Table 8-2 contains the measured and corrected excess reactivity for each assembly and the associated system eigenvalue based upon a β_{eff} of 0.0069.

TABLE 8-1

RADIAL DIMENSION OF CORE AND REFLECTOR WITH LARGE CONTROL RODS[a]

(in centimeters)

	Core A	Core B	Core C	Core D	Core E
HTGR lattice region	28.84	28.84	28.84	28.84	28.84
Heterogeneous or driver region	69.82	77.43	77.43	84.53	84.53
Reflector region	80.76	88.57	88.57	90.80	92.49

[a]From Ref. 8-1.

TABLE 8-2

MEASURED CORE REACTIVITY[a]

(in dollars)

	Core A	Core B	Core C	Core D	Core E
Measured core reactivity	0.41	0.42	0.50	0.21	0.33
Corrected core reactivity[a]	2.08	2.05	2.13	1.78	2.00
Corrected effective multiplication factor[b]	1.014	1.014	1.014	1.012	1.014

[a]To facilitate comparisons with calculations, it is desirable to make experimental corrections to the actual core reactivity for the addition of fuel or graphite elements in the locations taken up by control rods, safety rods, nuclear fuses, and ion chambers (Ref. 8-2).

[b]The calculated value of β_{eff} was used.

Calculational Procedure and Results

The fact that there were no direct measurements of control rod worth makes it necessary to adopt an indirect approach in comparing calculation and experiment. From Table 8-2, it is apparent that each configuration has the same eigenvalue. Our general approach, then, is to calculate the eigenvalue of each assembly and attempt to interpret any scatter in our results in terms of an error in control rod worth. More specifically, the three steps of the procedure are

1. Calculate the eigenvalue, k_A, of the unrodded core. Since this is presumably the easiest calculation, k_A is taken as the target for the remaining calculations.

2. Calculate the eigenvalue of assembly B both with and without the control rods present. If these eigenvalues are designated k_B and k_B^*, respectively, then the "experimental" control rod worth is $(k_B^* - k_A)/k_B^*$ kA and the calculated worth is $(k_B^* - k_B)/k_B^* k_B$, so that the error in the calculation is $[k_B^*(k_A - k_B)]/[k_A(k_B^* - k_B)]$.

3. Calculate the eigenvalue of assembly E both with and without control rods present. If these eigenvalues are designated k_E and k_E^*, then the formulae of Step 2 apply with the subscript E replacing B.

The individual calculations associated with each step of this process are described in the following paragraphs. The section Additional Calculations and Comments describes come subsidiary calculations performed to test the validity of the models used.

Cross-Section Generation. Cross sections were generated by performing separate MICROX (Ref. 8-4) calculations for the lattice and the driver regions. Control rod cross sections were averaged over the lattice region spectrum and reflector cross sections over the driver region spectrum.

The 14 energy group structure shown in Table 8-3 was chosen, rather than the standard 9 group structure, in order to properly model the fast leakage spectrum in this small core. Spatial effects were approximated by including an energy-dependent buckling term in this infinite medium calculation.

TABLE 8-3

ENERGY GROUP STRUCTURES

Lower Energy (eV)	Group No. (14 Groups)	Group No. (10 Groups)
3.329 E+6	1	1
1.353 E+6	2	1
4.979 E+5	3	1
1.831 E+5	4	1
3.183 E+4	5	2
4.307 E+3	6	2
9.61 E+2	7	3
1.761 E+1	8	4
3.930 E+0	9	5
2.381 E+0	10	6
4.140 E-1	11	7
1.000 E-1	12	8
4.000 E-2	13	9
0.0	14	10

Transport Theory. Several one-dimensional, P1-S4 transport theory calculations were made with the 1DFX (Ref. 8-5) code to determine:

1. The worth of a single rod.

2. Current-to-flux ratios at the rod surface for use in two-dimensional diffusion theory.

3. Region spectra for condensing the 14 group cross sections down to 10 groups, the existing upper limit in the triangular mesh diffusion theory codes available.

In all the 1DFX models the mesh spacing varied from ∿2 cm in the driver region to ∿0.05 cm in and around the control rod region. Some negative fluxes did appear in the lower two groups, but they did not significantly influence the results. Geometric axial bucklings were employed to simulate axial leakage, and all calculations were converged to 10^{-6} $\Delta k/k$.

The eigenvalue of the unrodded core, k_A, was calculated to be 1.0273. This is 0.0133 larger than the measured value and may well be a clue to the reason for the difficulty in calculating the worth of these rods. This is discussed further in the section, "Summary and Recommendations." For the lack of a reasonable alternative, this value of 1.0273 was taken as a target for the remaining assemblies.

Next Core B was analyzed. With the rod inserted, the eigenvalue, k_B, was 1.0233; with the rod removed, k_B^* was calculated as 1.0963. Thus, the "measured" worth is 0.0613 $\Delta k/k$, while the calculated worth is 0.0651, an overestimate of 5.8%.

Triangular Mesh Diffusion Theory. Although it was expected that a two-dimensional model would be required only for assembly E, a two-dimensional calculation was performed for assembly A to ensure that the target eigenvalue, k_A, was insensitive to the change in model and solution technique. The BUGTRI (Ref. 8-6) geometric model was designed to conserve both volume and mass with a mesh spacing (3.336 cm) that permitted an exact representation of the hexagonal fuel elements in the central region. Ten group cross sections were obtained by flux weighting reaction rates and current weighting transport cross sections over the 14 group spectra determined in 1DFX. The group boundaries are shown in Table 8-3.

The BUGTRI eigenvalue for Core A was 0.994 as compared to the 1DFX value of 1.0273. This discrepancy of 0.0333 is significantly larger than the diffusion/transport mismatch of ∿0.005 to 0.010 which has been observed in the past. An examination of the neutron balance tables showed that it was completely due to an overestimate of the system leakage. The reason for this overestimate is the difficulty encountered in correctly choosing an external boundary condition for the zig-zag system boundary. In the calculation, a value of $\delta = -(D/\phi)(\partial\phi/\partial n) = 0.4692$ had been used to simulate a vacuum boundary. Although this is correct for a slab or a large cylinder, it is inappropriate for a jagged boundary because, physically, re-entrant neutrons from adjacent zigs will act to reduce the normal derivative at the surface of neighboring zags. To overcome this difficulty, the external boundary condition was treated as a free parameter and adjusted until the leakage agreed with the 1DFX results. With this reduced boundary condition ($\delta = 0.14$ instead of 0.4692), the eigenvalue was 1.027 and the flux distribution agreed with the 1DFX distribution to ∿1%.

Next, Core B was analyzed in two stages. First, the appropriate external boundary condition was determined by a procedure, identical to that outlined above, which forced agreement with the rod removed. Then, the current-to-flux ratios at the surface of the graphite sleeve were taken from the 1DFX calculation, adjusted by the perimeter ratio of the two rod models to preserve the line integral, and used in a second BUGTRI calculation. This calculation overestimated the absorptions in the rod by ∿3%, an amount similar to that encountered in standard HTGR design calculations. The reason for this error, while not completely understood, is presumably due either to the coarseness of the mesh or the anisotropy of the 1DFX flux. Adjusting the current-to-flux ratios slightly to preserve rod absorptions yielded an eigenvalue, k_B, of 1.024 as compared with the unrodded eigenvalue, k_B^*, of 1.0952. This rod worth of 0.0635 overestimates the "experimental" value by 4.5%. If the external boundary condition of the unrodded core had been adjusted until k_B^* was exactly

the 1DFX value of 1.0963, this overestimate would have been reduced to 3.3%. The value of this pair of calculations is not the reduced discrepancy between calculation and experiment, but rather the confidence it gives us about treating the external boundary condition in this cavalier manner.

Next assembly E was analyzed by a similar procedure. The model has approximately the same external shape as that of core A so that one would expect the same boundary condition to apply. A BUGTRI/1DFX comparison for the unrodded core indicated this to be nearly true since the BUGTRI eigenvalue of 1.1249 was only 0.0017 lower than the 1DFX value. The adjusted rod current-to-flux ratios were then taken from the single rod case and a second calculation performed to obtain a rodded eigenvalue of 1.0113. Adjusting these values for the small bias noted above yields $k_E = 1.013$ and $k_E^* = 1.1266$ which, with k_A equal to 1.0273, implies an "experimental" worth of 0.0858 and a calculated worth of 0.0995. Thus, the calculation is in error by $\sim$13.8%.

Additional Calculations and Comments

In an attempt to reduce the discrepancies listed above, subsidiary calculations were performed to verify some of the assumptions made in the models used. The results, and some qualitative comments, are contained in the following paragraphs.

Cross Sections. Ignoring the possibility of mistakes in the basic data (fine group cross-section sets and material densities), errors can be introduced by the use of either inappropriate bucklings or an inadequate group structure. The first possibility was eliminated by simply performing a buckling iteration and noting an insiginficant change in system eigenvalue. The adequacy of the group structure was not checked directly, i.e., by the straightforward process of increasing the number of groups until the solution remained constant. There were two reasons for this, as follows:

1. The similarity of the single rod worths calculated in this and the previous study (which used 10 groups) implies that $\Delta k/k$ is not sensitive to the group structure used.

2. An earlier sensitivity study (Ref. 8-7) had shown that this structure is completely adequate for HTGR control rod calculations.

Thus, while the eigenvalue itself may be sensitive to the number of energy groups (similar HTGR critical analyses indicated a change of 0.004 Δk in going from 12 to 30 groups), control rod worths should not be.

Transport Theory. To test the adequacy of the P1-S4 approximation, a P1-S8 calculation was performed for the rodded core. The change was negligible.

BUGTRI. Since BUGTRI assumes a constant mesh spacing throughout the core, it was not possible to increase the resolution of the flux around the control rods without greatly increasing the cost of the calculation. Therefore, it is difficult to evaluate whether or not the relatively coarse mesh spacing of 3.336 cm did allow an adequate representation of the flux gradient. However, the good agreement of the BUGTRI and 1DFX calculations for the single rod core implies that the truncation error is not very significant.

The treatment of the external boundary condition as a free parameter is, of course, subject to question. Qualitatively the adjustment is reasonable, but the magnitude of the change is difficult to defend on purely theoretical grounds. It is reassuring, however, to note that when the boundary condition is adjusted to force the system leakage to agree with an equivalent 1DFX calculation, both the eigenvalue and the flux distribution also agree very closely.

The 1DFX current-to-flux ratios were taken at the outer surface of the graphite sleeve and then reduced by 5% so that the line integral over the hexagonal model would equal that calculated in the 1DFX cylindrical approximation. This process assumes that BUGTRI and 1DFX will calculate identical average fluxes along the surface. The good agreement between the calculations tends to justify this assumption.

The use of rod surface current-to-flux ratios from a single-rod calculation in a rod-pair calculation tacitly assumes that the incident flux spectrum does not vary between the two cases. This assumption is clearly violated on the facing sides of the rod pair since the shadowing will induce some spectral hardening. Ignoring this spectral hardening will overestimate the worth of a rod-pair. This is true because, as the incident spectrum hardens, the fast flux within the graphite sleeve increases. This increases the scattering source to the lower groups and thus the flux and outflow in these groups per unit surface flux. By ignoring this behavior, the rod current-to-flux ratio is overestimated and, thus, the rod worth.

The most straightforward way to eliminate this error is to use a transport theory code that can calculate shadowing directly. TRIPLET (Ref. 8-8), a triangular mesh transport theory code currently being converted to our computer, is the obvious candidate for such a calculation.

Summary and Recommendations

The results described above indicate a discrepancy between calculation and experiment of $\sim$5% for the worth of a single rod and $\sim$10% for that of a rod pair. The single-rod error is not inconsistent with the quoted experimental error of ±0.003 for each assembly. However, the rod-apir error is statistically significant. In searching for the reason for this error, it is important to note that these results are essentially identical to those obtained in the original analysis, even though the

methods used in that study were quite different from those used here. This is especially true of the spatial modelling of the rod-pair configuration. This consistency implies that the reason for this discrepancy is common to both studies and suggests that the error is contained in either the basic nuclear data, material densities assumed, or the interpretation of the experimental data available.

In considering the first two areas, the fact that an analysis of a core fueled completely with driver fuel (C/U = 2500 in Ref. 8-2) showed good agreement with experiment suggests that the error is associated with the lattice region. This is also consistent with the observation that, as the importance of the lattice region is reduced by the insertion of control rods, the calculated eigenvalue agrees more closely with the measured eigenvalue of 1.014. Since the lattice region had a relatively high impurity level, an examination of the sensitivity of the control rod worths to the levels assumed might well be useful.

There is also some question about the validity of the boron data set used in both these studies. More recent data sets show reduced absorption and scattering cross sections at high energies (Ref. 8-9), a change which would improve the agreement of the rod worth calculations. The single control rod experiment was reanalyzed using ENDF/B Version III boron data. Only a small improvement in the comparison between calculation and experiment was obtained.

The third area of investigation is the re-examination of the experimental corrections made to the measured excess reactivity to account for the reactivity tied up in control system voids, offset to some extent by the reflective properties of the honeycomb. There are two points which perhaps warrant some further scrutiny. First of all, how often were these corrections measured? If, for example, the honeycomb worth had not been re-evaluated for each configuration, the calculational trend would become more understandable. The second point is concerned with the possible flux distortion introduced into our calculations by

not treating the presence of local disturbances explicitly. Some triangular mesh calculations would indicate the degree of calculational sensitivity to this approximation.

In summary, the most probable reasons for the observed discrepancy and the indicated method of resolution are:

1. The treatment of rod shadowing - perform a TRIPLET calculation.

2. Impurity levels assumed - perform a sensitivity study.

3. Experimental data - review experimental log (if available) and study sensitivity to local disturbances.

Analysis of HTLTR Critical Experiments

Regression analyses of the experimental k_∞ data generated during the HTLTR program were completed. Confidence limits for both $k_\infty(T)$ and $dk_\infty(T)/dT$ were established. The best (narrowest) confidence limits were obtained for the lattices where the agreement between calculation and experiment is best. The rather wide confidence limits obtained for HTGR Lattices No. 1 and 3 indicate that good agreement between experiment and calculation for these lattices would be quite fortuitous.

HTLTR Reactivation

One critical experiment in a Pu-fueled HTGR lattice was performed in the original HTLTR program. Further experiments, however, will probably be required before commercial use of Pu fuel can be warranted. Discussions between GGA and BNWL personnel were held regarding the experimental scope, duration, and priorities associated with reactivating the HTLTR for a Pu-fueled HTGR lattice program. These discussions revealed that a meaningful program would cost about $400,000 per year for a period of 3 years.

A recommendation against reactivation of the HTLTR in the near future was transmitted to the AEC.

Topical Report Summarizing GGA Analysis of the HTGR and HTLTR Critical Experiments

Work on a topical report summarizing all relevant GGA analyses of the HTGR and HTLTR critical experiments continued.

REACTOR PHYSICS: ANALYSIS OF REACTOR NOISE AND PULSED-NEUTRON EXPERIMENTS IN LARGE HTGRs

Work on a topical report assessing the potential usefulness of reactor noise analysis techniques for large HTGRs continued.

TEST ELEMENT PROGRAM

Fuel Test Element FTE-3

Anneal and Hydrolysis Tests on FTE-3 Fuel Rods

Fuel rods irradiated in FTE-3 were annealed at temperatures of 1600°, 1800°, and 2000°C to produce failed particles. The rods selected for this work contained TRISO coated UC_2 particles and BISO coated ThC_2 particles. The purpose of this work is to determine (1) time-temperature failure rates, and (2) the effect of hydrolysis on fission gas release (R/B) from exposed carbide fuel. The anneals and fission gas release tests were performed in the TRIGA King furnace facility.

As reported in the previous Quarterly Progress Report (Gulf-GA-A12725), the rod that was annealed at 1600°C showed approximately 4% particle failure after 520 hr of annealing in dry helium. Exposure of this rod at 900°C to 10^{-4} atm water (equivalent to 2 ppmv water in the primary coolant at 50 atm) caused only a factor of 1.5 increase in the R/B value. Further exposure of the rod to 0.03 atm water (equivalent to 600 ppmv water in the primary coolant) caused a further increase (by a factor of 3) in the R/B value. On subsequent annealing of the rod at 1100°C in dry helium, the R/B value decreased by a factor of 2. Thus, the overall increase was less than a factor of 3.

Table 8-4 shows the results for rods annealed at 1800° and 2000°C. The rod annealed at 1800°C showed a high R/B value (1.1×10^{-2}) after a total anneal time of 135 hr. An attempt to remove the rod intact from the standard fission gas release crucible failed. The rod was reduced to several smaller pieces during the anneal. One of these pieces has been submitted for metallographic examination. The rod annealed at 2000°C showed ∿5.6% fuel particle failure after annealing for 79 hr. This rod is currently being hydrolyzed at 1000°C in the King furance facility using helium gas containing 100 ppmv water. Fission gas release values will be determined periodically during the hydrolysis.

TABLE 8-4
EFFECT OF ANNEALING ON FISSION GAS RELEASE (R/B) FOR FUEL RODS IRRADIATED IN FTE-3

Rod No.	Anneal Temp (°C)	Anneal Time (hr)	Kr-85m R/B at 1100°C
1-7-6	--	0	4.6×10^{-6} [a]
	1800	10	2.7×10^{-6}
	1800	30	2.2×10^{-5}
	1800	53.5	1.7×10^{-5}
	1800	83.5	2.5×10^{-5}
	1800	135.5	1.1×10^{-2}
1-7-7	--	0	1.9×10^{-5} [a]
	2000	1	1.9×10^{-5}
	2000	4	5.6×10^{-5}
	2000	9	4.4×10^{-5}
	2000	19	3.2×10^{-5}
	2000	29	6.2×10^{-5}
	2000	59	8.8×10^{-5}
	2000	79	3.0×10^{-4}

[a] R/B for irradiated rod as-received.

The anneal and hydrolysis tests on FTE-3 fuel rods will henceforth be performed and reported under Task IV.

Metallic Fission Product Release Studies

Metallic fission product release experiments are being performed on samples of loose BISO coated fuel particles irradiated in FTE-3. The purpose of this work is to determine diffusion coefficients for metals (such as cesium, strontium, and cerium) in coating and kernel materials. The diffusion coefficients are determined from fractional release versus time curves. Metallic fission products such as cesium are monitored by collecting them on a cold finger located near the crucible containing the particles. The fission products are leached from the cold finger after removal from the annealing furnace and gamma-counted to determine the amounts released. Fractional release values are then obtained by comparison with the initial particle fission product content prior to annealing.

The fission product metal release studies on FTE-3 particles will henceforth be performed and reported under Task IV.

Fission Product Release Samples

Four niobium-canned fission product release samples (No. Nb-3, Nb-6, Nb-10, and Nb-14) were irradiated in the spine of FTE-3. The design of the fission product release samples is shown in Fig. 8-1. Each sample consists of fuel particles loaded into an H-327 graphite crucible along with coke material to absorb fission products. Each crucible is wrapped with graphoil and perforated niobium foil and placed in a thick-walled niobium can. The purpose of the niobium can is to retain the fission products released during irradiation. The coated particles irradiated in the four samples are described in Table 8-5.

A thermal analysis of the fission product release samples was performed to determine the maximum probable fuel particle bed temperature. Temperature data are shown in Table 8-6, where a maximum fuel particle bed temperature of 1371°C is indicated. The increase in temperature from the 1100°C spine temperature consists of a 90°C rise across the helium gap, an 80°C rise across the foil-filled gap between the niobium and graphite crucibles, and a 100°C rise from the graphite crucible into the fuel particle bed. On the basis of this analysis, the fuel bed temperature is taken to be 1360°C.

The TAC2D computer code was used for the thermal analysis. The thermal model, which was based on drawings from Ref. 8-10, incorporated a fuel particle bed 0.025 in. deep. Equal spacing was assumed between the graphoil and niobium sheets that surround the inner graphite crucible on the sides and top. The spacing between foils located below the graphite crucible was taken as 0.0005 in. These spaces were filled with an unknown mixture of argon, nitrogen, and methane gas; however, for the present analysis, a gas with the thermal conductivity of nitrogen was assumed. The 0.1-in. nominal radial gap existing between the niobium crucible and the 1100°C outer body was assumed to be filled with helium.

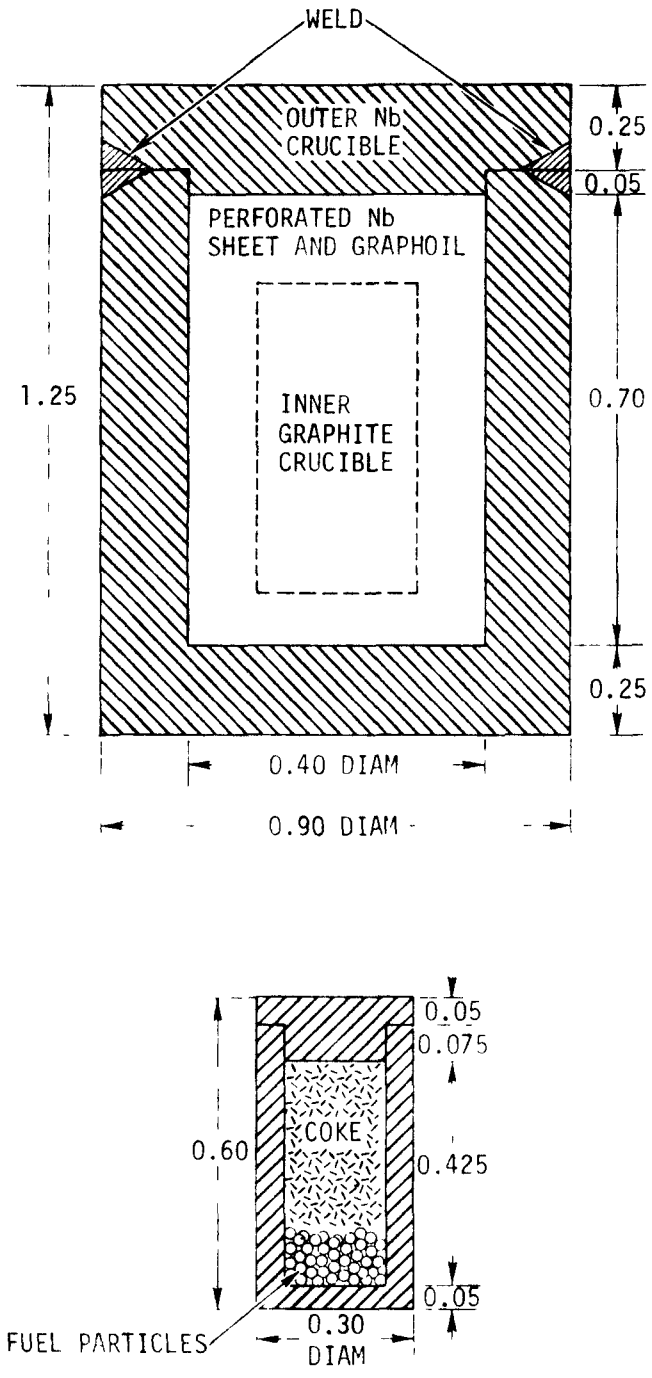

Fig. 8-1. Design of fission product release spine samples in FTE-3: top, outer crucible (niobium), and bottom, inner crucible

TABLE 8-5

DESCRIPTION OF FUEL PARTICLES USED IN NIOBIUM-CANNED FISSION PRODUCT RELEASE SAMPLES IRRADIATED IN FTE-3

Crucible No.	Particle Batch No.	Kernel Type	Kernel Size (μm)	Coating Type	Buffer		Outer Isotropic		Coating Gas	
					Thickness (μm)	Density (g/cm^3)	Thickness (μm)	Density (g/cm^3)	Buffer	Isotropic Coating
Nb-3	4000-227	$(ThU)C_2$[a]	193	BISO-LTI	40	1.20	72	1.85	Propylene	Propylene
Nb-6	4000-232	$(ThU)C_2$[a]	198	TRISO-LTI[b]	51	1.06	38	1.78	Acetylene	Propylene
Nb-10	4632-137	$(ThU)C_2$[a]	200	BISO-LTI (Si doped)	46	1.22	72	2.18	Propylene	Propylene
Nb-14	4503-59	UO_2	232	BISO-LTI	50	1.30	70	1.83	Propylene	Propylene

[a] Th/U = 2

[b] Inner isotropic coating thickness = 19 μm, density = 1.86 g/cm^3; SiC coating thickness = 21 μm, density = 3.21 g/cm^3.

TABLE 8-6
THERMAL ANALYSIS OF NIOBIUM-CANNED FISSION PRODUCT RELEASE SAMPLES (No. Nb-3, Nb-6, Nb-10, and Nb-14) IRRADIATED IN FTE-3

Component	Temperature Range (°C)
Niobium crucible	1187 to 1194
Graphoil and niobium foils	1205 to 1219
Graphite crucible	1250 to 1274
Coke material	1252 to 1270
Fuel particles	1349 to 1371

The primary uncertainties in the analysis are (1) the composition (and thus the thermal conductivity) of the gas in the particle bed and in the space between crucibles, and (2) the spacing of the foils beneath the graphite crucible. Since the graphite crucible exerts a relatively small pressure on the foils beneath it, the gaps between foils may be larger than the 0.0005 in. assumed, but are probably not smaller than this value. Wider gaps would increase the fuel temperature.

In order to establish the probable temperature limits within which the fuel was likely to have operated, runs were made with argon gas (low thermal conductivity) and methane gas (high thermal conductivity) in the gap. Maximum fuel temperatures of 1395°C with the argon and 1326°C with the methane were obtained, in comparison with 1371°C obtained with nitrogen.

After irradiation in FTE-3, the four fission product release samples were separated into component parts and gamma-counted to determine the distribution of Cs-137, Ce-144, and Zr-95. The particles were separated from the coke material by screening. The distribution data are given in Table 8-7.

As shown in Table 8-7, the retention of Cs-137 in the Nb-3 BISO particles was relatively high (0.94 fraction) considering the high irradiation temperature (1360°C). The relatively low retention of Ce-144

TABLE 8-7

DISTRIBUTION OF Cs-137, Ce-144, AND Zr-95 IN FISSION PRODUCT RELEASE SAMPLES IRRADIATED IN FTE-3

Fuel Particle Sample	Nuclide	Distribution of Fission Product Nuclide[a]							
		Fuel Particles		Coke[b]		Graphite Crucible		Graphoil	
		(mg/g)	Fract.	(mg/g)	Fract.	(mg/g)	Fract.	(mg/g)	Fract.
Nb-3, BISO coated (Th, U)C_2	Cs-137	4.8(-1)[c]	0.94	2.9(-2)	0.057	4.2(-4)	0.001	1.7(-3)	0.003
	Ce-144	2.1(-1)	0.81	1.9(-2)	0.074	6.3(-3)	0.024	2.4(-2)	0.095
	Zr-95	1.4(-1)	0.95	4.9(-3)	0.034	2.7(-4)	0.002	1.3(-3)	0.009
Nb-6, TRISO coated (Th, U)C_2	Cs-137	4.0(-1)	0.97	1.1(-2)	0.028	7.6(-5)	<0.001	2.9(-4)	0.001
	Ce-144	2.2(-1)	0.93	7.4(-3)	0.032	9.0(-4)	0.004	7.7(-3)	0.033
	Zr-95	8.6(-2)	0.98	1.7(-3)	0.019	5.1(-5)	0.001	2.5(-4)	0.003
Nb-10, BISO (Si) coated (Th, U)C_2	Cs-137	3.6(-1)	0.84	5.9(-2)	0.14	1.5(-3)	0.003	1.0(-2)	0.03
	Ce-144	1.8(-1)	0.81	2.0(-2)	0.088	7.8(-3)	0.035	1.4(-2)	0.063
	Zr-95	9.6(-2)	0.80	(d)	(d)	1.0(-3)	0.008	(d)	(d)
Nb-14, BISO coated UO_2	Cs-137	3.2(-1)	0.33	5.9(-1)	0.61	7.5(-3)	0.008	5.7(-2)	0.06
	Ce-144	2.4(-1)	0.97	(e)	(e)	1.2(-3)	0.005	7.2(-3)	0.029
	Zr-95	1.2(-1)	0.99	(e)	(e)	1.0(-4)	0.001	5.2(-4)	0.004

[a] Fractions of nuclides associated with the niobium crucibles were <0.001.

[b] Petroleum coke.

[c] 4.8(-1) means 4.8×10^{-1}.

[d] Component samples being recounted.

[e] Below limits of detection.

(0.81 fraction) is consistent with experience on cerium retention. The presence of about 5% of the Zr-95 outside the Nb-3 particles suggests that about 5% of the particles failed and that the fuel kernels broke into fragments which became associated with other components. Zirconium is a non-volatile refractory metal, and would be expected to remain with the fuel at the irradiation temperature of 1360°C. The releases of Cs-137 and Zr-95 from the Nb-3 particles were similar (0.006 and 0.05, respectively), suggesting that the fractions of Cs-137 outside the fuel particles was more likely the result of broken particles than of release by diffusion.

As expected, the TRISO particles (sample Nb-6), in comparison with the BISO particles, were more effective in retaining the metal nuclides. Two percent of the Zr-95 was found outside the TRISO particles, suggesting that 2% of the particles failed and broke into fragments.

The data for sample Nb-10 indicate that silicon-doping of the BISO coating was not effective in retaining the metal nuclides. The Nb-14 particle sample showed the highest release of Cs-137, indicating that the particular combination of UO_2 kernel and BISO coating was not effective in retaining cesium. On the other hand, the Nb-14 particle sample showed high retention of Ce-144, indicating the effectiveness of oxide kernels in retaining cerium.

It is of interest to use the curve in Fig. 4-3 (see Task IV) to estimate the release of Cs-137 from BISO prrticles under the irradiation conditions of FTE-3. To do this, a value is calculated for Dt/ℓ^2, where D is the diffusion coefficient for cesium in pyrolytic carbon, t is the irradiation time, and ℓ is the coating thickness. On the basis of data from out-of-pile cesium release experiments under way at Gulf General Atomic, $D = 2 \times 10^{-11}$ cm^2/sec at 1360°C. The irradiation time t was 132 days for FTE-3, and from Table 8-4, ℓ = 70 μm. Using these values $Dt/\ell^2 = 4.7$. As shown by the curve in Fig. 4-3, this value corresponds to an accumulated release of 70%, or a retention of 30%.

The observed retention of each of the four particle samples was higher than 30% (see Table 8-7); thus, the degree of cesium retention was greater than that presently used in calculations of cesium release from an HTGR core.

Diffusion Samples

Eleven metallic diffusion samples were irradiated in FTE-3. The main purpose of the diffusion samples is to obtain diffusion coefficient data for fission product metals in graphite. As shown in Fig. 8-2, the diffusion samples consisted of H-327 graphite crucibles having an annular hole, which contained coke material impregnated with isotopes of cesium, strontium, barium, and samarium, or mixtures of these isotopes, in varying concentrations. The isotopes activate in the reactor or have long half-lives, permitting analysis after irradiation. The enriched isotopes are strontium (Sr-84) 82% enriched and samarium (Sm-152) 99% enriched. Cesium-133 (natural) is used in the samples containing this particular metal. For the samples containing barium, Ba-133 is used to tag the stable material. The isotopes are in the form of carbides in coke material. (See Ref. 8-10 for further detail on diffusion samples.)

After irradiation of the diffusion samples, the post graphite and wall graphite were sectioned on a lathe to determine fission product concentration profiles. The concentration profiles are being analyzed by Prof. L. R. Zumwalt, North Carolina State University, to determine diffusion coefficient data. Two computer programs were developed for use in the analysis: (1) PLOTIT for plotting data, and (2) CPROFIT (Concentration PROfile FIT) for fitting and analyzing data on the basis of slow (transient) and fast (constant flux) components.

Sorption ratio values (partition coefficient or ϕ values) for cesium between the coke material and H-327 graphite were derived from Cs-134 loadings in the coke material and Cs-134 concentration profiles. Cesium loadings in the coke material were determined by chemical analysis of samples of the unirradiated coke material. Cs-134 concentration values in the graphite at

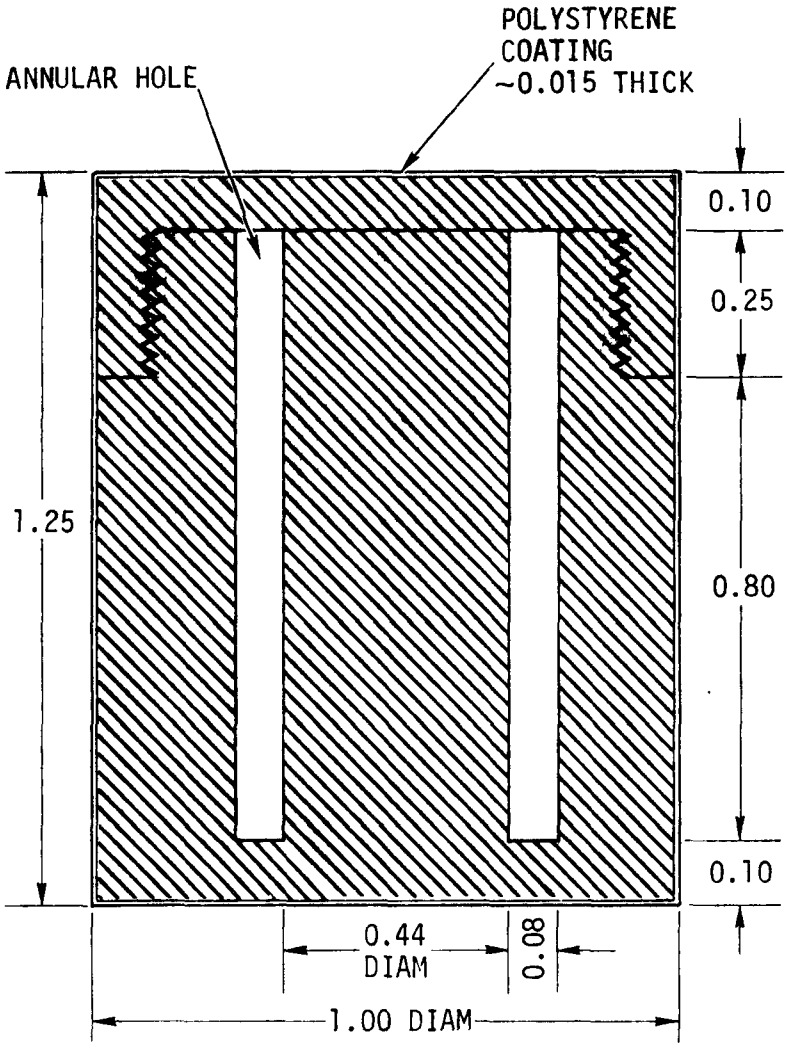

Fig. 8-2. Design of diffusion spine samples

the surface were obtained by extrapolating the concentration profiles to zero depth.

The cesium sorption ratio data are given in Table 8-8. Two values are given for each diffusion sample: one value was measured between the coke and the post graphite and the other value between the coke and the wall graphite. The sorption ratio values are appreciably higher for furfuryl alcohol coke than for petroleum coke. The coke in sample 55 contained 1% MgF to determine the effectiveness of the fluoride ion for gettering fission product metals; this had no apparent effect on the sorption ratio for cesium. The sorption ratio values appear to decrease with increasing temperature.

TABLE 8-8

CESIUM SORPTION RATIOS DERIVED FROM DATA FOR FTE-3 DIFFUSION SAMPLES

Sample	Irrad. Temp. (°C)	Thermal Flux (E<2.38 eV)	Fast Flux (E>0.18 MeV)	Coke			Sorption Ratio, ϕ[b]	
				Type[a]	Cs Loading (mg/g)	Cs-134 Loading (mg/g)	Inner[c]	Outer[d]
3	743	0.35(21)[e]	0.40(21)	Alc	3.2	9.5(-2)	360	320
5	982	0.35(21)	0.32(21)	Alc	3.2	9.3(-2)	130	210
42	840	0.46(21)	0.50(21)	Alc[f]	11.0	5.3(-1)	150	590[g]
45	968	0.33(21)	0.28(21)	Alc[f]	0.92	2.8(-2)	140	280
55	957	0.31(21)	0.25(21)	Alc[h]	26.8	4.0(-1)	90	200
63	963	0.32(21)	0.26(21)	Pet	0.51	1.2(-2)	10	20
66	1057	0.64(21)	0.60(21)	Pet	0.51	1.3(-2)	5	10

[a] Alc signifies furfuryl alcohol coke; Pet signifies petroleum coke.

[b] Units for ϕ are mg Cs/g coke — mg Cs/g H-327 graphite.

[c] Inner ϕ values measured at interface between coke and post graphite.

[d] Outer ϕ values measured at interface between coke and crucible wall.

[e] 0.35(21) means 0.35×10^{21}.

[f] Other metals (Sr, Sm, and Ba) present.

[g] This value is questionable.

[h] Other metals (Sr, Sm, and Ba) present. Coke contained 1% MgF.

REFERENCES

8-1. Nirschl, R. J., E. M. Gillette, and J. R. Brown, "Experimental and Analytical Results for HTGR Type Control Rods of Hafnium and Boron in the HTGR Critical Facility," USAEC Report Gulf-GA-A9354, Gulf General Atomic, January 31, 1973.

8-2. Bardes, R. G., et al., "Results of HTGR Critical Experiments Designed to Make Integral Checks on the Cross Sections in Use at Gulf General Atomic," USAEC Report GA-8468, Gulf General Atomic, February 12, 1962.

8-3. Pound, D. C., et al., "Hazards Report for Modified HTGR Critical Facility," General Dynamics, General Atomic Division Report GA-6452 (Rev. 2), 1966.

8-4. Walti, P. and P. Koch, "MICROX, A Two-Region Flux Spectrum Code for the Efficient Calculation of Group Cross Sections," Gulf General Atomic Report Gulf-GA-A10827, April 14, 1972.

8-5. Archibald, R., K. D. Lathrop, and D. Mathews, "1DFX - A Revised Version of the 1DF(DTF-IV) SN Transport Theory Code," Gulf General Atomic Report Gulf-GA-B10820, September 27, 1971.

8-6. Dorsey, J. P., R. Froehlich, and F. Todt, "BUG-2/BUGTRI, Two-Dimensional Multigroup Burnup Codes for Rectangular and Hexagonal Geometry," USAEC Report GA-8272, Gulf General Atomic, August 22, 1972.

8-7. Mangan, D. and V. Malakhof, "Methods for Calculating the Control Rod Worth in PSC," Gulf General Atomic unpublished data, 1966.

8-8. Reed, Wm. H., et al., "TRIPLET: A Two-Dimensional, Multigroup, Triangular Mesh, Planar Geometry, Explicit Transport Code," USAEC Report LA-5428-MS, Los Alamos Scientific Laboratory, 1973.

8-9. Mathews, D., Gulf General Atomic, personal communication.

8-10. Steward, K. P., "Spine Samples in the Phase 1 and Phase 2 Peach Bottom Test Elements," Gulf General Atomic unpublished data, September 30, 1971.

TASK IX

FUEL MATERIALS DEVELOPMENT

FUEL IRRADIATIONS

Capsule P13N

Capsule P13N is the fourth in a series of irradiation tests of candidate HTGR recyclable-type fuels and is the first P-capsule to be monitored for in-pile fission gas release during irradiation. The two primary objectives of this experiment were: (1) to compare oxide, carbide, and resin kernel irradiation performance at very high temperatures (1350° to 1500°C) to moderate fast fluences ($\sim 5.5 \times 10^{21}$ n/cm^2), and (2) to determine coated particle and fuel rod dimensional changes as a function of irradiation temperature, fluence, and particle design.

The capsule contained five cells in which fuel rods and unbonded particle samples were tested. A total of 22 fuel rods, 24 loose particle samples, and 175 piggyback samples were irradiated. Particle samples from parent coated particle batches were tested in fuel rods. Particle samples separated from the parent batches according to size and density were tested as unbonded particle samples. Descriptions of the fuel particles and fuel rod samples were given in an earlier Quarterly Progress Report (Gulf-GA-A12150).

Capsule P13N was inserted in the ETR (I-135W core position) in cycle 114E on January 19, 1972, and completed its scheduled irradiation on January 5, 1973 after 3732 effective full-power hours of operation. It was then shipped to the GGA Hot Cell, where it is currently undergoing post-irradiation examination.

Disassembly of the capsule and preliminary examination of all the fuel samples has been completed. The results of the examination of the fuel rod samples, which consisted of visual examination, metallography, and post-irradiation fission gas release measurements, were reported in the previous Quarterly Progress Report (Gulf-GA-A12725). Fuel rod dimensional change data and fuel rod disintegration - acid leach data are currently undergoing analysis and will be reported at a later date.

Fuel kernel migration coefficients were calculated for 28 UO_2 TRISO particles exhibiting unidirectional kernel migration in fuel rods 2D-16, 2A-10, 4D-9, and 5A-19. These data were presented in Fig. 9-20 of Quarterly Progress Report Gulf-GA-A12725. A systematic error was made in calculating the temperature gradients for these particles from the RAT code thermal analysis; consequently, the kernel migration coefficients reported for these particles are high by a factor of 5 to 10. The kernel migration coefficients were recalculated and are plotted in Fig. 9-1 as a function of reciprocal temperature.

Visual examination, metallography, and fission gas relase measurements were completed on the 24 unbonded particle samples. In some instances temperature effects observed in the unbonded particle samples appeared to be inconsistent with the particle performance in the bonded fuel rods tested in capsule P13N and with unbonded particle irradiations in previous P-capsule tests. Thermal analysis of the unbonded fuel beds is currently being re-evaluated; the results of the examination of the unbonded particle samples will be reported at a later date.

Capsule P13P

Capsule P13P, a companion test to P13N, is the fifth in a series of irradiation tests of candidate HTGR recyclable-type fuels. The capsule contained five cells in which fuel rods and unbonded particle samples were tested. Descriptions of the fuel particle and fuel rod samples were given in an earlier Quarterly Progress Report (Gulf-GA-A12222).

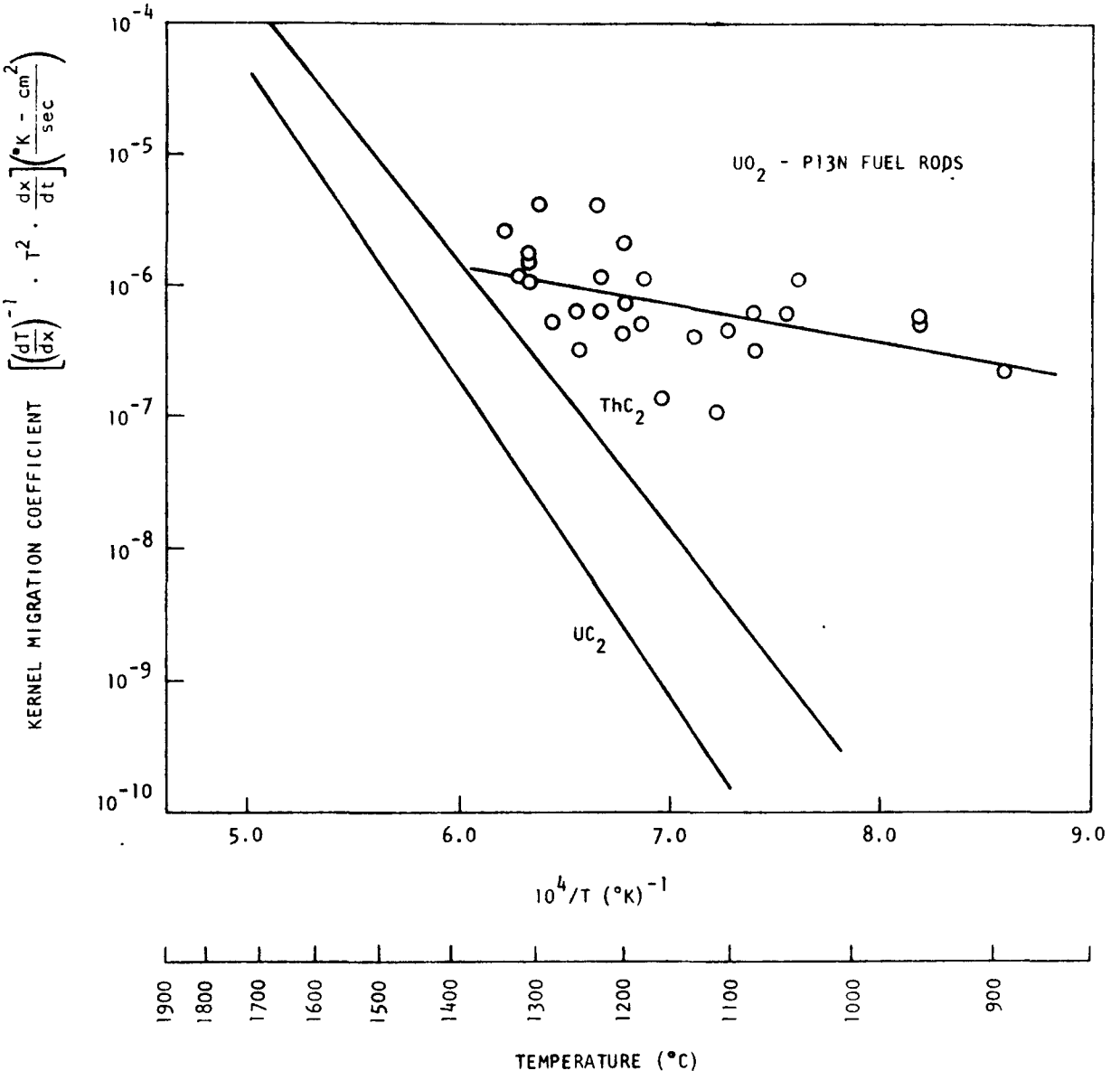

Fig. 9-1. Kernel migration coefficient versus 1/T for UO_2 TRISO particles from fuel rods 2D-16, 2A-10, 4D-9, and 5A-19 irradiated in capsule P13N. Kernel migration data for unirradiated ThC_2 and UC_2 are also shown.

The capsule was inserted in the ETR on April 11, 1972, in the J-10-5E position. Cadmium shield capsules were placed in adjacent holes of the J-10 filler piece to reduce the high peak thermal flux to the P13P design value (2.6×10^{14} nv). The capsule completed its scheduled irradiation to $\sim 8 \times 10^{21}$ n/cm^2 (design) in April 1973 and was transferred to the GGA Hot Cell facility. Disassembly of the capsule was completed and the fuel samples are currently undergoing postirradiation examination.

Initial results of the P13P postirradiation examination are encouraging since the macroscopic examination of the reference size (200 μm) UC_2 TRISO particles indicates all samples survived irradiation. Also, metallographic examination of a peak exposure fuel rod (7 to 8 x 10^{21} n/cm^2 at 1350°C) containing the 200-μm UC_2 TRISO particles revealed very good irradiation performance of these particles under the relatively severe conditions. A more detailed description of the P13P postirradiation examination results will be presented in the next Quarterly Progress Report.

Capsules P13R and P13S

Capsules P13R and P13S are the seventh and eighth in a series of irradiation tests conducted under the AEC-sponsored HTGR Base Program. The purpose of these tests is to demonstrate the integrity of reference and alternate large HTGR fuels over a wide range of irradiation conditions. These tests have the following four primary objectives:

1. Obtain irradiation data on a broad spectrum of property (and process) variables for reference large HTGR fuel.

2. Obtain temperature-fluence dependence on in-pile fission gas release and relate to coated particle integrity.

3. Determine effect of thermal cycling on fuel integrity.

4. Test alternate fuel materials.

These capsules are nearly identical in design; each contains four fuel rod cells and two unbonded particle cells. Twenty rods (five per cell) and 20 to 22 unbonded coated particle batches will be tested in each capsule (see Fig. 9-2). The individual cells have separate purge gas systems which provide the means for temperature control. The purge gas is also sampled separately for each cell in order to measure the in-pile fission gas release.

Capsules P13R and P13S are scheduled to begin their irradiation in mid-December 1973 in the E7 position in the GETR. Both capsules are designed to reach full HTGR fast fluence in the peak exposure positions ($\sim 9 \times 10^{21}$ n/cm^2, E > 0.18 MeV_{GETR}). Because of the axial flux gradient in the test reactor, the neutron exposures will range from $\sim 4 \times 10^{21}$ n/cm^2 to 9×10^{21} n/cm^2.

Fuel rod samples in P13R and P13S will be irradiated at three temperatures: 1075°, 1300°, and 1500°C. The majority of the samples will be irradiated at 1075°C to 5.5 and 9.0×10^{21} n/cm^2. One set of capsule rods will be irradiated at 1300°C (P13R) and 1500°C (P13S) to 6.5×10^{21} n/cm^2 in order to obtain in-pile fission gas release data as a function of temperature and fluence, as well as to demonstrate fuel integrity under these very severe irradiation exposures. These combinations of irradiation exposures envelope peak temperature and fast fluence conditions to be experienced by $\geq$99.5% of the fuel during its residence time in a large HTGR (under nominal operating conditions).

One series of fuel rods (cell 1, P13S) will be thermal cycled from its nominal operating temperature of 1075°C to 1500°C once every GETR fuel cycle ($\sim$26 times/year). This test is the first attempt to simulate temperature cycling that results from load following and/or control rod pattern changes in the large HTGR. Fission gas release measurements will be made before and after each thermal cycle. Identical fuel rods will be irradiated in cell 1 of P13R at a constant temperature of 1075°C for comparative purposes.

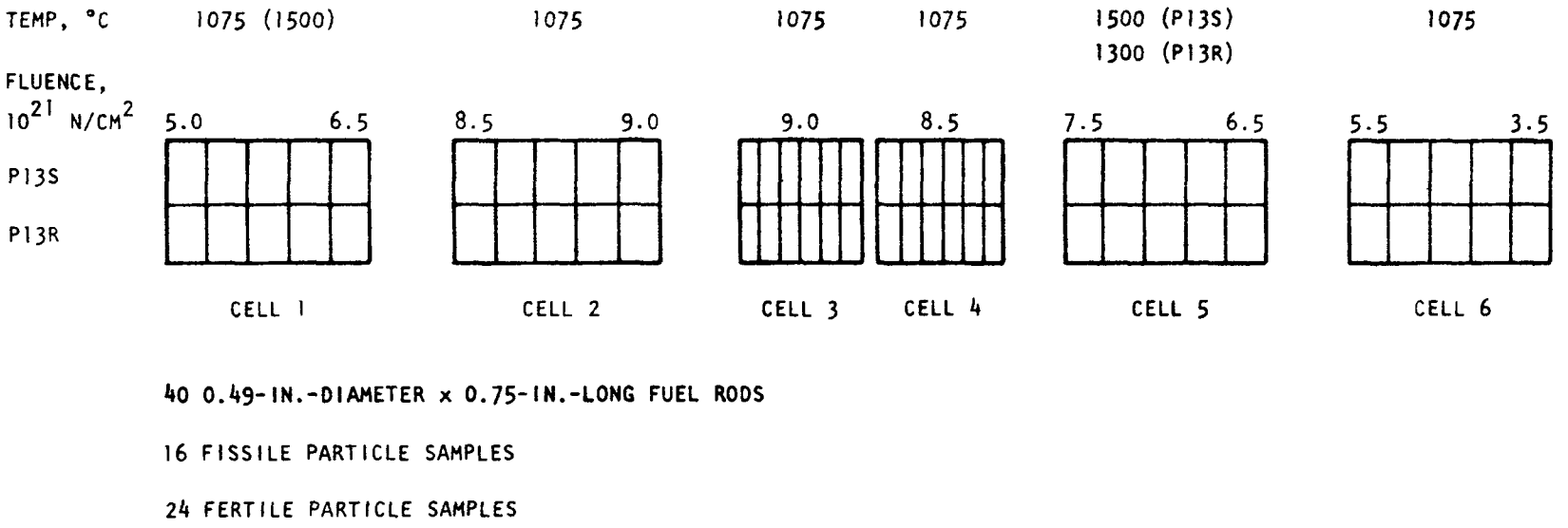

Fig. 9-2. Schematic layout showing temperature-fluence conditions for capsules P13R and P13S

A description of the fuel rod variables being investigated in these tests is given in Tables 9-1 through 9-3.

All unbonded particle samples will be irradiated at 1075°C to full HTGR fast fluence, $\sim 9 \times 10^{21}$ n/cm$^2_{GETR}$. A description of these samples is given in Tables 9-4 through 9-7.

Capsule P13T

Initial planning for the P13T capsule experiment is now under way. This capsule is scheduled to begin irradiation in the ORR in September 1974.

The primary objective of this test is to irradiate cure-in-place fuel rods that most closely represent the fuel for the large HTGR. Secondary objectives will be to obtain irradiation data on fuel rod matrix variables and to test rods containing $(Th,U)O_2$ particles. Fuel rods will also contain several UC_2 TRISO and ThO_2 BISO batches with coating attributes within the expected specification limit.

Capsule P13T will be a large-diameter capsule containing two separate cells. Cell 1 will contain a 2.4-in.-diameter x 8-in.-long graphite body loaded with nine 0.62-in.-diameter, 2.4-in.-long fuel rods. Cell 2 will be composed of three individual graphite bodies each approximately 5 in. long. These bodies will hold six 2.4-in.-long rods and fifteen 1.6-in.-long rods.

GGA-ORNL Cooperative Irradiation Capsules

A series of cooperative irradiation tests are being carried out with ORNL in their irradiation facilities. These irradiations include tests in the HFIR target position (HT-capsules), the HFIR beryllium-reflector position (HRB-capsules), and the ORR facility.

TABLE 9-1

DESCRIPTION OF FUEL RODS[a] BEING TESTED IN CAPSULE P13R

Capsule Position	Sample Number 7161-004-	Coated Particles[b]						Matrix				Particle Packing[f,g] (%)	Fuel Loading Uniformity[k]		Fission[l] Gas Release	Thorium[g,m] Contamination (g Th/g Th)
		Fissile[c]		Fertile[d]		Shim Particles		Filler[e] (wt %)	Apparent Density[f,g] (g/cm^3)	Macro-porosity[h,i] (%)	Apparent Pitch Coke Yield[g,j] (%)		U-235	Th-232		
		Type	Batch Number	Type	Batch Number	Type	Batch Number									
Cell 1																
A[n]	01-5	UC_2	6151-00-045	ThO_2	6542-20-035	1099-I[o]	FO 147	37	--	31	--	--	1.05	1.05	2×10^{-6}	$<8 \times 10^{-6}$
B	02-6	UC_2	6151-00-035	ThO_2	6542-02-020	1099-N[p]	FO 82	34	0.71	40	39	56	1.00	1.02	1×10^{-6}	$<8 \times 10^{-6}$
C	03-5	UC_2	6151-00-035	ThO_2	6542-01-010	1099-I	FO 136	33	0.67	42	36	55	1.03	1.06	1×10^{-6}	$<8 \times 10^{-6}$
D	04-6	UC_2	6151-00-035	ThO_2	6542-01-020	1099-I	FO 136	34	0.68	35	36	57	1.04	1.12	3×10^{-6}	$<9 \times 10^{-6}$
E[n]	05-6	$(Th,U)O_2$	5466-37	ThO_2	6542-02-020	1099-I	FO 147	34	--	32	--	--	1.03	1.07	4×10^{-6}	$<9 \times 10^{-6}$
Cell 2																
A[n]	06-5	UC_2	6151-00-045	ThO_2	6542-20-035	1099-I	FO 147	32	--	37	--	--	1.05	1.11	3×10^{-6}	$<9 \times 10^{-6}$
B	07-5	UC_2	6151-00-035	ThO_2	6542-02-020	1099-I	FO 136	42	0.77	28	41	56	1.08	1.10	3×10^{-6}	$<9 \times 10^{-6}$
C	08-13	UC_2	6151-00-035	ThO_2	6542-01-010	1099-I	FO 148	29	0.65	37	28	56	1.02	1.04	4×10^{-6}	$<9 \times 10^{-6}$
D	09-5	UC_2	6151-00-035	ThO_2	6542-01-020	Lonza	FO 149	33	0.66	36	31	57	1.02	1.04	3×10^{-6}	$<1 \times 10^{-5}$
E[n]	10-5	$(Th,U)O_2$	5466-37	ThO_2	6542-01-010	1099-I	FO 147	42	--	37	--	--	1.01	1.08	6×10^{-6}	$<1 \times 10^{-5}$
Cell 5																
A[n]	16-5	$(Th,U)O_2$	5466-37	ThO_2	6542-01-020	1099-I	FO 147	35	--	37	--	--	1.01	1.00	4×10^{-6}	$<6 \times 10^{-6}$
B	17-5	UC_2	6151-00-035	ThO_2	6542-02-020	1099-N	FO 82	34	0.71	35	40	56	1.03	1.07	2×10^{-6}	$<7 \times 10^{-6}$
C	18-6	UC_2	6151-00-035	ThO_2	6542-01-010	1099-I	FO 136	30	0.69	35	35	55	1.09	1.06	3×10^{-6}	$<7 \times 10^{-6}$
D	19-7	UC_2	6151-08-015	ThO_2	6542-19-015	1099-I	FO 136	33	0.68	42	37	56	1.03	1.09	2×10^{-6}	$<7 \times 10^{-6}$
E[n]	20-6	UC_2	6151-09-015	ThO_2	6542-09-010	1099-I	FO 147	32	--	27	--	--	1.04	1.08	3×10^{-6}	$<6 \times 10^{-6}$
Cell 6																
A[n]	21-5	UC_2	6151-08-015	ThO_2	6542-19-015	1099-I	FO 147	33	--	34	--	--	1.07	1.10	4×10^{-6}	$<9 \times 10^{-6}$
B	22-5	UC_2	6151-09-015	ThO_2	6542-09-010	1099-I	FO 136	32	0.70	41	38	56	1.06	1.09	2×10^{-6}	$<8 \times 10^{-6}$
C	23-5	UC_2	6151-00-035	ThO_2	6542-01-010	1099-I	FO 136	30	0.57	43	25	54	1.07	1.12	2×10^{-6}	2×10^{-4}[q]
D	24-5	UC_2	6151-00-035	ThO_2	6542-02-020	Lonza	FO 149	31	0.67	40	31	56	1.10	1.13	6×10^{-6}	$<9 \times 10^{-6}$
E[n]	25-5	UC_2	6151-00-045	ThO_2	6542-20-035	1099-I	FO 147	33	--	36	--	--	1.03	1.03	3×10^{-6}	$<1 \times 10^{-5}$

(a) All rods are approximately 1.25 cm (0.493-in.) in diameter by 1.90 cm (0.75-in.) long.

(b) All rods except cell 1, position B and position C, contain TRISO coated carbon inert particles (batch number 6351-02-020).

(c) All fissile particles are TRISO coated

(d) All fertile particles are BISO coated

(e) Measurement made on companion green rod.

(f) Calculated from fired rod and mean particle parameters.

(g) Not meaningful to determine value for thermocouple rods due to some uncertainty in green and fired parameters.

(h) Measurement made on comapnion fired rod.

(i) Determined from metallographic cross section.

(j) Calculated from green and fired rod and mean particle weights.

(k) Determined by gamma counting both ends of rod and calculating ratio of maximum and mean values.

(l) Release ratio/birth rate for Kr-85m at 1100°C.

(m) Determined by hydrolysis test. Value indicates amount of exposed thorium. "<" denotes the amount is below the limit of detection of apparatus. If detectable quantity, the value is corrected for total conversion of ThO_2 to ThC_2.

(n) Thermocouple rod - center hole [approximately 0.34 cm (0.13-in.) in diameter] through entire length of rod.

(o) I signifies impregnated with furfuryl alcohol.

(p) N signifies nonimpregnated

(q) Second rod from this batch had a value of $<9 \times 10^{-6}$.

TABLE 9-2

DESCRIPTION OF FUEL RODS[a] BEING TESTED IN CAPSULE P13S

Capsule Position	Sample Number 7161-004-	Coated Particles[b]				Shim Particles		Matrix				Particle Packing[f,g] (%)	Fuel Loading Uniformity[k] (peak/average)		Fission[l] Gas Release	Thorium[g,m] Contamination (g Th/g Th)
		Fissile[c]		Fertile[d]				Filler[e] (wt %)	Apparent Density[f,g] (g/cm^3)	Macro-porosity[h,i] (%)	Apparent Pitch Coke Yield[g,j] (%)		U-235	Th-232		
		Type	Batch Number	Type	Batch Number	Type	Batch Number									
Cell 1																
A[n]	01-7	UC_2	6151-00-045	ThO_2	6542-20-035	1099-I[o]	FO 147	37	--	31	--	--	1.07	1.10	2×10^{-6}	$<8 \times 10^{-6}$
B	02-5	UC_2	6151-00-035	ThO_2	6542-02-020	1099-N[p]	FO 82	34	0.67	40	36	56	1.07	1.07	1×10^{-6}	$<8 \times 10^{-6}$
C	03-6	UC_2	6151-00-035	ThO_2	6542-01-010	1099-I	FO 136	33	0.66	42	34	55	1.10	1.07	1×10^{-6}	$<8 \times 10^{-6}$
D	04-5	UC_2	6151-00-035	ThO_2	6542-01-020	1099-I	FO 136	34	0.68	35	36	57	1.11	1.09	2×10^{-6}	$<9 \times 10^{-6}$
E[n]	05-5	$(Th,U)O_2$	5466-37	ThO_2	6542-02-020	1099-I	FO 147	34	--	32	--	--	1.00	1.02	2×10^{-6}	$<9 \times 10^{-6}$
Cell 2																
A[n]	11-6	UC_2	6151-00-045	ThO_2	6542-20-035	1099-I	FO 148	29	--	36	--	--	1.02	1.08	2×10^{-7}	$<9 \times 10^{-6}$
B	12-5	UC_2	6151-09-015	ThO_2	6542-09-010	1099-I	FO 136	32	0.70	32	35	55	1.02	1.07	2×10^{-6}	6×10^{-3}[q]
C	13-6	UC_2	6151-00-035	ThO_2	6542-01-010	1099-I	FO 148	31	0.59	35	25	53	1.10	1.10	3×10^{-6}	$<9 \times 10^{-6}$
D	14-5	UC_2	6151-00-035	ThO_2	6542-02-020	1099-N	FO 82	36	0.69	36	36	56	1.00	1.02	2×10^{-6}	$<1 \times 10^{-5}$
E[n]	15-5	UC_2	6151-08-015	ThO_2	6542-19-015	1099-I	FO 147	36	--	26	--	--	1.05	1.03	5×10^{-6}	$<1 \times 10^{-5}$
Cell 5																
A[n]	16-6	$(Th,U)O_2$	5466-37	ThO_2	6542-01-020	1099-I	FO 147	35	--	37	--	--	1.02	1.01	4×10^{-6}	$<6 \times 10^{-6}$
B	17-6	UC_2	6151-00-035	ThO_2	6542-02-020	1099-N	FO 82	34	0.67	35	38	56	1.08	1.06	1×10^{-6}	$<7 \times 10^{-6}$
C	18-5	UC_2	6151-00-035	ThO_2	6542-01-010	1099-I	FO 136	30	0.68	35	35	55	1.07	1.10	2×10^{-6}	$<7 \times 10^{-6}$
D	19-5	UC_2	6151-08-015	ThO_2	6542-19-015	1099-I	FO 136	33	0.73	42	36	56	1.11	1.09	3×10^{-6}	$<7 \times 10^{-6}$
E[n]	20-5	UC_2	6151-09-015	ThO_2	6542-09-010	1099-I	FO 147	32	--	27	--	--	1.09	1.11	3×10^{-6}	$<6 \times 10^{-6}$
Cell 6																
A[n]	26-5	UC_2	6151-00-035	ThO_2	6542-01-020	1099-N	FO 82	33	--	40	--	--	1.06	1.10	3×10^{-6}	$<9 \times 10^{-6}$
B	27-5	$(Th,U)O_2$	5466-37	ThO_2	6542-02-020	1099-I	FO 136	32	0.71	29	35	55	1.00	1.08	1×10^{-6}	$<8 \times 10^{-6}$
C	28-13	UC_2	6151-00-035	ThO_2	6542-01-010	1099-I	FO 148	29	0.64	38	31	55	1.03	1.09	4×10^{-6}	$<8 \times 10^{-6}$
D	29-5	UC_2	6151-00-035	ThO_2	6542-01-020	1099-I	FO 136	44	0.79	32	39	57	1.06	1.11	1×10^{-6}	$<9 \times 10^{-6}$
E[n]	30-5	UC_2	6151-00-045	ThO_2	6542-20-035	1099-I	FO 147	39	--	30	--	--	1.03	1.10	2×10^{-6}	$<1 \times 10^{-5}$

(a) All rods are approximately 1.25 cm (0.493-in.) in diameter by 1.90 cm (0.75-in.) long.

(b) All rods except cell 1, position B and position C, contain TRISO coated carbon inert particles (batch number 6351-02-020).

(c) All fissile particles are TRISO coated

(d) All fertile particles are BISO coated

(e) Measurement made on companion green rod.

(f) Calculated from fired rod and mean particle parameters.

(g) *Not meaningful to determine value for thermocouple rods due to some uncertainty in green and fired parameters.*

(h) Measurement made on comapnion fired rod.

(i) Determined from metallographic cross section.

(j) Calculated from green and fired rod and mean particle weights.

(k) Determined by gamma counting both ends of rod and calculating ratio of maximum and mean values.

(l) Release ratio/birth rate for Kr-85m at 1100°C.

(m) Determined by hydrolysis test. Value indicates amount of exposed thorium. "<" denotes the amount is below the limit of detection of apparatus. If detectable quantity, the value is corrected for total conversion of ThO_2 to ThC_2.

(n) Thermocouple rod - center hole [approximately 0.34 cm (0.13-in.) in diameter] through entire length of rod.

(o) I signifies *impregnated with furfuryl alcohol.*

(p) N signifies nonimpregnated

(q) Second rod from this batch had a value of $<9 \times 10^{-6}$.

TABLE 9-3

FUEL ROD VARIABLES[a] BEING TESTED IN CAPSULES P13R AND P13S

Rod Location	Coated Particles		Shim		Matrix		Firing Conditions
	Fissile	Fertile	Particles	Loading	Filler	Additive	
Cell 1							
P13R & P13S							
A[b]	Faceted	Faceted	Ref	Low	Ref[c]	Ref	Ref
B	WESL[d]	WESL	Nonimpregnated	High	Ref	Ref	Ref
C	WESL	WESL	Ref	High	Ref	Ref	Ref
D	WESL	WESL	Ref	Ref	Ref	Ref	1500°C firing
E[b]	Oxide	WESL	Ref	Ref	Ref	Ref	Ref
Cell 2							
P13R							
A[b]	Faceted	Faceted	Ref	Ref	Ref	Ref	1500°C firing
B	WESL	WESL	Ref	Ref	Lonza	Ref	Ref
C	WESL	WESL	Ref	Ref	Ref	Ref	Packed bed[e]
D	WESL	WESL	Lonza	Ref	Ref	SC003	Ref
E[b]	Oxide	WESL	Ref	High	Ref	Ref	Ref
P13S							
A[b]	Faceted	Faceted	Ref	Ref	Ref	Ref	N_2 atmosphere
B	High OPyC density	High OPyC density	Ref	Ref	Ref	Ref	Ref
C	WESL	WESL	Ref	High	Ref	SC027[e]	Ref
D	WESL	WESL	Nonimpregnated	Ref	Ref	Ref	Ref
E[b]	Low OPyC density	Low OPyC density	Ref	High	Ref	Ref	Ref
Cell 5							
P13R & P13S							
A[b]	Oxide	WESL	Ref	Ref	Ref	Pef	Ref
B	WESL	WESL	Nonimpregnated	High	Ref	Ref	Ref
C	WESL	WESL	Ref	Ref	Ref	Ref	1500°C firing
D	Low OPyC density	Low OPyC density	Ref	Ref	Ref	Ref	N_2 firing
E[b]	High OPyC density	High OPyC density	Ref	Low	Ref	Ref	Ref
Cell 6							
P13R							
A[b]	Low OPyC density	Low OPyC density	Ref	Ref	Ref	Ref	Ref
B	High OPyC density	High OPyC density	Ref	Low	Ref	Ref	Ref
C	WESL	WESL	Ref	High	Ref	SC027[e]	Ref
D	WESL	WESL	Lonza	Ref	Ref	SC003	Ref
E[b]	Faceted	Faceted	Ref	Ref	Ref	Ref	N_2 firing
P13S							
A[b]	WESL	WESL	Nonimpregnated	Ref	Ref	Ref	Ref
B	Oxide	WESL	Ref	Low	Ref	Ref	Ref
C	WESL	WESL	Ref	High	Ref	Ref	Packed bed[e]
D	WESL	WESL	Ref	Ref	Lonza	Ref	Ref
E[b]	Faceted	Faceted	Ref	Ref	Ref	Ref	1500°C firing

[a] Reference fuel rod attributes:

Fissile particles: UC_2 TRISO, 1.8 g/cm^3, OPyC, round
Fertile particles: ThO_2 TRISO, 1.85 g/cm^3, OPyC, round
Shim: impregnated GLCC 1099, 20 to 27 vol %
Matrix: 6353 filler, A240 pitch, SC011 additive
Carbonizing and firing conditions: In-block (H-451) to 1800°C in argon

All rods hot-injected, except P13R Cell 2-C and Cell 6-C which were slug-injected.

[b] Thermocouple rods.

[c] Ref denotes reference.

[d] Within estimated specification limits.

[e] Variable reduces the pitch coke content in rod matrix.

TABLE 9-4

TRISO COATED FISSILE PARTICLE VARIABLES[a] BEING TESTED IN IRRADIATION EXPERIMENTS P13R AND P13S

Primary Variable	Data Retrieval Number	Comments
Reference TRISO coated UC_2[b]	6151-00-035	OPyC density 1.85 g/cm^3, coating rate 4.0 µm/min
OPyC density/coating rate	6151-00-010	OPyC density 1.80 g/cm^3, coating rate 1.1 µm/min
Faceting and OPyC density/coating rate	6151-00-025	OPyC density 1.88 g/cm^3, coating rate 1.4 µm/min
Faceting and OPyC density/coating rate	6151-00-045	OPyC density 1.81 g/cm^3, coating rate 3.8 µm/min
Faceting and OPyC density/coating rate	6151-00-046	Same as 6151-00-045, except the material was tabled to isolate the most severely faceted particles
OPyC density/coating rate	6151-08-015	OPyC density 1.76 g/cm^3, coating rate 3.6 µm/min
OPyC density/coating rate	6151-02-025	OPyC density measurements vary between 1.50 and 1.66, coating rate 0.7 µm/min
OPyC density/coating rate	6151-01-015	OPyC 1.90 g/cm^3, coating rate 0.7 µm/min
OPyC density/coating rate	6151-09-015	OPyC density 1.94 g/cm^3, coating rate 3.6 µm/min
OPyC density	6151-09-025	OPyC density 1.95 g/cm^3
IPyC coating rate	6151-04-015	IPyC coating rate 0.7 µm/min
Interrupted SiC layer	6151-03-015	
Interrupted SiC layer	4161-01-021	
TRISO coated $(Th,U)O_2$	4163-00-010	Th/U ratio of 1/1; 73 µm buffer
TRISO coated $(Th,U)O_2$	5466-37	Th/U ratio of 1/1; 107 µm buffer
TRISO coated $(Th,U)O_2$	6155-01-020	Th/U ratio of 8/1

[a] Unless noted otherwise, all particles have 200 µm kernels.

[b] Reference coatings are: buffer - 100 µm thick, 1.1 g/cm^3; IPyC - 30 µm thick, 1.95 g/cm^3; SiC - 25 µm thick, >3.18 g/cm^3; OPyC - 40 µm thick, 1.80 g/cm^3.

TABLE 9-5

FERTILE PARTICLE VARIABLES BEING TESTED IN IRRADIATION EXPERIMENTS P13R AND P13S

Primary Variable	Data Retrieval Number	Comments[a]
Reference	4252-02-010	Previously irradiated in HT-12 through -15
	4252-06-010	Previously irradiated in HT-12 through -15
Coating design	6542-16-010	Buffer thickness 39 μm, density 1.08 g/cm^3; OPyC thickness 55 μm, density 1.81 g/cm^3; currently being irradiated in HT-17 through -19
	6542-17-010	Buffer thickness 44 μm, density 0.95 g/cm^3; OPyC thickness 122 μm, density 1.86 g/cm^3; currently being irradiated in HT-17 through -19
OPyC density and coating rate	6542-01-010	OPyC density 1.80 g/cm^3, coating rate 10.0 μm/min; currently being irradiated in P13Q and HT-17 through -19
	6542-01-020	OPyC density 1.82 g/cm^3, coating rate 2.72 μm/min; currently being irradiated in HT-17 through -19
	6542-02-020	OPyC density 1.91 g/cm^3, coating rate 8.5 μm/min; currently being irradiated in HT-17 through -19
	6542-02-030	OPyC density 1.89 g/cm^3, coating rate 2.16 μm/min; currently being irradiated in HT-17 through -19
	6542-09-010	OPyC density 1.93 g/cm^3, coating rate 5.0 μm/min
	6542-19-015	OPyC density 1.78 g/cm^3
Constant total particle density	4252-06-018[b]	Density separated from 4252-06-010; OPyC density 1.82 g/cm^3
	6542-19-016	Density separated from 6542-19-010; OPyC density 1.78 g/cm^3
	6542-21-016	Density separated from 6542-21-010; OPyC density 1.73 g/cm^3
Faceted coatings	6542-20-025	OPyC density 1.80 to 1.90 g/cm^3
	6542-20-035	OPyC density 1.80 to 1.90 g/cm^3
Mixed gas OPyC layer	6542-21-015	OPyC density 1.73 g/cm^3
	6542-22-015	OPyC density 1.80 g/cm^3, coating rate 2 to 3 μm/min
	6542-22-025	OPyC density 1.81 g/cm^3, coating rate 7 to 10 μm/min
	6542-23-025	OPyC density 1.89 g/cm^3
	6542-24-015	OPyC density 1.94 g/cm^3
N_2 carrier gas buffer	6542-12-025	
No seal coat	6542-11-015	OPyC density 1.80 to 1.90 g/cm^3
	6542-18-015	OPyC density 1.80 to 1.90 g/cm^3
Nonround kernels	6542-25-015	OPyC density 1.80 to 1.90 g/cm^3
TRISO coating	6252-00-025	Comparison of TRISO and BISO coated ThO_2

[a] Unless indicated otherwise, desired average particle attributes are: kernel diameter 480 to 520 μm, density 9.5 to 10.0 g/cm^3; buffer thickness 80 to 90 μm, density 1.0 to 1.2 g/cm^3; seal coat; OPyC thickness 70 to 80 μm, density 1.80 to 1.90 g/cm^3, OPTAF $\leq$1.20.

[b] Also screened to a specific size range.

Capsule P13Q

Capsule P13Q is designed to demonstrate the performance of fuel rods fabricated using candidate large HTGR processes and materials. Experiment P13Q is the GGA portion of GGA-ORNL cooperative experiment OF-1. The GGA and ORNL halves of the test are separated by a sealed bulkhead, and each half of the test will be controlled and monitored by separate systems.

Eighteen fuel rods, 0.63 in. in diameter by 2 in. long, are being irradiated in isotropic H-451 graphite bodies in a configuration similar to that planned for the large HTGR. The experiment is designed to operate isothermally in the ORR at a peak fuel rod temperature of 1150°C to a maximum fast neutron fluence of 9×10^{21} n/cm^2. Descriptions of the coated particles and fuel rods included in capsule P13Q are given in Tables 9-8 and 9-9.

The P13Q experiment began its irradiation in the E-3 position of the ORR on August 29, 1973. Initial temperature measurements were 100° to 350°C below predicted values. This indicates actual powers (thermal flux levels) in the P13Q portion of the capsules are lower than design. Gas mixture adjustments have brought two of the three bodies close to their design temperatures of 1150°C; however, the uppermost body in the cell continues to operate about 150°C below the desired temperature of 1150°C.

Initial fission gas measurements indicate very low releases from the fuel in P13Q. Values for Kr-85m R/B have been running $< 10^{-6}$ since capsule startup.

Capsules HRB-4 and HRB-5

Capsules HRB-4 and HRB-5 represent a cooperative GGA-ORNL irradiation effort designed to evaluate the irradiation performance of fuel rods fabricated using candidate processes and materials for large HTGR startup and recycle fuel systems. Capsules HRB-4 and HRB-5 are companion capsules and were inserted in the beryllium-reflector position of the HFIR on October 8,

TABLE 9-6

DESCRIPTION OF COATED PARTICLES BEING TESTED IN CAPSULE P13R

Data Retrieval Number	Kernel			Coating												Total Coated Particle							Particle Disposition		
				Buffer		Inner Isotropic PyC			SiC		Outer Isotropic PyC				Total Coating Thickness (μm)			Metal Loading			Surface Contamination[d]		Used In		
	Type	Mean Diameter (μm)	Type[a]	Thickness (μm)	Density (g/cm³)	Thickness (μm)	Density (g/cm³)	OPTAF[b]	Thickness (μm)	Density (g/cm³)	Thickness (μm)	Density (g/cm³)	Coating Rate (μm/min)	OPTAF[b]		Mean Diameter (μm)	Density (g/cm³)	U (wt %)	Th (wt %)	Fission Gas Release[c]	U (g U/g U)	Th (g Th/g Th)	Fuel Rods	Unbonded Test	Unbonded Particle Position
Fissile Particles[e]																									
5466-37	$(Th,U)O_2$	258	TRISO	107	1.12	29	1.87	1.07	30	3.18	31	1.79	6.0	1.10	197	619	2.37	12.7	12.3	1×10^{-6}	2×10^{-7}	6×10^{-5}	X		-
6151-00-010	UC_2[f]	199	TRISO	97	1.18	35	1.94	1.19	31	3.20	44	1.80	1.1	1.11	207	595	2.28	17.3	0.43	4×10^{-7}	-	-		X	C3T1,2,3[g]
6151-00-025	UC_2	190	TRISO	98	1.15	35	1.93	1.16	31	3.20	33	1.88	1.4	1.17	197	561	2.36	18.0	-	6×10^{-8}	4×10^{-7}	-		X	C4T4,5,6
6151-00-035	UC_2[f]	196	TRISO	87	1.07	33	1.92	1.22	32	3.20	38	1.85	4.0	1.17	190	575	2.29	18.9	-	3×10^{-7}	4×10^{-7}	-	X	X	C3T4,5,6
6151-00-045	UC_2	196	TRISO	88	1.15	35	1.93	1.17	29	3.22	40	1.81	3.8	1.13	192	578	2.33	17.8	-	2×10^{-7}	1×10^{-7}	-	X	X	C3T7,8,9
6151-00-046[h]	UC_2	196	TRISO	88	1.15	35	1.93	1.17	29	3.22	40	1.81	3.3	1.13	192	578	2.33	17.8	-	2×10^{-7}	1×10^{-7}	-		X	C3T10
6151-01-015	UC_2[f]	197	TRISO	105	1.15	31	1.94	1.20	25	3.21	42	1.90	0.7	1.15	203	590	2.28	17.4	0.22	1×10^{-8}	1×10^{-7}	-		X	C4T1,2,3
6151-04-015	UC_2[f]	202	TRISO	105	0.87	33	1.88	1.23	28	3.20	36	1.82	1.4	1.14	202	599	2.45	17.4	0.22	8×10^{-7}	1×10^{-6}	9×10^{-4}		X	C3T11,12
6151-08-015	UC_2[f]	202	TRISO	95	1.07	33	1.92	1.25	26	3.21	36	1.76	3.6	1.09	190	593	2.28	18.6	-	1×10^{-7}	9×10^{-7}	-	X		-
6151-09-015	UC_2[f]	197	TRISO	105	1.15	31	1.94	1.16	29	3.22	39	1.94	3.6	1.06	204	587	2.30	17.8	-	9×10^{-8}	4×10^{-7}	-	X	X	C4T7,8,9
6151-09-025	UC_2[f]	197	TRISO	97	1.18	35	1.94	1.14	31	3.22	41	1.95	4.0	1.11	204	590	2.37	17.5	-	2×10^{-7}	8×10^{-7}	-		X	C4T10,11,12
Fertile Particles																									
4252-06-018[i]	ThO_2	511	BISO	78	1.10	-	-	-	-	-	77	1.82	5.8	1.14	155	826	3.67	-	58.9	-	-	7×10^{-4}		X	C3T1,2
6542-01-010	ThO_2	500	BISO	79	1.08	-	-	-	-	-	85	1.80	10.0	1.06	164	828	3.59	-	56.5	-	-	6×10^{-6}	X	X	C3T5,6
6542-01-020	ThO_2	504	BISO	81	1.17	-	-	-	-	-	74	1.82	2.7	1.10	155	813	3.55	-	57.5	-	-	6×10^{-6}	X	X	C3,T3,4,7,8
6542-02-020	ThO_2	481	BISO	87	1.08	-	-	-	-	-	72	1.91	8.5	1.06	159	796	3.59	-	56.2	-	-	2×10^{-5}	X	X	C4T5,6
6542-02-030	ThO_2	481	BISO	79	1.18	-	-	-	-	-	74	1.89	2.2	1.12	153	786	3.54	-	56.0	-	-	8×10^{-5}		X	C3T9,10
6542-09-010	ThO_2	511	BISO	84	1.06	-	-	-	-	-	75	1.93	5.0	1.13	159	822	3.56	-	57.6	-	-	1×10^{-4}	X	X	C3T11,12
6542-11-015	ThO_2	497	BISO	87	1.12	-	-	-	-	-	74	1.83	2.6	1.29	161	819	3.35	-	57.8	-	-	6×10^{-7}		X	C4T1,2
6542-18-015	ThO_2	476	BISO	84	1.11	-	-	-	-	-	70	1.84	6.5	1.13	154	791	3.53	-	58.8	-	-	3×10^{-6}		X	C4T3,4
6542-19-015	ThO_2	486	BISO	81	1.15	-	-	-	-	-	77	1.78	7.5	1.16	158	824	3.55	-	58.9	-	-	4×10^{-6}	X		-
6542-20-025	ThO_2	495	BISO	76	1.25	-	-	-	-	-	81	1.82	3.5	1.18	157	809	3.57	-	58.2	-	-	3×10^{-6}		X	C4T9,10
6542-20-035	ThO_2	462	BISO	80	1.20	-	-	-	-	-	83	1.84	3.6	1.15	163	810	3.50	-	57.4	-	-	1×10^{-6}	X	X	C4T7,8
6542-25-015	ThO_2	489	BISO	79	1.21	-	-	-	-	-	76	1.82	7.0	1.11	155	826	3.57	-	58.2	-	-	1×10^{-6}		X	C4T11,12
Inert Particles																									
6351-01-020	C	253	TRISO	-	-	29	1.76	1.09	29	3.22	36	1.75	-	1.12	-	573	1.83	-	-	-	-	-	X		-

(a) TRISO denotes a coating design with a SiC layer and BISO denotes a particle with no SiC layer.
(b) Optical anisotropy factor, relative units.
(c) Release rate/birth rate for Kr-85m at 1100°C.
(d) Determined by leach test.
(e) Fissile material 93.15% enriched.
(f) Kernels Th doped.
(g) C denotes cell; T denotes tray. Each tray holds approximately 225 fissile particles and 450 fertile particles.
(h) Nonround particles separated from parent batch 6151-00-045 using a vibrating table. Parameters listed are for parent batch.
(i) Density and size separated from parent batch 4252-06-010.

TABLE 9-7

DESCRIPTION OF COATED PARTICLES BEING TESTED IN CAPSULE P13S

Data Retrieval Number	Kernel			Coating											Total Coating Thickness (μm)	Total Coated Particle								Particle Disposition		
				Buffer		Inner Isotropic PyC			SiC		Outer Isotropic PyC													Used In		
	Type	Mean Diameter (μm)	Type[a]	Thickness (μm)	Density (g/cm³)	Thickness (μm)	Density (g/cm³)	OPTAF[b]	Thickness (μm)	Density (g/cm³)	Thickness (μm)	Density (g/cm³)	Coating Rate (μm/min)	OPTAF[b]		Mean Diameter (μm)	Density (g/cm³)	Metal Loading U (wt %)	Metal Loading Th (wt %)	Fission Gas Release[c]	Surface Contamination[d] U (g U/g U)	Surface Contamination[d] Th (g Th/g Th)	Fuel Rods	Unbonded Test	Unbonded Particle Position
Fissile Particles[e]																										
4161-01-021	UC_2	189	TRISO	82	1.31	29	1.91	1.16	30	3.20	32	1.82	3.4	1.07	173	541	2.47	20.8	-	5×10^{-6}	6×10^{-7}	-		X	C3T4,5,6[f]
4163-00-011	$(Th,U)O_2$	253	TRISO	69	1.17	32	1.78	1.14	36	3.20	72	1.77	4.1	1.09	209	690	2.37	9.2	9.2	3×10^{-9}	6×10^{-6}	3×10^{-5}		X	C4T1,2,3
5466-37	$(Th,U)O_2$	258	TRISO	107	1.12	29	1.87	1.07	30	3.18	31	1.79	6.0	1.10	197	619	2.37	12.7	12.3	1×10^{-6}	2×10^{-7}	6×10^{-5}	X	X	C4T7,8,9
6151-00-035	UC_2(g)	204	TRISO	99	1.07	33	1.92	1.25	27	3.22	27	1.85	4.0	1.17	190	575	2.29	18.9	-	3×10^{-7}	4×10^{-7}	-	X	X	C4T10,11,12
6151-00-045	UC_2(g)	196	TRISO	88	1.15	35	1.93	1.17	29	3.22	40	1.81	3.8	1.13	192	578	2.33	17.8	-	2×10^{-7}	1×10^{-7}	-	X		
6151-02-025	UC_2(g)	204	TRISO	99	1.07	33	1.92	1.25	27	3.22	43	1.50	0.7	1.13	202	608	2.19	18.4	0.22	2×10^{-6}	1×10^{-6}	8×10^{-4}		X	C3T10,11,12
6151-03-015	UC_2(g)	199	TRISO	99	1.10	31	1.90	1.24	29	3.22	45	1.77	1.5	1.12	204	594	2.40	17.6	0.23	2×10^{-6}	2×10^{-6}	7×10^{-4}		X	C3T1,2,3
6151-08-015	UC_2(g)	202	TRISO	95	1.07	33	1.92	1.25	26	3.21	36	1.76	3.6	1.09	190	593	2.28	18.6	-	1×10^{-7}	9×10^{-7}	-	X	X	C3T7,8,9
6151-09-015	UC_2(g)	197	TRISO	105	1.15	31	1.94	1.16	29	3.22	39	1.94	3.6	1.06	204	587	2.30	17.8	-	9×10^{-8}	4×10^{-7}	-	X		
6155-01-020	$(Th,U)O_2$	502	TRISO	106	1.24	32	1.93	1.17	34	3.22	42	1.81	3.4	1.07	214	885	3.34	5.2	43.6	6×10^{-7}	6×10^{-7}	7×10^{-5}		X	C4T4,5,6
Fertile Particles																										
4252-02-010	ThO_2	488	BISO	83	1.08	-	-	-	-	-	73	1.83	4.0	1.16	156	805	3.51	-	58.8	-	-	2×10^{-5}		X	C4T2,3
4252-06-010	ThO_2	516	BISO	85	1.10	-	-	-	-	-	76	1.82	5.7	1.14	161	841	3.54	-	58.9	-	-	7×10^{-4}		X	C3T1,2
6252-00-025	ThO_2	512	TRISO	60	1.16	30	1.87	1.25	31	3.21	42	1.81	4.2	1.24	164	833	3.77	-	54.0	-	-	9×10^{-7}		X	C3T11,12
6542-01-010	ThO_2	500	BISO	79	1.08	-	-	-	-	-	85	1.80	10.0	1.06	164	828	3.59	-	56.5	-	-	6×10^{-6}	X		
6542-01-020	ThO_2	504	BISO	81	1.17	-	-	-	-	-	74	1.82	2.7	1.10	155	813	3.55	-	57.5	-	-	6×10^{-6}	X		
6542-02-020	ThO_2	481	BISO	87	1.08	-	-	-	-	-	72	1.91	8.5	1.06	159	796	3.59	-	56.2	-	-	2×10^{-5}	X		
6542-09-010	ThO_2	511	BISO	84	1.06	-	-	-	-	-	75	1.93	5.0	1.13	159	822	3.56	-	57.6	-	-	1×10^{-4}	X		
6542-12-025	ThO_2	505	BISO	84	1.10	-	-	-	-	-	70	1.79	6.7	1.22	154	816	3.58	-	58.0	-	-	5×10^{-7}		X	C4T11,12
6542-16-010	ThO_2	502	BISO	39	1.08	-	-	-	-	-	55	(h)	3.7	1.07	94	687	4.84	-	70.4	-	-	1×10^{-4}		X	C4T4,5,6
6542-17-010	ThO_2	502	BISO	44	0.95	-	-	-	-	-	122	1.86	2.8	1.27	166	829	3.55	-	54.5	-	-	6×10^{-7}		X	C4T1
6542-19-015	ThO_2	486	BISO	81	1.15	-	-	-	-	-	77	1.78	7.5	1.16	158	824	3.55	-	58.9	-	-	4×10^{-6}	X	X	C4T7
6542-19-016[i,j]	ThO_2	486	BISO	81	1.15	-	-	-	-	-	77	1.78	7.5	1.16	158	824	≈3.45[k]	-	58.9	-	-	4×10^{-6}		X	C4T8
6542-20-035	ThO_2	462	BISO	80	1.20	-	-	-	-	-	83	1.84	3.6	1.15	163	810	3.50	-	57.4	-	-	1×10^{-6}	X		
6542-21-015	ThO_2	492	BISO	79	1.13	-	-	-	-	-	82	1.73	7.8	1.10	161	833	3.46	-	57.4	-	-	4×10^{-6}		X	C4T10
6542-21-016[j,l]	ThO_2	492	BISO	79	1.13	-	-	-	-	-	82	1.73	7.8	1.10	161	833	≈3.40[k]	-	57.4	-	-	4×10^{-6}		X	C4T9
6542-22-015	ThO_2	503	BISO	85	1.12	-	-	-	-	-	81	1.80	4.0	1.07	166	831	3.50	-	58.0	-	-	1×10^{-6}		X	C3T3,4
6542-22-025	ThO_2	500	BISO	81	1.15	-	-	-	-	-	80	1.81	7.6	1.10	161	833	3.53	-	57.8	-	-	3×10^{-6}		X	C3T5,6
6542-23-025	ThO_2	486	BISO	82	1.19	-	-	-	-	-	73	1.89	5.7	1.09	155	800	3.58	-	57.5	-	-	4×10^{-6}		X	C3T7,8
6542-24-015	ThO_2	511	BISO	86	1.13	-	-	-	-	-	83	1.94	6.6	1.11	169	844	3.55	-	57.1	-	-	1×10^{-6}		X	C3T9,10
Inert Particles																										
6351-01-020	C	253	TRISO	-	-	29	1.76	1.09	29	3.22	36	1.75	-	1.12	-	573	1.83	-	-	-	-	-	X		

[a] TRISO denotes a coating design with a SiC layer and BISO denotes a particle with no SiC layer.

[b] Optical anisotropy factor, relative units.

[c] Release rate/birth rate for Kr-85m at 1100°C.

[d] Determined by leach test.

[e] Fissile kernels 93.15% enriched.

[f] C denotes cell; T denotes tray. Each tray holds approximately 225 fissile particles and 450 fertile particles.

[g] Kernels Th doped.

[h] Not determined.

[i] Density separated from parent batch 6542-19-016.

[j] Parameters listed are for parent batch, except particle density.

[k] Estimated, under going final QC analysis.

[l] Density separated from parent batch 6542-21-015.

TABLE 9-8

DESCRIPTION OF COATED PARTICLE SAMPLES BEING TESTED IN CAPSULE P13Q

Data Retrieval Number	Sample Number	Kernel[a] Type	Kernel[a] Density (g/cm^3)	Kernel[a] Mean Diameter (μm)	Coating[a] Buffer Type	Buffer Thick. (μm)	Buffer Density (g/cm^3)	Inner Isotropic PyC Thick. (μm)	Inner Isotropic PyC Density (g/cm^3)	Inner Isotropic PyC OPTAF	SiC Thick. (μm)	SiC Density (g/cm^3)	Outer Isotropic PyC Thick. (μm)	Outer Isotropic PyC Density (g/cm^3)	Outer Isotropic PyC OPTAF	Total Coating Thickness (μm)	Total Coated Particle[a] Mean Diameter (meas.) (μm)	Total Coated Particle[a] Density (g/cm^3)	Mutual Loadings U (%)	Mutual Loadings Th (%)	Fission Gas Release[b]	Thorium Contamination[c] (g Th/g Th)	Used in Fuel Rods	Used in Particle Tests
Fissile																								
4163-00-014[d]	TU01393BILS1-1-W	$(Th,U)O_2$[e,f]	(10.00)	250	TRISO	63	(1.17)	(32)	(1.78)	(1.14)	49	(3.20)	74	(1.77)	(1.09)	218	668	2.45	(9.13)	(9.18)	(3.23×10^{-9})	(2.3×10^{-4})		X
5466-37-1-3[d]	5466-37E	$(Th,U)O_2$[e,f]	(9.94)	248	TRISO	93	(1.12)	(29)	(1.87)	(1.07)	35	(3.18)	36	(1.79)	(1.10)	193	625	2.45	(12.65)	(12.65)	(1.08×10^{-6})	(6.10×10^{-5})		X
6151-00-010	5862-107E	UC_2[g,f]	10.99	199	TRISO	97	1.18	35	1.94	1.19	31	3.20	44	1.80	1.11	200	595	2.26	17.28	.43	3.987×10^{-7}	0	X	
6151-00-013[d]	5862-107E	UC_2[g,f]	(10.99)	194	TRISO	88	(1.18)	(35)	(1.94)	(1.19)	31	(3.20)	44	(1.80)	(1.11)	191	581	2.27	(17.28)	(.43)	(3.987×10^{-7})	(0)		X
Fertile																								
6542-01-010	5730-5-ABC	ThO_2	10.04	500	BISO	79	1.08	--	--	--	--	--	85	1.80	1.06	164	828	3.49	--	56.51	--	$< 1.6 \times 10^{-6}$	X	
6542-01-013[d]	5730-5-ABC	ThO_2	(10.04)	500	BISO	81	(1.08)	--	--	--	--	--	87	(1.80)	(1.06)	168	819	3.44	--	(56.51)	--	$(< 1.6 \times 10^{-6})$		X
6542-02-010	5741-141-ABC	ThO_2	9.88	504	BISO	77	1.09	--	--	--	--	--	91	1.88	1.06	168	833	3.39	--	54.99	--	1.6×10^{-6}	X	
6542-02-013[d]	5741-141-ABC	ThO_2	(9.88)	509	BISO	78	(1.09)	--	--	--	--	--	89	(1.88)	(1.06)	167	841	3.45	--	(54.99)	--	$(< 1.6 \times 10^{-6})$		X
4252-06-012-9[d]	TO1414BIL	ThO_2	(9.94)	508	BISO	79	(1.10)	--	--	--	--	--	73	(1.82)	(1.14)	152	820	3.63	--	(58.90)	--	(2.5×10^{-4})		X
Inert																								
6641-00-040	5862-125	Inert	1.28	∿500	BISO	∿80	(h)	--	--	--	--	--	62	1.88	1.13	∿142	791	1.48	--	--	--	--	X	
6641-00-043[d]	5862-125	Inert	(1.28)	(∿500)	BISO	(∿80)	(h)	--	--	--	--	--	63	(1.88)	(1.13)	∿143	729	1.50	--	--	--	--		X
4361-00-010	ORNL 1833	Inert	1.4[i]	534	TRISO	(h)	(h)	(h)	(h)	1.10	16	3.19	28	1.90	1.09	(i)	534	1.72	--	--	--	--	X	

[a] Numbers in parenthesis are values measured on particle parent batches.

[b] Release rate/birth rate for Kr-85m at 1100°C.

[c] Values given indicate amount of exposed Throium as determined by Th hydrolysis.

[d] Particle test samples were selected from parent batches by density separation.

[e] Th:U Ratio = 1.01/1.

[f] U is 93.15% enriched with U-235.

[g] Th:U ratio = 0.986/1.

[h] Not determined.

[i] Data obtained from ORNL.

TABLE 9-9
DESCRIPTION OF FUEL RODS BEING TESTED IN CAPSULE P13Q

Rod Number[a]	Position in Capsule	Coated Particles						Shim Material Type	Matrix			Particle Packing Fraction[c,d] (%)	Loading Uniformity[f,g]		Fission Gas Release[h,g]	Thorium Contamination[i,b] (g Th/g Th)	External Rod Condition (Visual)[j,g]
		Fissile		Fertile		Inert			Filler[b] (wt%)	Apparent Density[c,d] (g/cm^3)	Macro-porosity[e,b] (%)		Th	U			
		Type	Batch No.	Type	Batch No.	TRISO Batch No.	BISO Batch No.										
7161-002-19-3	3-1A	TRISO	6151-00-010	BISO	6542-01-010	4361-00-010	6641-00-040	1099	44.07	(k)	(k)	60	1.075	1.013	$<1 \times 10^{-7}$	7.3×10^{-5}	18.5
7161-002-20-3	3-2A	TRISO	6151-00-010	BISO	6542-01-010	4361-00-010	6641-00-040	1099	45.07	(k)	21.4	60	1.050	1.040	1.5×10^{-7}	$<6.0 \times 10^{-7}$	19
7161-002-21-3	3-3A	TRISO	6151-00-010	BISO	6542-02-010	4361-00-010	6641-00-040	1099	43.93	(k)	27.4	60	1.071	1.028	2.4×10^{-7}	$<6.0 \times 10^{-7}$	19
7261-002-10-3	3-1B	TRISO	6151-00-010	BISO	6542-01-010	4361-00-010	6641-00-040	1099	44.32	0.843	22.8	56	1.128	1.125	1.3×10^{-6}	1.6×10^{-6}	17
7261-002-11-8	3-2B	TRISO	6151-00-010	BISO	6542-01-010	4361-00-010	6641-00-040	1099	44.48	0.840	25.6	56	1.151	1.117	$<1 \times 10^{-7}$	6.6×10^{-5}	19
7261-002-12-8	3-3B	TRISO	6151-00-010	BISO	6542-02-010	4361-00-010	6641-00-040	1099	44.65	0.851	21.2	56	1.194	1.110	5.1×10^{-7}	$<9.0 \times 10^{-7}$	18
7261-002-13-3	2-1A	TRISO	6151-00-010	BISO	6542-01-010	4361-00-010	6641-00-040	1099	42.74	0.844	22.9	56	1.114	1.033	1.8×10^{-6}	5.5×10^{-6}	19
7261-002-14-3	2-2A	TRISO	6151-00-010	BISO	6542-01-010	4361-00-010	6641-00-040	1099	40.92	0.913	21.0	56	1.161	1.039	1.8×10^{-6}	$<1.3 \times 10^{-6}$	19.5
7261-002-15-3	2-3A	TRISO	6151-00-010	BISO	6542-01-010	4361-00-010	6641-00-040	1099	32.48	0.744	31.2	56	1.211	1.059	5.6×10^{-6}	5.3×10^{-5}	19.5
7161-002-13-3	2-1B	TRISO	6151-00-010	BISO	6542-01-010	4361-00-010	6641-00-040	1099	45.06	0.871	18.8	60	1.009	1.001	4.2×10^{-7}	$<1.8 \times 10^{-6}$	18
7161-002-14-3	2-2B	TRISO	6151-00-010	BISO	6542-01-010	4361-00-010	6641-00-040	1099	44.62	0.912	24.2	60	1.137	1.003	4.6×10^{-6}	1.5×10^{-5}	19.5
7161-002-15-8	2-3B	TRISO	6151-00-010	BISO	6542-01-010	4361-00-010	6641-00-040	1099	35.54	0.743	34.8	60	1.154	1.042	3.4×10^{-7}	4.7×10^{-4}	19
7261-002-16-8	1-1A	TRISO	6151-00-010	BISO	6542-01-010	4361-00-010	6641-00-040	1099	41.80	0.822	26.2	56	1.135	1.014	1.1×10^{-6}	$<2.0 \times 10^{-6}$	18
7261-002-17-3	1-2A	TRISO	6151-00-010	BISO	6542-01-010	4361-00-010	6641-00-040	1099	45.46	0.789	24.0	56	1.189	1.005	7.9×10^{-6}	$<2.0 \times 10^{-6}$	20
7261-002-18-5	1-3A	TRISO	6151-00-010	BISO	6542-02-010	4361-00-010	6641-00-040	1099	39.94	0.847	25.9	56	1.187	1.021	3×10^{-5}	$<4.1 \times 10^{-6}$	17
7161-002-16-8	1-1B	TRISO	6151-00-010	BISO	6542-01-010	4361-00-010	6641-00-040	1099	44.12	0.855	20.1	60	1.108	1.007	1.6×10^{-6}	4.1×10^{-5}	18.5
7161-002-17-3	1-2B	TRISO	6151-00-010	BISO	6542-01-010	4361-00-010	6641-00-040	1099	43.62	0.794	22.6	60	1.078	1.008	9.8×10^{-6}	$<2.2 \times 10^{-6}$	20
7161-002-18-8	1-3B	TRISO	6151-00-010	BISO	6542-02-010	4361-00-010	6641-00-040	1099	45.84	0.875	20.4	60	1.145	1.033	$<1 \times 10^{-7}$	9.1×10^{-6}	19

[a] All fuel rods are 0.61 in. in diameter by 2.1 in. long.
[b] Data obtained on companion fuel rod from same batch.
[c] Calculated from green/fired fuel rod dimensions and nominal particle parameters.
[d] Data obtained by using batch average values.
[e] Determined by taking average value from two metallographic cross-section composite photographs of a rod from each batch.
[f] Ratio of peak-to-average metal content determined from γ scan of both ends of each rod.
[g] Data obtained on fuel rod actually used in capsule.
[h] Release rate/birth rate for Kr-85m at 1100°C.
[i] Determined by thorium hydrolysis test. Value indicates amount of exposed thorium.
[j] Examination based on a 1 to 20 scale score.
[k] Not determined.

1972. Both capsules were designed to operate isothermally with a 1250°C axial (centerline) temperature and were monitored for in-pile fission gas release during irradiation. Capsule HRB-5 was discharged from the HFIR in February 1973, after completing its scheduled irradiation (5 cycles) to a peak fast neutron fluence of 4.7×10^{21} n/cm^2 (E > 0.18 MeV). Capsule HRB-4 was discharged from the HFIR in July 1973, after completing its scheduled irradiation (11 cycles) to a peak fast neutron fluence of $\sim 10.5 \times 10^{21}$ n/cm^2.

The GGA samples in each capsule consisted of six fuel rods (two each of three different types) having nominal dimensions of 0.05 x 1.00 in. These samples included rods fabricated with three different graphite fillers, one binder, and two types of graphite shim material. All rods were fabricated by the admix compaction process and were carbonized and high-fired in H-327 graphite tubes to simulate in-block curing. A description of the fuel rods tested in capsules HRB-4 and HRB-5 was given in an earlier Quarterly Progress Report (Gulf-GA-A12422).

Results of the visual examination, dimensional change measurements, and postirradiation fission gas release measurements on the six GGA fuel rods irradiated in HRB-5 were reported in an earlier Quarterly Progress Report (Gulf-GA-A12599). The six GGA fuel rods irradiated in capsule HRB-4 are currently undergoing postirradiation examination in the GAA Hot Cell.

HRB-6

Capsule HRB-6 represents a cooperative GGA-ORNL irradiation effort designed to evaluate the irradiation performance of fuel rods fabricated using candiate processes and materials for large HTGR startup and recycle fuel systems. The six GGA fuel rods tested in this experiment contained a blend of (Th,U)C_2 TRISO/ThO_2 BISO/inert carbon BISO particles. These rods were fabricated using the hot injection process and were cured in-place in H-451 graphite. A more complete description of the fuel rods

tested in capsule HRB-6 was given in an earlier Quarterly Progress Report (Gulf-GA-A12515).

The capsule was designed to operate isothermally with a 1250°C axial (centerline) temperature and was designed to be swept with helium to monitor for in-pile fission gas release during irradiation. Capsule HRB-6 was discharged from the HFIR in September 1973 after completing eight irradiation cycles to a peak fast neutron fluence of $\sim 8 \times 10^{21}$ n/cm^2 (E > 0.18 MeV).

Disassembly and preliminary examination of capsule HRB-6 was conducted at ORNL. The six GGA fuel rods were judged to be in good condition. The fuel rods were intact and very little matrix cracking occurred except for circumferential cracking around the matrix end caps. Some matrix and particle debonding occurred on the sides of the rods as a result of mechanical interaction with the graphite sleeve as the rods were being pushed out. The fuel rods are being shipped to GGA for further Hot Cell examinations.

Capsules HT-12, HT-13, HT-14, and HT-15

HT-12 through HT-15 is a series of four irradiation experiments designed to test the irradiation behavior of unbonded, BISO coated, ThO_2 fertile fuel particles. All capsules have completed irradiation and have been transferred to the GGA Hot Cell facility where examination of the fuel samples is currently in progress. Visual examination, radiography, metallography, and density gradient column separations are being used to evaluate the particle samples.

TASK XI
GRAPHITE RESEARCH

INTRODUCTION

Work during the current quarter was divided among five major tasks: (1) irradiation of production-grade near-isotropic and needle-coke graphites in graphite irradiation capsule OG-1, (2) design and initial fabrication of graphite irradiation capsule OG-2, (3) initial planning and scheduling of near-isotropic graphite screening tests in irradiation capsules HT-20 through -23, (4) improvement of graphite tensile testing procedures, and (5) development of a project plan report covering the A budget graphite irradiation task.

CAPSULE IRRADIATIONS

Capsule OG-1

Graphite irradiation capsule OG-1 has been under irradiation in the ORR since June 23, 1973. This capsule, described in an earlier Quarterly Progress Report (Gulf-GA-A12422), will provide irradiation data primarily on advanced fuel block graphites with some data on pyrolytic carbons, silicon carbide, boronated control graphites, and fuel rod matrix materials. The capsule is operating at 600°C to 1400°C and will reach fluences of 0.5 to 4.4 x 10^{21} n/cm^2 ($E > 0.18$ MeV). It will be discharged December 2, 1973 at the conclusion of cycle 115.

Plans have been made and procedures established to unload the capsule crucibles at ORNL. The crucibles will be transported to GGA for specimen unloading and postirradiation analysis.

Capsule OG-2

OG-2 is the second in the OG-series of capsule irradiations designed to gather irradiation data on advanced fuel block graphites. Capsule OG-2 has been designed to operate at the same temperatures as those of OG-1, thus allowing for reirradiation of OG-1 samples to higher fluences.

During the current quarter a tentative schedule for fabricating OG-2 by April 19, 1974 and insertion by May 19, 1974 has been established. Samples cut from production-size near-isotropic graphites are being assembled and measured for inclusion in OG-2.

HT-20 Through -23 (ORNL Capsules)

Tentative plans have been made with personnel at ORNL to screen near-isotropic advanced graphites by utilizing the end positions of four ORNL HT-type capsules. The capsules will be designed to operate between 910° and 960°C to fluences of $\sim$1.5, 3, 5, and 8 x 10^{21} n/cm^2 (E > 0.050 MeV). Three or four different graphite grades will be included.

GRAPHITE PROPERTIES AND IRRADIATION

A systematic sampling plan for machining experimental specimens from production-size graphite logs has been prepared. Templates for laying out the location of a set of specimens for each log have been fabricated. The sampling plan has been used in the preparation of specimens of production-size near-isotropic graphites for capsule OG-2.

Work continues on improvement of stress-strain and tensile testing procedures. Tests with spherical bearings, roller bearings, roller chains, and knive-edge type grip ends are being conducted using strain gage implemented specimens. The aim of these tests is to devise a system of grip ends which will greatly reduce or eliminate bending moments during testing.

Specimens have been prepared and plans are being made to measure the Poisson's ratio of H-451 graphite as a function of orientation and position in a production-type log. These tests will proceed when the proper end grips have been selected.

PROJECT PLAN

The project plan report is in preparation. This plan involves the testing and qualification of near-isotropic graphites for use in fuel and reflector blocks for early large HTGRs. The issuance of the project plan is scheduled for the first of February, with a working draft available in early January.